An efficient methodology based on two-and-a-half-dimensional finite element and boundary element methods for ground-borne vibration radiated by underground railway tunnels and the re-radiated noise emitted inside them

by
Dhananjay Ghangale

An efficient methodology based on two-and-a-half-dimensional finite element and boundary element methods for ground-borne vibration radiated by underground railway tunnels and the re-radiated noise emitted inside them

A dissertation submitted by

by

Dhananjay Ghangale

advisor/s

Robert Arcos Villamarín

Jordi Romeu Garbí

in partial fulfilment of the requirements of the

Doctoral degree

in

Escola Superior d'Enginyeries Industrial, Aeroespacial i Audiovisual de Terrassa

Department of Mechanical Engineering

Universitat Politècnica de Catalunya

June 2019

If we have chosen the position in life in which we can most of all work for mankind, no burdens can bow us down, because they are sacrifices for the benefit of all; then we shall experience no petty, limited, selfish joy, but our happiness will belong to millions, our deeds will live on quietly but perpetually at work, and over our ashes will be shed the hot tears of noble people.

Karl Marx

Abstract

Escola Superior d'Enginyeries Industrial, Aeroespacial i Audiovisual de Terrassa

Department of Mechanical Engineering

by Dhananjay Ghangale

This thesis presents a methodology for assessing induced ground-borne vibration due to underground railway infrastructures in the context of an urban environment. The methodology is based on a comprehensive numerical approach for modelling track/tunnel/soil systems considering a full-space model of the ground. This approach is formulated in the wavenumber-frequency domain and it is based on coupled finite element-boundary element method. An axisymmetric formulation to deal with circular underground railway tunnels is included in the approach in order to improve the computational speed of the methodology. This formulation can also be used for other types of railway tunnels if a circular boundary of the boundary element mesh is considered. The developed approach also includes asymptotic solutions of the Green's functions for large wavenumbers which results in an improvement of the accuracy of the overall methodology. A hybrid methodology which uses semi-analytical solutions of a cavity in a full-space in conjunction with the previously described approach has been developed with the aim of computing the energy flow radiated upwards by underground railway tunnels. Since this methodology uses finite elements to model the tunnel structure, its modelling detail is higher than the previously developed methodologies based on semi-analytical modelling of the tunnel structure. This hybrid methodology has been specifically designed for the study the vibration radiation of railway tunnels, the comparison between them and for the study of the insertion loss of mitigation measures at the sources, as soft rail-pads, under-ballast or under-slab mats, dynamics vibration absorbers, etc. In this thesis, this hybrid methodology is used to perform a comparison of the energy flow radiated upwards by various types of underground railway tunnels. Finally, a modelling approach for the re-radiated noise induced by a train passage inside railway tunnels is presented. This approach is based on the weak coupling between the comprehensive numerical approach for modelling track/tunnel/soil previously described and a two-and-a-half-dimensional boundary element method model for interior acoustics. Using this modelling approach, the influence of the fastener stiffness on the noise and vibration levels inside a simple tunnel as well as the relation between the noise emitted by the rails or the tunnel structure is investigated and discussed.

Acknowledgements

Firstly, I would like to express my sincere gratitude to Prof. Jordi Romeu, one of my thesis advisors, for giving me the opportunity to pursue my Doctoral dissertation under his supervision. His positive attitude immensely benefited my research and his immense support for technical and personal matters made the four years worthwhile.

I would also like to express my sincere gratitude to my advisor Dr. Robert Arcos for the continuous support of my doctoral study and related research, for his patience, motivation, and immense knowledge. His guidance helped me in all the time of research and writing of this thesis. I could not have imagined having a better advisor and mentor for my doctoral study.

My sincere gratitude also goes to Dr. Pedro Alves Costa, who provided me with the opportunity to join his team as an intern, and who provided me with new insights in my research and helped me broaden my research horizons. I would also like to express my gratitude to his research group members for making me feel at home in Porto. Without their precious support and feedback, it would not have been possible to conduct a major part of my thesis.

I would also like to thank my colleagues Dr. Arnau Clot and Behshad Noori and the lab members for making the time I spent in Terrassa fun both inside and outside the workplace and for patiently braving my infinite queries related to my research. I would also like to express my sincere gratitude to Julen and Marta for their kind friendship and hospitality.

I would like to thank my friends from Porto and Terrassa, my Sensei Vasco and the members of Senshin Ryu Jujutsu who are like my surrogate family since my time in Porto, for helping me familiarise with the new culture and help me overcome the challenges encountered while living abroad. I would also like to mention my two good friends Cristina and Hélène for the constant support and encouragement they provided.

I would also like to express my sincere gratitude to the community at free and open source software Linus Torvalds for the Linux kernel and the developers of Matlab without which the simulations in this thesis would not have been possible.

Last but not least, I would like to thank my family: my parents and to my brother for supporting me spiritually throughout writing this thesis and my life in general.

Declaration

I hereby declare that the thesis I am submitting is entirely my own original work except where otherwise indicated. I am aware of the University's regulations concerning plagiarism, including those regulations concerning disciplinary actions that may result from plagiarism. Any use of the works of any other author, in any form, is properly acknowledged at their point of use.

Dhananjay Ghangale

Contents

List of Figures

List of Tables

To my Mother and my Father

Chapter 1

Introduction

This chapter begins with a brief introduction to railway-induced ground-borne vibration and noise problems and justifies the main reasons that led to the development of the present work. The chapter concludes with a brief outline of the contents of each of the chapters in the thesis.

1.1 Justification of the work

Noise and vibration pollution in urban areas is a major issue of concern for governments and administrations due to the increasing preoccupation by the general population about the effects on their comfort and quality of life. One of the most important sources that cause this contamination is railway traffic. In the past, when infrastructures were constructed in urban areas, the concern was focused on the airborne noise emitted by at-grade railway infrastructures, mainly due to the rolling noise: noise radiated by the rail and wheel due to their vibrations induced by the wheel/rail contact excitation mechanism. Nowadays, in contrast, as most of the urban railway lines are underground, the focus is placed on the ground-borne railway-induced vibration and noise in buildings. Ground-borne vibration is perceived as mechanical vibration of the human body in a relevant frequency range from 1 Hz to 80 Hz and ground-borne noise (also known as re-radiated noise) is perceived as a sound emitted by the building structure in a relevant frequency range from 16 Hz to 250 Hz [1].

Since almost all developed regions of the world have laws to regulate the maximum levels of noise and vibration to which the population is exposed, predictions of these levels must be carried out in designing new railway infrastructures or when new buildings are planned to be located near existing ones. The operation of underground railway infrastructures could affect the quality of life of the inhabitants in the buildings and could also affect the structural health of nearby buildings (mostly old and historical), facilities or other infrastructures. Also, the noise generated from these underground railway infrastructures affects the comfort of the passengers inside the vehicle as well as the commuters on the train station [2, 3, 4].

In the literature, three models dedicated to studying the ground-borne vibration induced by railway infrastructures are encountered: empirical models, semi-analytical models and numerical models. Empirical models are based only on statistically treated experimental measurements data and cannot accurately represent particular cases. Semi-analytical models describe the dynamic behaviour of the system using in the basis of the combination of simple systems, like beams, plates, shells and half-spaces. They allow to deeply understand the mechanics of the considered problems. These models are much

more adaptive to particular cases than empirical models and computationally less taxing as compared to the numerical model. These analytical models are good models in the initial design stages of a new railway line project or to cover a large number of different situations in an efficient way. However, one of the disadvantages of these models is that they can only model the system in terms of geometrically simple systems, which means that they can not be used for detailed studies. Thus, when the detailed prediction of a particular system is required, numerical models are the most suitable solution, since they ensure higher accuracy.

Most of the numerical methods are based on some kind of discretisation of either the domain or the boundary of the domain. Specifically speaking about two of the most used methods in the field, the finite element method (FEM) is based on the discretization of the domain or boundary element method (BEM) is based on the discretization of only the boundary. However, these numerical methods are slow. Meshless methods, like the method of the fundamental solutions (MFS) are also being used to improve the computational speed by numerical modelling. However, these meshless methods are not quite as robust as mesh-based ones. As the railway infrastructures are mostly assumed to be invariant in one direction, a two-and-a-half dimensional approach (2.5D) can be used. In the present work, the numerical methodology presented is based on a 2.5D FEM and 2.5D BEM approaches.

In order to increase the efficiency on the prediction of railway-induced ground-borne or structural-borne vibration and noise, fast methods based on coupled finite element-boundary element method in two and a half-domain (2.5D FEM-BEM) to study the railway-induced ground-borne vibration are developed in this thesis. Moreover, this thesis presents a methodology to assess the efficiency of a vibration mitigation countermeasures used in underground infrastructures by computing the vibration energy radiated upwards that has been developed and applied for realistic study cases. In order to perform analysis of noise radiation due to train pass in closed domains, a 2.5D acoustic BEM is also developed. The main highlights of this thesis are summarised as follows:

1. A numerical methodology based on a 2.5D FEM-BEM approach and on the semi-analytical solutions of a cavity in a full-space for the computation of the vibration energy flow in the soil radiated by underground railway infrastructures is established.

2. A decoupled methodology based on a coupled 2.5D FEM-BEM approach and a 2.5D acoustic BEM for the computation of re-radiated noise in underground railway infrastructures is presented.

3. A 2.5D acoustic BEM with regularised integral for computation of sound radiations has been developed in the context of this thesis.

4. An efficient wavenumber-frequency sampling strategy for obtaining an accurate response of the system due to a train pass-by excitation is presented.

5. Fast methods for obtaining the 2.5D BEM matrices required in the overall methodology have been derived and implemented in the context of this thesis.

6. Application examples of realistic study cases of the methodologies developed in this thesis are presented. Specifically, a study of the validity of the assessment of vibration reducing countermeasures by one accelerometer on the tunnel wall.

1.2 Thesis outline

The thesis is organised in six chapters. In this chapter, the justification and organisation of the thesis are presented. Chapter 2 focuses on the review of the literature relevant to the thesis topic. Chapter 3 presents the theoretical framework concerning the 2.5D FEM-BEM. It also presents the new developments that have been incorporated in the 2.5D FEM-BEM that results in improving the computational cost of the 2.5D FEM-BEM. Chapter 4 focuses on the development of a computation scheme for energy flow radiated by underground railway tunnels on account of train passage. Chapter 5 is an extension of Chapter 4 and focuses on the study of the validity of the assessment of vibration reducing countermeasures by one accelerometer on the tunnel wall. Chapter 6 focuses on developing a decoupled computation scheme for the re-radiated noise generated inside an underground railway tunnel by train passage. In this chapter, a 2.5D BEM approach for acoustic problems is presented together with a study on the influence of the stiffness of the fasteners as vibration reducing countermeasures on the noise and vibration response of existing underground infrastructure. Finally, the conclusions of this thesis are presented in chapter 7, where some recommendations and considerations for future research in this area are presented.

Chapter 2

State of the art

In this chapter, the literature review of the publications relevant to the thesis is presented. The chapter presents a summary of the semi-analytical and numerical models encountered in the literature that are used in the analysis of problems in elastodynamic and acoustic. As the thesis presents a methodology that has been specifically designed to be used in general assessment studies about ground-borne underground railway-induced vibrations where decisions on the type of track and/or the application of mitigation measures at the sources, as soft rail-pads, under-ballast or under-slab mats have to be made, an overview of isolation countermeasures used for mitigating of vibration radiated by railway infrastructures is also presented.

2.1 Introduction

Several approaches have been developed in the past two decades to achieve railway-induced ground-borne noise and vibration predictions. Fundamentally, these prediction approaches are of three kinds: empirical, analytical and numerical [5]. Empirical models are based on measurements performed on specific sites and, thus, in the majority of cases, are not usually suitable for predictions of new infrastructures. A detailed review of railway-induced ground-borne vibration can be found in [6, 7, 8]. In general, analytical and numerical approaches are the most commonly used methodologies nowadays. They are all based on at least one of the main excitation mechanisms [9]:

- The quasi-static excitation, which is induced by the the static component of the train axle loads moving along the track. In general, it has a low-frequency content (<20 Hz), which shifts to lower frequencies with increasing distance from the track and to higher frequencies with increasing train speed [10]. This excitation dominates the ground-borne vibration in the case of high-speed trains with running speeds close to the Rayleigh phase velocity of the ground (trans-Rayleigh trains). In contrast, for typical urban train speeds (sub-Rayleigh trains), this excitation only dominates the track response [11].

- The dynamic excitation, which is induced by the dynamic component of the wheel-rail contact forces generated, basically, by the spatial variation of the support stiffness and track roughness. It has a high-frequency content in general: between 20 Hz and 250 Hz. In the case of sub-Rayleigh trains, this excitation mainly dominates the ground-borne vibration.

2.2 Semi-analytical models

Hunt et al. [12, 13] presented an analytical-stochastic methodology to calculate ground-borne vibration in buildings due to underground railway traffic from a three-dimensional (3D) point of view. In this model, the building is assumed to be an infinitely long structure composed of beams, columns and a piled foundation, in which a homogeneous half-space model for the ground is assumed. Also assumed in that work was a weak coupling between the incident wave field due to the railway traffic and the building structure, which means that the free field displacements of the ground are assumed to be the excitation of the ground/building structure model uncoupled with the railway infrastructure. This incident wave field was calculated using a stochastic modelling of the vibration generation and propagation mechanisms [14].

Recently a theoretical model was formulated in a moving coordinate system to evaluate the propagation constants and the localisation factors of a periodic jointed tunnel by [15]. The periodic tunnel was approximated as a pipe-beam model with periodic joints on elastic foundations. Timoshenko beam theory was utilised for the tunnel segment, while the segment joints were simplified as linearly elastic springs. A three-dimensional analytical model for the prediction of ground vibrations from two parallel tunnels embedded in a full-space was presented by [16]. The two tunnels were modelled as cylindrical shells of infinite length, and the surrounding soil was modelled as a full-space with two cylindrical cavities. Closed-form semi-analytical solution for the vibrations due to a moving point load in a tunnel embedded in a half-space by [17]. An analytical method to calculate ground vibrations from a tunnel in a multi-layered half-space was presented in [18].

The most recognised semi-analytical model for underground ground-borne vibrations is probably the Pipe-in-Pipe (PiP) model, developed by Forrest and Hunt [19, 20]. The initial formulation has been later improved and used for obtaining a wide variety of results. Hussein and Hunt [21] coupled the tunnel-soil model to a floating-slab track model. Moreover, Gupta et al. [22] compared the PiP model results to those obtained using a coupled FEM-BEM periodic model of the superstructure/tunnel/soil system, and they highlighted the advantages and limitations of both models as well. Hussein et al. [23] extended the initial full-space formulation to a half-space one using the full and half-space 2.5D elastodynamic Green's functions obtained by Tadeu and Kausel [24, 25]. The extension to a layered half-space using a fictitious force method has been recently presented by Hussein et al. [26]. On the other hand, it should be mentioned that the PiP model is unable to deal with alternative construction geometries such as the mentioned double-deck tunnel.

2.3   Numerical models

Regarding the modelling, the complete system related to underground railway-induced vibration problems, a model that accounts for the vehicle, the track, the tunnel, the ground and the building has to be constructed. The first predictive methodology that works with the complete system, which consists of the vehicle, the superstructure, the tunnel, the ground and the building, was developed by [27]. This methodology uses a two-dimensional (2D) finite element (FE) model to compare the train-induced vibration in a building for two superstructure systems: direct fixation fasteners (DFF) and floating slab track (FST). Both FE models for DFF and FST superstructures are excited by a pair of unit harmonic loads applied on the rail-heads, in order to determine the steady-state responses. Later, [28] extended the previous model to take into account quasi-static and dynamic excitation by making an equivalency for the case of non-moving wheel/rail contact forces. In another paper, Balendra et al. [29] developed a 2D analytical model of the same complete system by using a sub-structuring technique. However, 2D models do not take into account the wave propagation in the direction of the track and, even more important, they cannot account for the train motion along the track [30].

Stamos and Beskos [31] have used the three dimensional (3D) boundary element method (BEM) in determining the response of underground elastic structures. 3D BEM has also been used in the analysis of noise radiation, for example for the study of acoustic scattering [32] and in the analysis of acoustic barriers [33]. A disadvantage of the BEM is its instability on modelling thin geometries, as pointed out by Tadeu et al. [34].

Coupled formulations usually based on the finite element method (FEM) and BEM are proposed to address the disadvantage of using only BEM or FEM. These formulations have been proposed to study soil-structure interaction problems using a sub-domain decomposition where, in most of the cases, the structure is modelled with a domain discretisation method, like FEM, and the soil is modelled with a boundary discretisation method, like BEM. Bordon et al [35] have used a combined FEM-BEM approach to study the fluid-structure interaction of thin elastic bodies in his model the fluid is modelled using BEM while FEM is used to model the elastic body. Appropriate boundary and compatibility condition are utilised to couple the FEM and BEM equations. 3D BEM-FEM coupled models have also been used by Padron [36] in the analysis of piles and pile group embedded in the elastic medium.

In the context of railway-induced noise and vibration problems, Anderson and Jones [37] presented a comparison of 3D and two dimensional (2D) FEM-BEM methods for the analysis of vibration from railway tunnels. In these comparisons, it was found that a fully

3D model should be used in order to obtain correct predictions of the wave propagation, at least in the near field. However, the computational cost of 3D methodologies is always higher than the 2D ones. Coupled 3D FEM-BEM was used by Everstine et al. [38] to study fluid-structure interaction. In this method, FEM was used to model structure and the surrounding fluid was model with BEM. An edge-based smooth FEM (ES-FEM) was proposed in [39, 40] to solve 3D acoustic problems in mid-frequency, as ES-FEM reduces the numerical dispersion error in low to mid-frequency range. The proposed method showed better accuracy than FEM-BEM based on quadrilateral boundary elements.

Fiala et al.[41] developed a 3D methodology to calculate the ground-borne vibration and re-radiated noise on buildings for the case of at-grade infrastructures, based on an FE model of the building structure coupled with a boundary element (BE) model of the layered ground [42]. To compute the incident wave field induced by the train excitation, a weak coupling between this incident wave field and the building structure is also assumed. A longitudinally invariant track is assumed to calculate the free field ground surface displacements of the vehicle/superstructure/ground system, where the ground is modelled in the wavenumber-frequency domain by means of a BE methodology using the Green's functions of a layered half-space.

In order to reduce the required computational time for 3D models, two important methodologies appear: the 3D periodic approach [43, 22, 44] and the 2.5D approach [30, 45, 46] Fiala et al. [47] have used a methodology for analysis of vibrations of underground trains where, in order to take into account, the track longitudinal variability, they have used the well-established 3D periodic FEM-BEM model, previously developed by [43], for the computation of the free field ground surface displacements of the vehicle/superstructure/tunnel/ground system. This 3D periodic FEM-BEM approach has been extensively validated with analytical models, such as the "Pipe-in-Pipe"(PiP) model [22], and with experimental measurements [44].

Another relevant approach that is able to calculate the incident wave field due to railway traffic in a 3D is the 2.5D approach [42, 48, 49, 50, 9]. The methodology is applied to 3D cases, where the geometry is invariant (or assumed to be) in one direction. It involves taking Fourier transform of the coordinate of invariant direction and solving a set of 2D problems which are then Fourier anti-transformed to obtain the 3D solution. The advantage of this methodology is the reduction of the mesh dimensions by one. This methodology is being widely used nowadays, giving good results in the prediction of ground-borne vibration [30, 9, 51].

2.5D FEM was used for the simulation of wave propagation in the ground by high-speed train passage by Bian et al. [52]. Wave dissipation in the far field was taken into account

with absorbing boundaries constructed with frequency dependent dash-pots. However, the disadvantage of the using FEM combined with absorbing boundaries is the low computational speed and accuracy associated with the methodology.

Coupled formulation based on FEM and BEM in 2.5D was proposed by Sheng et al. [53, 30]. In this method the soil was modelled with BEM, the tunnel structure with FEM and the rails are assumed to be Euler beams. The BEM in that formulation used full-space Green's functions and, as a result, mesh truncation and meshing of layer interfaces is required in order to model layered half-spaces. Moreover, the singular terms appearing in BEM are explicitly computed in that methodology. Jin et al [54] validated the 2.5D FEM-BEM with experimental measurements. The method is based on [30] in this method the tunnel structure and the track are modelled using solid and beam finite elements while the ground is modelled using boundary elements. Recent investigations [50, 55] propose significant improvements of this methodology by using a regularised boundary integral as an alternative to the evaluation of the singular integrals which appear in the 2.5D BE formulation. Moreover, the direct stiffness matrix method for layered half-spaces [24] is used instead of the 2.5D fundamental solution of a homogeneous full-space, achieving very significant simplifications of the meshing problem. [56] has proposed a more efficient method to compute these Green's functions.

Lopes et al. [57] proposed a methodology for simulating the vibrations induced by traffic from the tunnel to the building in which the solution for the tunnel ground system is developed using a 2.5D technique based on the finite element method, and adopting perfectly matched layers (PML's) to model the waves in the soil. An alternative methodology was proposed by [58] which uses a mesh-less method of fundamental solution (MFS) instead of PML to model soil-structure interactions. MFS is preferred over PML for its computational efficiency of modelling large domains. In another approach. However, despite the computational advantages of MFS, significant errors can be introduced as the correctness of the MFS results is dependent on the number of virtual sources and on the distance between virtual sources and collocation points [59]. Tadeu et al. [60] found that the accuracy of MFS along with the domain strongly depends on the accuracy of the pre-calculated boundary conditions.

A hybrid model that used BEM to model the propagation of waves in the soil and cavity solution to model the tunnel was used to study the dynamic interaction between the Central line tunnels and those of Crossrail by Brooks et al. [61]. Germonpre et al. [62] proposed a model based on the wave analysis technique and PML to model a track that varies in the longitudinal direction and can be used to model parametric excitation due to any type of track stiffness variation. [45] proposed a method based on finite element

coupled with scaled boundary finite-element (SBFM), to study the ground vibration of underground railways. In this method, the unbounded domain is simulated by SBFEM.

In the context of modelling noise radiated by a structure in railway-induced ground-borne noise and vibration problems, Romero et al. Romero et al. [63] proposed a methodology based on coupled FEM-BEM where BEM was used to model unbounded solid domains and solid and/or fluid bounded domains were modelled with FEM. In this paper, a 2.5D FEM was developed to model interior acoustics assuming a strong coupling with the structural system. Subsequent improvements were made to this method by incorporating in BEM approach the Green's functions of a fluid-solid medium to represent a solid half-space flattened by a fluid medium [64]. This allows for modelling exterior acoustics in soil-structure interaction problems.

A 3D FEM-BEM methodology has also been used by Fiala et al. [41, 47] to model the re-radiated noise in buildings arising from ground-borne vibrations induced by underground railway traffic. In this model, the track/tunnel/soil system is modelled using the method presented in [9], which is based in a 2.5D FEM-BEM approach, and the structural building/soil system is modelled by means a 3D FEM-BEM, assuming a weak coupling between this two systems. The building interior acoustics is computed by means of a spectral FEM, also considering a weak coupling between the acoustic field and the structural vibration. Colaço et al. [65] also proposed a decoupled approach for the computation of the re-radiated noise in buildings generated by railway-induced ground-borne vibration that, in this case, uses MFS to study the interior acoustics problem. Sheng et al. [66] have used a decoupled BEM approach in the analysis of noise radiated in at-grade railway tracks.

2.4   Isolation countermeasures

The analysis of the vibration from the source to the receiver allows designing better vibration reducing countermeasures. A comprehensive overview of the state of the art on railway-induced ground vibration concerning governing physical mechanisms, prediction methods, and mitigation measures has been presented by [67]. A continuous row of heavy masses forming a wall next to the track was studied as a mitigation measure for railway induced ground-borne vibration by [68]. The effectiveness of this countermeasure was determined by means of a 2.5D FEM-BEM method. It was found that the masses were effective at a site which has soft soil and the performance of the masses was dependent on the height and width of the wall of the masses. Another countermeasure similar to the one just described is the use of sheet pile [69].

Vibration isolation at the source is the most common practice in control of railway-induced vibrations. It is achieved by changing the dynamic behaviour of the track through the insertion of resilient elements or additional masses to the track structure. The former includes using resilient elements beneath the rails or the sleepers, such as rail pads or under sleeper pads and the latter achieved by the use of floating slab and ballast mats in the slab and ballasted tracks, respectively [70]. Sub-grade stiffening is also used as vibration reducing countermeasure [71].

Rail pads are elastic polyurethane mats which are installed directly under the foot of the rail. The effectiveness of railpads stiffness is evaluated in the work of [72] which shows by decreasing the railpads stiffness, the power radiation at high frequencies (above 70Hz) will be decreased by an average of 14 dB. Under sleeper-pads are special pads which are placed between the sleepers and the ballast. By using under sleeper pads not only the force of the train is expected to be distributed to more sleepers but also it is expected that vibrations in the ballast and in the ground are reduced.

Ballast mats were also used as vibration reducing countermeasure by Costa et al. [70]. It was found that the ballast mat has a dual effect, focusing on the train–track dynamic behaviour and on the reduction of high-frequency vibrations that are transmitted to the ground. Furthermore, it was found that global efficiency can be reached by placing the mat beneath the sub-ballast instead of below the ballast layer. A set of inclusions buried in the soil has been investigated as a possible countermeasure by [73].

A floating-slab track is widely known as an effective measure for railway-induced ground-borne vibration from underground tunnels. Rubber bearings or steel springs are mounted between the tunnel bed and the slab, which can be continuous or discontinuous. In particular, vibration isolation efficiency of continuous and discontinuous floating slab tracks are analysed and compared in the work of [10]. They concluded that both continuous and discontinuous floating slab tracks have a similar efficiency in the frequency range well above the isolation frequency of the slabs while because of the importance of the parametric excitation in discontinuous case, it has poorer efficiency at low frequencies. In the middle frequency range, ballast mats are an efficient way to reduce vibrations.

Chapter 3

Fast coupled 2.5D FEM-BEM for homogeneous full-space and half-space problems

The chapter presents the elastodynamic 2.5D FEM-BEM methodology used in the thesis for analysis of vibration and noise problems generated/induced by railway infrastructures. The chapter is divided into three sections. Sec. 3.1 presents the theoretical framework of the method used in thesis, Sec. 3.2 presents the novelties of the coupled 2.5D FEM-BEM developed in the thesis. The chapter concludes with the verification of the numerical methodology.

3.1 2.5D FEM-BEM

In this thesis, the 2.5D FEM-BEM methodology for modelling the track/tunnel/soil system is based on the formulation presented in [50], which uses a regularisation of the Green's function. The advantage of this methodology is the avoidance of explicit computation of singular terms on account of global regularisation of boundary element matrices. The simplicity of its implementation being its other advantage. In this method, the response is obtained by constructing a global stiffness matrix in a FEM framework. The structure/soil problem (tunnel/soil system in chapter 4 and track/tunnel/soil system in chapter 6) is modelled with the coupled 2.5D FEM-BEM and the equation for solving it is given by

$$[\mathbf{K}_0 - \mathrm{i}k_x\mathbf{K}_1 + k_x^2\mathbf{K}_2 + \bar{\mathbf{K}}_s - \omega^2\mathbf{M}]\bar{\boldsymbol{U}} = \bar{\boldsymbol{F}}, \tag{3.1}$$

where k_x is the wavenumber associated to the x coordinate (the Fourier image in x direction), ω is the angular frequency which takes into account the effect shift property of Fourier transform and

$$\omega = \tilde{\omega} + k_x v_t. \tag{3.2}$$

$\mathbf{K}_0$, $\mathbf{K}_1$ and $\mathbf{K}_2$ are the stiffness matrices related to the domain modelled with 2.5D FEM, $\mathbf{M}$ is the mass matrix of the structure and $\bar{\mathbf{K}}_s$ is the dynamic stiffness matrix of the soil obtained from the 2.5D BEM model. The stiffness and mass matrices of the structure are independent of the wavenumber and the frequency, while the stiffness matrix of the soil is a function of them. Moreover, $\bar{\boldsymbol{F}}$ represents the vector of external forces and $\bar{\boldsymbol{U}}$ is the vector of displacements, both defined in the 2.5D domain.

The stiffness matrix of the soil appearing in Eq. (3.1) is obtained by

$$\bar{\mathbf{K}}_s = \mathbf{T}_m\bar{\mathbf{U}}_b^{-1}[\bar{\mathbf{T}}_b + \mathbf{I}], \tag{3.3}$$

where, $\bar{\mathbf{T}}_b$, $\bar{\mathbf{U}}_b$ are matrices related to the Green's tractions and displacements computed on the boundary, respectively, $\mathbf{I}$ represents the identity matrix and $\mathbf{T}_m$ is the transformation matrix that converts the unknown nodal tractions on the boundary to nodal

forces. The later is given as $\mathbf{T}_m = \int \mathbf{N}^T \mathbf{N} \mathrm{d}S$, where $\mathbf{N}$ is the matrix of nodal shape functions of the boundary element discretisation. The unknown nodal tractions $\bar{\boldsymbol{T}}_b$ on the boundary can be found by solving the following boundary integral equation:

$$[\bar{\mathbf{T}}_b + \mathbf{I}]\bar{\boldsymbol{U}}_b = \bar{\mathbf{U}}_b\bar{\boldsymbol{T}}_b, \tag{3.4}$$

where $\bar{\boldsymbol{U}}_b$ is the vector of nodal displacements on the boundary and it is obtained by solving of Eq. (3.1). For the regularisation process applied in this approach, 2D static Green's function presented in App. A has been employed. Using this 2.5D FEM-BEM approach the structural velocity along the structure-acoustic interface can be obtained and, then, used as the input excitation for the acoustic model, with the assumption that the acoustic response does not affect the elastodynamic response of the building. This procedure is also adopted in Colaço et al. [65], who also describe the suitability of this approach. In this approach, structural damping is considered for the structures involved, treating the special case of the soil with the damping model presented at [74].

In this thesis, vectors are denoted by upper case bold italic letters and matrices and tensors are represented by upper case upright bold letters. Variable in wavenumber-frequency domain are denoted with a bar notation, variables in wavenumber-moving frequency domain are denoted with tilde notation while variables in frequency domain are denoted by capital letters. In this thesis a double Fourier transform is defined as

$$\bar{G}(k_x, \omega) = \int_{-\infty}^{+\infty} \int_{-\infty}^{+\infty} g(x, t)e^{\mathrm{i}(k_x x - \omega t)} \mathrm{d}x\mathrm{d}t, \tag{3.5}$$

for the transformation from the space-time domain to wavenumber-frequency domain and the anti-transform is defined as

$$g(x, t) = \frac{1}{4\pi^2} \int_{-\infty}^{+\infty} \int_{-\infty}^{+\infty} \tilde{G}(k_x, \omega)e^{-\mathrm{i}(k_x x - \omega t)} \mathrm{d}k_x\mathrm{d}\omega. \tag{3.6}$$

3.2   Fast computation of elastodynamic BEM matrices

The computation of the stiffness matrix of soil involves the computation of the BEM matrices related to traction and displacement. In order to obtain these matrices, the computation of traction and displacement Green's functions for a set of source and evaluation points is required. For a BEM mesh, the source points are placed on the BE nodes and the evaluators are given by the Gaussian integration points along all the BE. Thus, the computation of BEM matrices involves the computation of the Green's function for all combinations of source/evaluation points. It is important to note that

the more the amount of BE is, the larger the amount of source points and evaluators is and the higher the computational time for computing the BEM matrices becomes. In the method of François et al. [50] the Green's functions are computed on a grid of points and then an interpolation procedure is used to obtain the response at the required evaluators. However, interpolation could induce inaccurate results (with a sparse grid) or become computationally expensive (with a dense grid). In the present work, Green's functions are computed without the need for interpolation and in a computationally efficient way. Two strategies are discussed here which enables to accomplish this. The first strategy can be applied to any problem geometry. It involves fast computation of Green's function discussed in Sec. 3.2.1. The next strategy, discussed in Sec. 3.2.2, is only valid for a special class of problems encountered in underground railway infrastructures, specifically underground circular tunnels where the geometry of the system is axisymmetric,.

3.2.1   Fast computation of the Green's functions in a full-space

As discussed previously, the computational time associated to the calculation of the tractions and displacements Green's functions depends on the amount of source and evaluation points and on the number of discrete values for the wavenumber and the frequency. In a homogeneous full-space, the Green's functions are not a function of particular locations of the source and the evaluator: they are only a function of the relative distance between source and evaluation points. Relative distances between all source/evaluator combinations are contained in a smaller set of unique source/evaluator relative distances. Exploiting this fact, the fast computation of Green's functions is accomplished by computing the Green's function for this unique set of source/evaluator relative distances and then mapping them in order to obtain the Green's function for the complete set of source/evaluator combinations. This mapping also requires multiplying the Green's function with a transformation matrix that is described below. If all the BE of the BEM mesh have the same length, the unique set of source/evaluator combinations distances is the smallest. Exploiting this fact, the present methodology proposes to design the BEM mesh ensuring that all the elements have the same length.

In order to compute the Green's functions for displacement and traction for unique source/evaluator relative distances in the full-space, it should be noted that the dependency of the Green's functions for displacement and tractions on radial and angular coordinates can be separated into two functions: one only dependent on the relative radial distance and the other one only on the relative angle. The procedure to obtain the Green's function for any source/collocation point from the ones obtained at the unique source collocation point is as follows:

- Initially, the relative angles of all the source/evaluator combinations θ and the angles of the normals associated to all the evaluators ϕ are computed by

$$\phi = \arctan(n_y/n_z), \qquad \theta = \arctan(y/z), \tag{3.7}$$

where n_y and n_z are the normals and y and z are the relative distance in y and z directions.

- The normal are redefined as:

$$n_y = \cos(\phi - \theta), \quad n_z = \sin(\phi - \theta), \tag{3.8}$$

- The displacement and traction Green's functions for the unique set source/evaluator relative distances, which are represent by $\bar{\mathbf{H}}_{us}$ and $\bar{\mathbf{T}}_{us}$, respectively, are obtained using the Green's function provided in [25] considering $z = 0$.

- The displacement Green's functions at the required source/evaluators can be obtained as:

$$\bar{\mathbf{H}} = \mathbf{T}_\theta^{-1} \mathcal{M}(\bar{\mathbf{H}}_{us}) \mathbf{T}_\theta \tag{3.9}$$

where $\mathbf{T}_\theta$ is defined in Eq. (3.11) and $\mathcal{M}(.)$ represents the operation of the mapping from the unique set of source/evaluator relative distances to the required set of source/evaluator combinations.

- Similarly, the traction Green's functions can be obtained as

$$\bar{\mathbf{T}} = \mathbf{T}_\theta^{-1} (\mathcal{M}(\bar{\mathbf{T}}_{us}) \circ \mathbf{T}_\phi) \mathbf{T}_\theta \tag{3.10}$$

where

$$\mathbf{T}_\phi = \begin{bmatrix} n_y & n_y & n_z \\ n_y & n_y & n_z \\ n_z & n_z & n_y \end{bmatrix} \qquad \mathbf{T}_\theta = \begin{bmatrix} 1 & 0 & 0 \\ 0 & \cos\theta & -\sin\theta \\ 0 & \sin\theta & \cos\theta \end{bmatrix} \tag{3.11}$$

and where $\circ$ represents the Hadamard product. In this chapter, the Cartesian coordinates system that is used is referred in Fig. 3.1. The method presented in this section is derived in this coordinates system.

3.2.2 Axisymmetric formulation

The axisymmetric nature of circular tunnels can be used to take advantage in reducing the computation cost related to the calculation of the BEM traction and displacements matrices. To exploit the axisymmetry of the geometry, the boundary elements of the

BEM mesh must have the same length. In this case, the elements of the BEM matrices associated with all combinations of the sources and evaluators can be obtained from elements associated with only one source. This is possible because each source sees the same pattern of evaluators locations, with relative rotation between them. Thus, if the elements associated to a reference source are computed, the response for all the other combinations of source/evaluator distances can be easily obtained by multiplying these reference elements with a transformation matrix that takes into account the rotation between this reference source and the other ones. After this, appropriate mapping of the resulting elements should be performed. The transformation matrix having the relative rotation of the load points with respect to the axis of axisymmetry has the same form as $\mathbf{T}_\theta$ (mentioned in section 3.2.1) with angles θ that in this case are defined as the relative rotation between the required source points and the reference source point with respect to the axis of axisymmetry. The axisymmetric formulation is summarised as:

1. In a first step, all the elements for the reference source position and all the evaluator locations are computed.

2. The elements for other source/evaluator locations for all wavenumbers are obtained from the elements obtained in the first step by multiplying the elements with a transformation matrix.

3. The transformation matrix is $\mathbf{T}_\theta$ in Eq. (3.11) with angles θ defined as the relative rotation between the required source points and the reference source point with respect to the axis of axisymmetry.

4. In the final step, appropriate mapping and assembly of the elements is performed to obtain the final required BEM matrices of tractions and displacements.

Note: In cases of axisymetric geometries the displacements and tractions Green's functions are required to be computed only for the source points located on just one element, and then the mapping introduced in the Eq. (3.9) and Eq. (3.10) is required to performed once. Thus, the benefit of axisymteric formulation is further reducing the computation time.

3.3   Verification of the numerical methods

In this section, the verification of the numerical method developed in the thesis is presented. First, the verification of 2.5D BEM is presented followed by verification of 2.5D

FEM-BEM. The 2.5D FEM-BEM methodology is verified for the case of full-space and half-space.

3.3.1   Verification of 2.5D BEM

The boundary element method is validated by comparing the response of a cylindrical cavity in a full-space subjected to a unit 2.5D pressure load (Fig. 3.1). The cavity modelled by 2.5D BEM and semi-analytical solution of a cavity in a full-space provided by Gazis [75], has a radius of 1 m and the full-space is characterised by shear wave velocity $C_s = 150$ m/s and dilatational wave velocity $C_s = 300$ m/s and a material damping ratio $D_p = D_s = 0.025$. The pressure loading results in radial displacements in the full-space that is axisymmetric around the x-axis. The response of the cavity modelled by both method is computed for a frequency range of 80 Hz and wavenumber $k_x = k'_x C_s/\omega$ where k'_x is dimensionless wavenumber. Figure 3.2 shows the comparison of radial Green's displacements obtained by both methods at the boundary. Figure 3.3 shows the comparison of radial Green's displacements obtained by both methods at evaluator located at a radial distance of 10 m. The figures show a good agreement between both the methods thereby confirming the validation of 2.5D BEM.
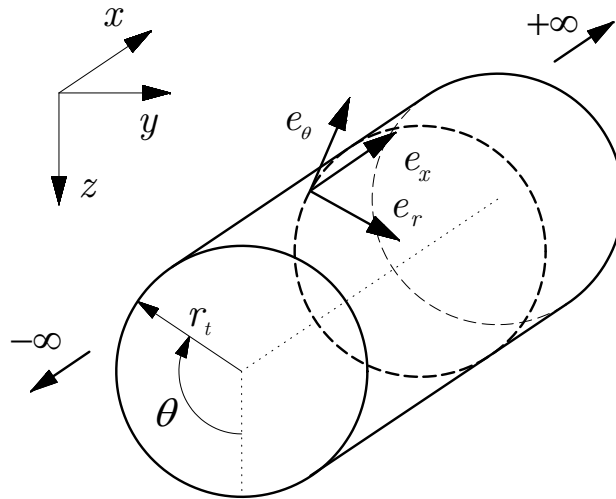
FIGURE 3.1: Cylindrical cavity in a full-space. Definition of the Cartesian and cylindrical coordinate systems for both semi-analytical and 2.5D FEM-BEM models.

3.3.2   Verification of 2.5D FEM-BEM

For validating of elastodynamic 2.5D FEM-BEM, a comparison is made with the semi-analytical solution of a cavity in a full-space provided by Gazis [75]. Cavity radius r_t of 1 m is considered. On the other hand, an equivalent 2.5D FEM-BEM model of this cavity
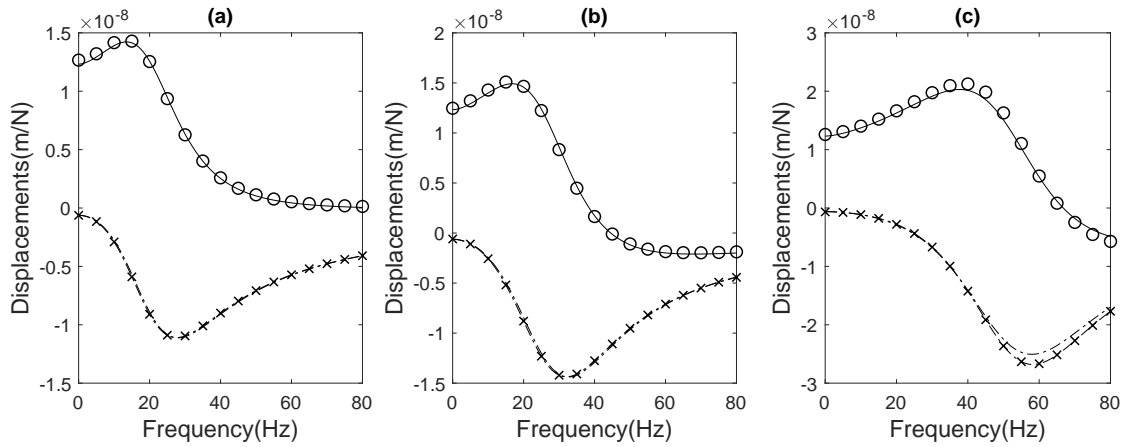
FIGURE 3.2: Green's function of displacement on the boundary, solid line represents the real part of Green's displacement by analytical method, 'o' markers the real part of Green's displacement by 2.5D BEM, dashed-dot line represents the imaginary part of Green's displacement by analytical method, 'x' markers represent the imaginary part of Green's displacement by 2.5D BEM.
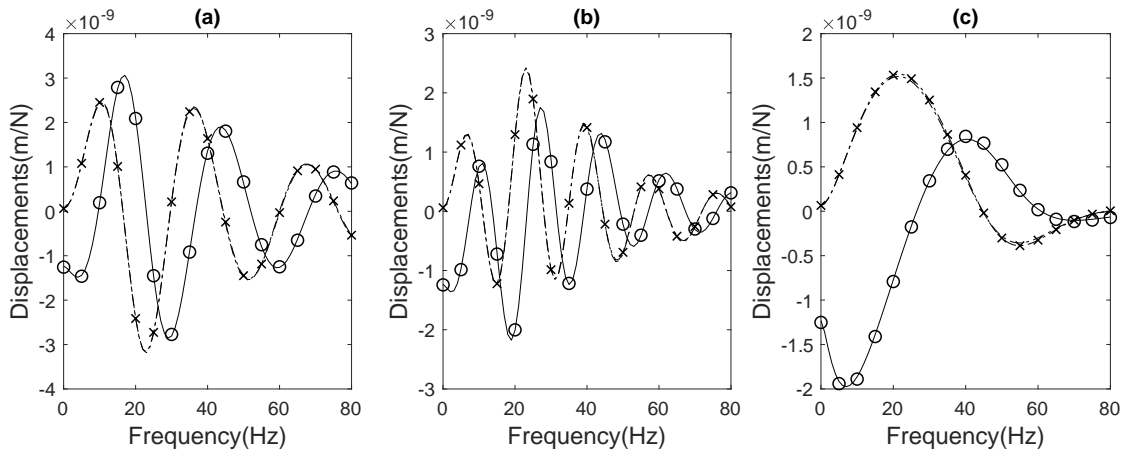
FIGURE 3.3: Green's function of displacement on the a point located at a radial distance of 10 m, solid line represents the real part of Green's displacement by analytical method, 'o' markers the real part of Green's displacement by 2.5D BEM, dashed-dot line represents the imaginary part of Green's displacement by analytical method,'x' markers represent the imaginary part of Green's displacement by 2.5D BEM.

in a full-space system has been constructed. In order to test the correctness of 2.5D FEM and 2.5D BEM implementations, the model is constructed by meshing a region close to the cavity with finite elements and the rest with boundary elements. Specifically, the region considered for the 2.5D FEM mesh is a circular ring of 0.2 m of thickness. The outer boundary of the circular ring is meshed with 80 linear boundary elements, while the 2.5D FEM mesh is based on linear triangular finite elements. An illustrative representation of the Cartesian and cylindrical coordinate systems associated with both models is presented in Fig. 3.1.

In both models, the cavity system is excited by a vertical unitary 2.5D load, which is

a point load in the y-z plane harmonically distributed in time and in x, applied at the inner boundary at $\theta = 0$. The properties of the medium that surrounds the cavity are summarized in the Table 3.1. For both models, the cavity response is computed for the frequencies up to 100 Hz and for the wavenumbers between -2π rad/m to 2π rad/m. The cavity displacement in the medium are computed for evaluators located at radial distance of 2 m from the center of the cavity and placed at angular locations θ of 0, $\pi/2$ rad, π rad and $3\pi/2$ rad.

Parameters	Notation	Units	Value
Young's modulus	E	[MPa]	108
Poisson ratio	ν	$[-]$	0.334
Density	ρ	[kg/m^3]	1800
Damping	$D_p = D_s$	$[-]$	0.025

TABLE 3.1: Properties of full-space used in the verification.

Figure 3.4 shows the results of the radial displacement in the full-space obtained for both models at all evaluators previously defined. From this results, it can be concluded that there is a very good agreement between the results obtained with 2.5D FEM-BEM and the semi-analytical solution of the cavity. This implies that the 2.5D elastodynamic FEM-BEM approach used in the framework of this article is properly verified. There is, however, a very slight mismatch in the results between the two methods at certain frequencies. Apart from the intrinsic errors related to the nature of mesh, the slight mismatch comes from the amount of ring modes considered [19] and the approximated model of a point load associated to the FEM approach.

In order to validate the model of the 2.5D FEM-BEM for half-space a comparison of the response of half-space modelled by EDT toolbox with an equivalent model modelled by 2.5D FEM-BEM. The equivalent model of half-space modelled by 2.5D FEM-BEM is modelled by rectangular geometry with a length of 1 m and a height of 1 m. Its surface modelled by linear triangular finite elements and the boundary is modelled with linear boundary elements.

The half-space modelled by both EDT and 2.5D FEM-BEM has the properties as given in Table 3.1. Both the EDT model and the 2.5D FEM-BEM model was excited by a vertical 2.5D point load. The response of both the models were obtained at two evaluators at ground surface one located at 2 m and the other located at 10 m from the centre of the geometry, in the frequency ranges of 80 Hz and wavenumber in the range of (0 to 1) rad/m.
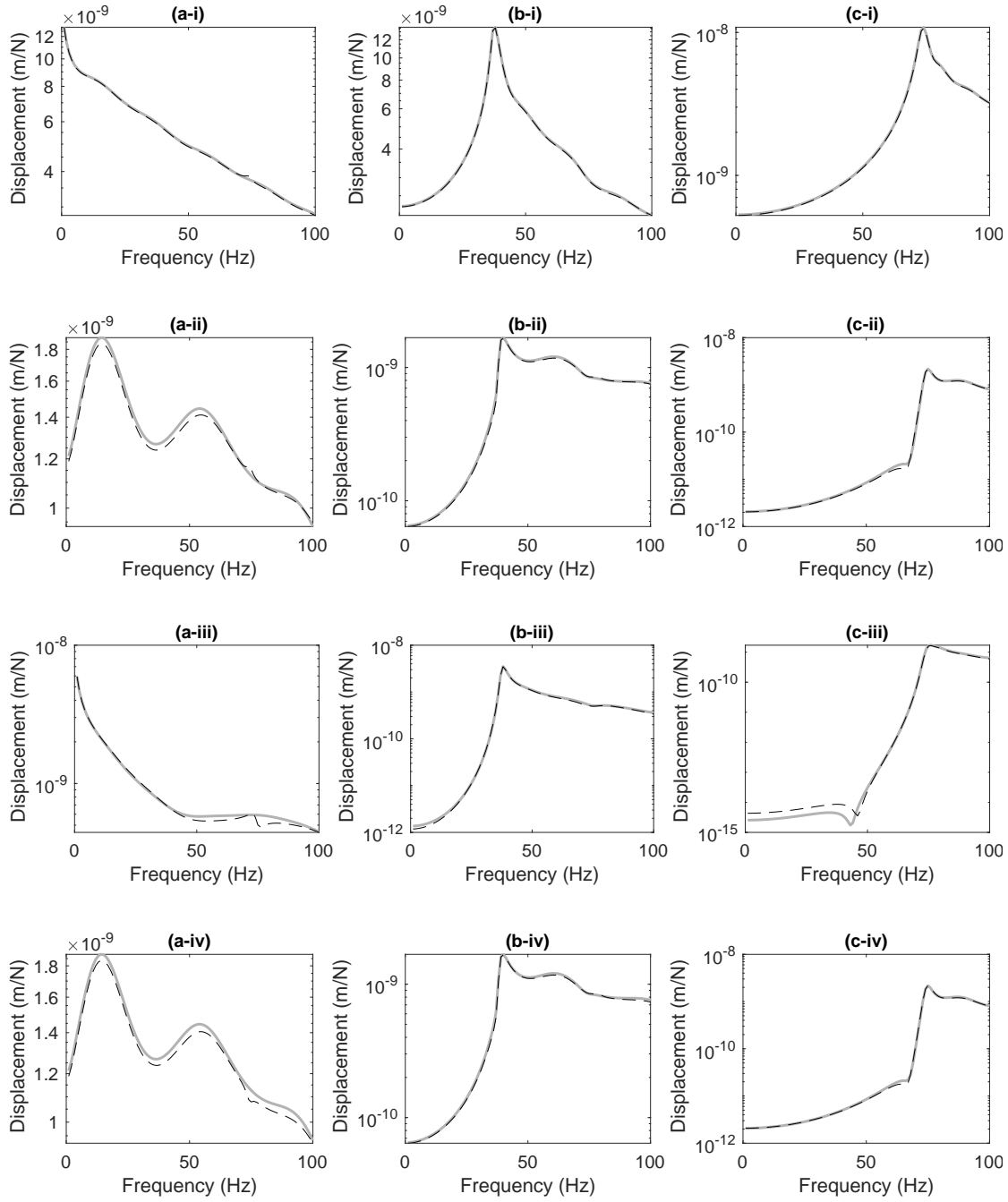
FIGURE 3.4: Green's functions of the radial displacement at specific wavenumbers obtained by the 2.5D FEM-BEM (dashed black line) and the semi-analytical cavity solution (grey solid line). The results are obtained at evaluators placed at a radial location of 2 m and at angular locations of 0 rad (i) $\pi/2$ rad (ii) π degrees (iii) and $3\pi/2$ rad (iv). (a) is referred to the response for $k_x = 0$, (b) to the response for $k_x = \pi/2$ rad/m and (c) to the response for $k_x = \pi$ rad/m.
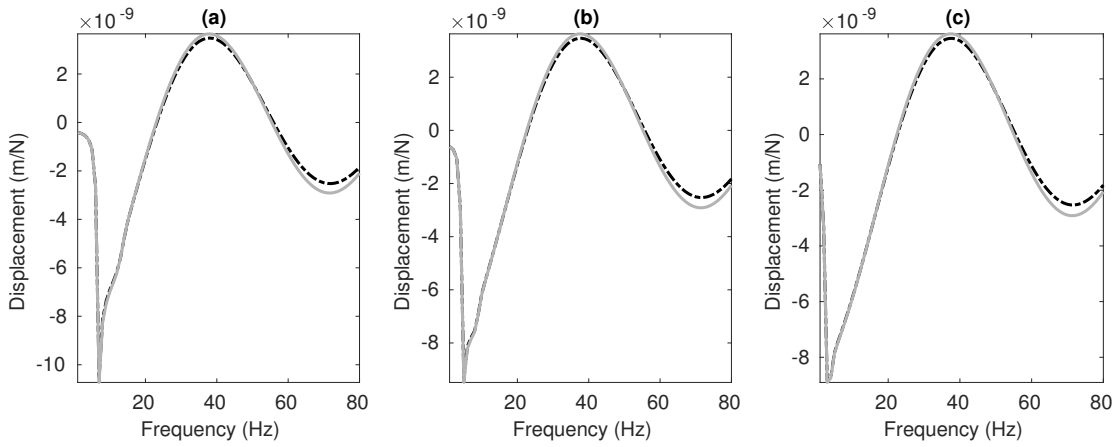
FIGURE 3.5: Imaginary part of vertical Green's displacements at 2m on ground surface obtained by EDT solution denoted by dashed-dotted line and by 2.5D FEM-BEM denoted by solid grey line, for $k_x = 0$ (a), $k_x = 0.5$ (a) and $k_x = 1$ (c).
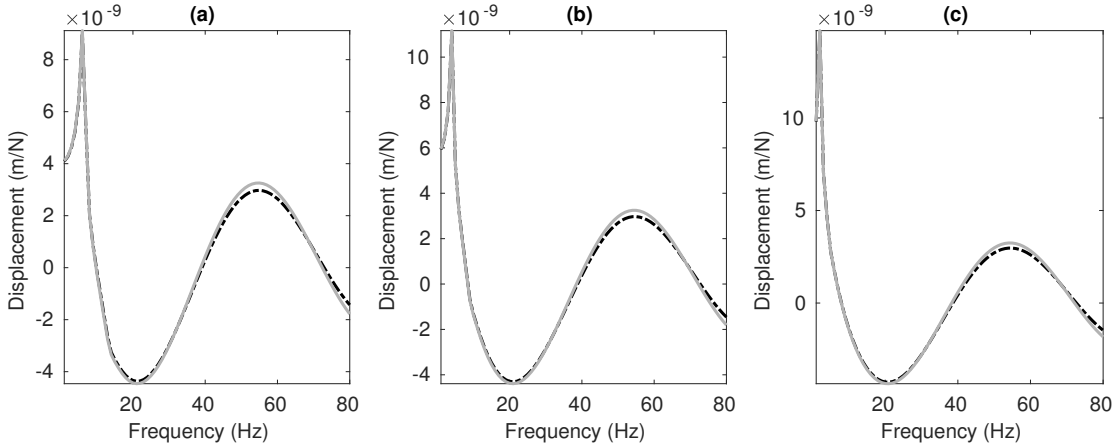
FIGURE 3.6: Real part of vertical Green's displacements at 2m on ground surface obtained by EDT solution denoted by dashed-dotted line and by 2.5D FEM-BEM denoted by solid grey line, for $k_x = 0$ (a), $k_x = 0.5$ (a) and $k_x = 1$ (c).

Figure 3.8 shows real and Fig. 3.7 shows the imaginary part of vertical Green's displacement at a receiver located on ground surface. Figure 3.6 shows real and Fig. 3.5 shows the imaginary part of vertical Green's displacement at a receiver located on the ground surface obtained by both methods for $k_x = (0, 0.5, 1)$ in frequency range of 80 Hz. From the figure it can be said that there is a good agreement between the methods. Thus it can be said that the 2.5D FEM-BEM for half-space is also verified.
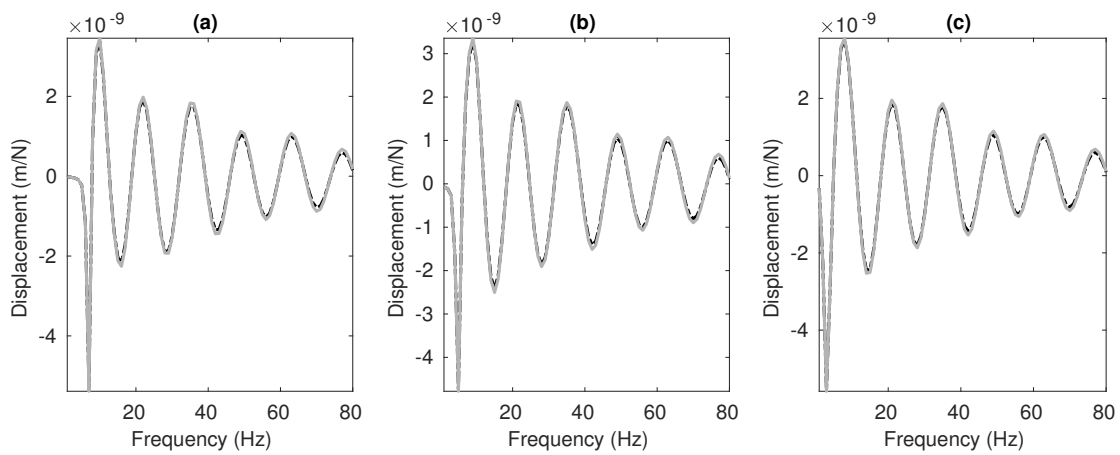
FIGURE 3.7: Imaginary part of vertical Green's displacements at 10m on ground surface obtained by EDT solution denoted by dashed-dotted line and by 2.5D FEM-BEM denoted by solid grey line, for $k_x = 0$ (a), $k_x = 0.5$ (a) and $k_x = 1$ (c).
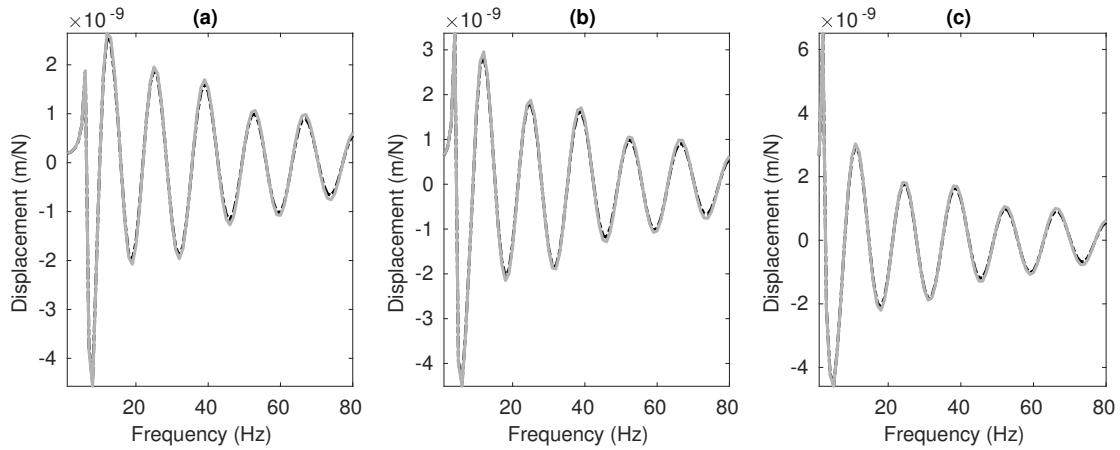
FIGURE 3.8: Real part of vertical Green's displacements at 10m on ground surface obtained by EDT solution denoted by dashed-dotted line and by 2.5D FEM-BEM denoted by solid grey line, for $k_x = 0$ (a), $k_x = 0.5$ (a) and $k_x = 1$ (c).

Chapter 4

Methodology for the vibration energy flow computation radiated by circular tunnels

Considering only a model for the vehicle/track/tunnel/soil system that accounts for the surrounding soil as a full-space is a computationally efficient approach for the evaluation of vibration mitigation measures applied on the source, rather than accounting for the complete system. In this regard, vibration energy flow is a tool that can be used in designing effective countermeasures for reducing the vibration generated by underground railway infrastructures.

Hussein et al [76] proposed a power-flow study based on the PiP model of [19, 21]. The model was later improved by [26], who replaced the initial full-space with a layered half-space. In order to obtain power-flow from double-deck tunnel [77, 78] proposed some modification to the PiP model. By coupling a plate which models the upper floor in a double-deck tunnel, with the PiP model, the case of the double-deck tunnel was approximated. Thus allowing for computation of vibration energy flow from the double-deck tunnel.

Limitation of the above methodologies is that power-flow from only simple geometrical configurations of underground tunnel infrastructures can be analysed, in reality, underground tunnel infrastructures are more complex and as such, there is a need to develop tools that can facilitate the computation of vibration energy flow from these infrastructures. Thus in this chapter, a methodology to compute vibration energy flow radiated by underground infrastructures is proposed.

4.1 Numerical method

As previously stated, the aim of this chapter is to present a new methodology for the computation of vibration energy flow radiated in the soil from underground infrastructure by train traffic. The global computation scheme of the methodology is shown in Fig. 4.1. This computation scheme consists of four different models: the track/tunnel/soil model, the train/track interaction model, the train pass-by response model and the vibration energy flow computation.
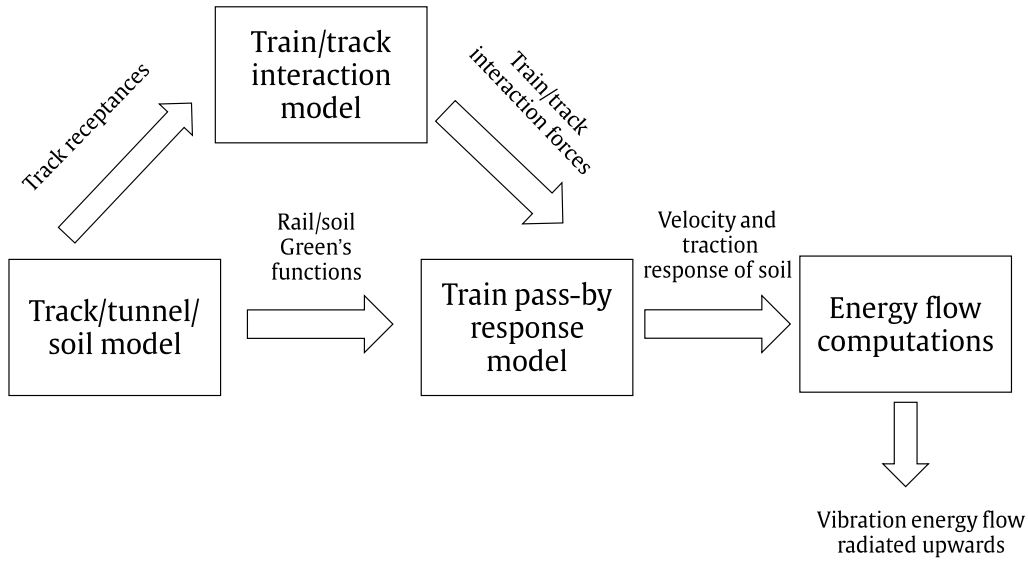
FIGURE 4.1: Schematic description of the methodology.

By its side, the track/tunnel/soil system consists of three models: a semi-analytical model of the track, a model based on a 2.5D FEM-BEM approach for the tunnel/soil system and the semi-analytical solutions of a cylindrical cavity in a full-space as a model of the vibration propagation in the soil. In the semi-analytical model of the track, the rails are modelled as Euler-Bernoulli beams and the fasteners as longitudinally distributed linear viscous springs. Tunnel/soil modelling is accomplished in the basis of a 2.5D FEM-BEM wherein the tunnel structure is modelled by FE and the local surrounding soil is modelled with BE. The connection between to tunnel/soil model and the semi-analytical solutions of the cylindrical cavity is done through the displacements on the tunnel/soil interface, which are obtained with the 2.5D FEM-BEM model of the tunnel/soil system and then they are used as boundary conditions in the semi-analytical solutions of the cavity in order to obtain the displacements and the tractions at arbitrary points in the soil.

As shown in Fig. 4.1, the coupled model of the train/track/tunnel/soil system is solved in two steps. In the initial step, the track receptances in the moving frame of reference obtained by the 2.5D FEM-BEM model are used together with the train/track interaction model to compute the wheel/rail interaction forces in the frequency domain. The train/interaction model mainly consists of a rigid multibody model of the vehicle and a wheel/rail contact model based on Hertz contact theory. In the next step, the wheel/rail interaction forces and the Green's function of the system between the rails and the soil (or other points on the system where the vibration response due to a train pass-by is

desired to be computed) are used together in the train pass-by response model to obtain the vibration and/or tractions response in selected evaluators. Finally, the vibration energy flow can be obtained in the soil by using velocity and traction responses in a set of points located in the soil around the tunnel. The details of each model used for obtaining the vibration response or the vibration energy flow in the soil are described in the following sections.

4.2   Modelling of the track/tunnel/soil system

As previously introduced, the response of the track/tunnel/soil system is obtained with the numerical methodology that consists of a 2.5D FEM-BEM approach to model the tunnel and the local surrounding soil, a semi-analytical model of the track and a semi-analytical model of a cylindrical cavity in a full-space used for the vibration propagation in the soil. These models are explained in subsections 3.1, 4.2.1 and 4.2.2, respectively. The 2.5D FEM-BEM coupled with the track model is used to obtain the Green's functions of the track/tunnel/soil system in the tunnel/soil interface due to vertical forces applied at the rails, while the semi-analytical solutions of the cavity are used to obtain the displacements and traction in the soil using the displacements obtained at the tunnel/soil interface as input boundary conditions. Being more specific, the track/tunnel/soil model presented in this work is constructed carrying out the following steps:

- Initially, the displacement Green's functions at the tunnel/soil interface (and other desired evaluators) due to a set of vertical forces applied at the FE nodes to be in contact with the rails are computed using the 2.5D FEM-BEM approach described in subsection 3.1.

- The rails are then coupled to the tunnel/soil model to obtain the Green's functions of the coupled track/tunnel/soil system at all the desired evaluators due to vertical forces on the rails.

- The tunnel/soil interface displacement Green's functions obtained in Cartesian coordinates are transformed into a cylindrical coordinates system.

- Using these tunnel/soil interface displacement Green's functions, the Fourier coefficients of the semi-analytical solutions of a cylindrical cavity in a full-space can be found.

- Using these coefficients, the tractions and displacement Green's functions at all the evaluators in the soil due to vertical forces on the rails are computed.

4.2.1   Track model and its coupling with the tunnel structure

In the methodology used in this thesis, it is proposed to use a semi-analytical model of the track coupled the 2.5D FEM-BEM model of the tunnel/soil system. In this semi-analytical model of the track, the rails are modelled as two identical Euler- Bernoulli beams of infinite length and the fasteners are modelled as continuously distributed linear massless viscous springs. Both rails and the fasteners are considered to have the same mechanical parameters, being E_r the Young's modulus of the rail material, I_r the second moment of inertia of the rail cross section, ρ_r the density of the rail material, S_r the rail cross-sectional area and k_f and c_f are the stiffness and viscous damping of the fasteners, respectively. Thus, the expression that defines the dynamic behaviour of the rails excited by moving harmonic vertical point loads with the same excitation frequency $\tilde{\omega}$ and the same speed v_t can be expressed in the wavenumber-frequency domain as

$$[E_r I_r k_x^4 - \rho_r S_r \omega^2]\bar{\boldsymbol{Z}}_r + (k_f + \mathrm{i}\omega c_f)(\bar{\boldsymbol{Z}}_r - \bar{\boldsymbol{Z}}_{tr}) = 2\pi\delta(\tilde{\omega} - (\omega + k_x v_t))\bar{\boldsymbol{F}}_r, \qquad (4.1)$$

where $\bar{\boldsymbol{Z}}_r = \{\bar{Z}_{r_1}\ \bar{Z}_{r_2}\}^T$ are the vertical displacements of the first and second rails and $\bar{\boldsymbol{Z}}_{tr} = \{\bar{Z}_{tr_1}\ \bar{Z}_{tr_2}\}^T$ are the equivalent vertical displacements of tunnel below the first and second rails. These equivalent vertical displacements are obtained by averaging the responses at the FE nodes of the tunnel that should be in contact with the rails induced by the set of vertical forces applied at these nodes. The response of the tunnel below the rails is given by

$$\bar{\boldsymbol{Z}}_{tr} = \bar{\mathbf{H}}_{tr}^{tr}\bar{\boldsymbol{F}}_{tr}, \qquad (4.2)$$

where $\bar{\boldsymbol{F}}_{tr} = \{\bar{F}_{tr_1}\ \bar{F}_{tr_2}\}^T$ are the equivalent vertical forces applied on the system below first and second rails and $\bar{\mathbf{H}}_{tr}^{tr}$ are the Green's functions that relates the equivalent vertical displacements of the tunnel below the rails with the equivalent vertical forces applied also there, which can be obtained by the 2.5D FEM-BEM model of the tunnel/soil described in the previous section. Moreover, the forces $\bar{\boldsymbol{F}}_{tr}$ can be expressed in terms of the displacements of the rails and the equivalent vertical displacements of the tunnel below the rails as shown in Eq. (4.1) as

$$\bar{\boldsymbol{F}}_{tr} = (k_f + \mathrm{i}\omega c_f)(\bar{\boldsymbol{Z}}_r - \bar{\boldsymbol{Z}}_{tr}). \qquad (4.3)$$

Combining Eqs. (4.2) and (4.3), the relation the displacements of the rails and the equivalent vertical displacements of the tunnel below the rails can be written as

$$\bar{\boldsymbol{Z}}_{tr} = \left(\frac{1}{k_f + \mathrm{i}\omega c_f}\mathbf{I} + \bar{\mathbf{H}}_{tr}^{tr}\right)^{-1}\bar{\mathbf{H}}_{tr}^{tr}\bar{\boldsymbol{Z}}_r. \qquad (4.4)$$

Inserting Eq. (4.4) in Eq. (4.1), the response of the rails can be written as

$$\left[(E_r I_r k_x^4 - \rho_r S_r \omega^2)\mathbf{I} + \bar{\mathbf{K}}_{ft}\right] \bar{\mathbf{Z}}_r = 2\pi\delta(\tilde{\omega} - (\omega - k_x v))\bar{\mathbf{F}}_r, \tag{4.5}$$

where,

$$\bar{\mathbf{K}}_{ft} = (k_f + \mathrm{i}\omega c_f)\left[\mathbf{I} - \left(\frac{1}{k_f + \mathrm{i}\omega c_f}\mathbf{I} + \bar{\mathbf{H}}_{tr}^{tr}\right)^{-1}\bar{\mathbf{H}}_{tr}^{tr}\right]. \tag{4.6}$$

Thus, the Green's functions of the vertical displacements of the rails due vertical forces on them in the moving frame of reference $\tilde{\mathbf{H}}_r^r$ are given by

$$\tilde{\mathbf{H}}_r^r = \left[\left[E_r I_r k_x^4 - \rho_r S_r\left(\tilde{\omega} + k_x v_t\right)^2\right]\mathbf{I} + \tilde{\mathbf{K}}_{ft}\right]^{-1}, \tag{4.7}$$

where $\tilde{\mathbf{K}}_{ft} = \tilde{\mathbf{K}}_{ft}(k_x, \tilde{\omega}) = \bar{\mathbf{K}}_{ft}(k_x, \tilde{\omega} + k_x v_t)$.

Then, the Green's functions that relate the response of the tunnel/soil system coupled with rails due to the vertical forces on the rails in the moving frame of reference $\tilde{\mathbf{H}}_s^r$ are given by

$$\tilde{\mathbf{H}}_s^r = \tilde{\mathbf{H}}_s^{tr}\tilde{\mathbf{K}}_{ft}\tilde{\mathbf{H}}_r^r, \tag{4.8}$$

being

$$\tilde{\mathbf{H}}_s^r = \left\{\tilde{\mathbf{H}}_s^{r_1} \quad \tilde{\mathbf{H}}_s^{r_2}\right\}, \quad \tilde{\mathbf{H}}_s^{tr} = \left\{\tilde{\mathbf{H}}_s^{tr_1} \quad \tilde{\mathbf{H}}_s^{tr_2}\right\}, \tag{4.9}$$

where $\tilde{\mathbf{H}}_s^{tr}$ are the Green's functions of the tunnel/soil system due to forces applied below the rails, which can be obtained using the 2.5D FEM-BEM approach presented in the previous section considering that $\tilde{\mathbf{H}}_s^{tr} = \tilde{\mathbf{H}}_s^{tr}(k_x, \tilde{\omega}) = \bar{\mathbf{H}}_s^{tr}(k_x, \tilde{\omega} + k_x v_t)$. In case that external mitigation measures are desired to be applied on the system, they can be coupled to the tunnel/soil system in the same way that rails are. For these cases, the Green's function of the system due to external forces applied at any arbitrary position of the tunnel/soil in the presence of the rails $\bar{\mathbf{H}}_s^{er}$ can be written as

$$\bar{\mathbf{H}}_s^{er} = \bar{\mathbf{H}}_s^e + k_{ft}^e\bar{\mathbf{H}}_s^{tr}\bar{\mathbf{H}}_{tr}^e, \tag{4.10}$$

where the sub-index or super-index e represents the external loading and

$$k_{ft}^e = (k_f + \mathrm{i}\omega c_f)\left(\frac{k_f + \mathrm{i}\omega c_f}{E_r I_r k_x^4 - \rho_r S_r \omega^2 + k_f + \mathrm{i}\omega c_f} - 1\right), \tag{4.11}$$

and where $\bar{\mathbf{H}}_s^e$ are the Green's functions of the tunnel/soil system due to external forces in the absence of the rails and $\bar{\mathbf{H}}_{tr}^e$ are the Green's functions of the response of the tunnel below the rails due to the external loads in the absence of the rails. Finally, the Green's functions associated to the response of the rails due to external loading can be written

as

$$\bar{\mathbf{H}}_r^e = k_{fr}^e \bar{\mathbf{H}}_{tr}^e, \tag{4.12}$$

where

$$k_{fr}^e = \frac{k_f + \mathrm{i}\omega c_f}{E_r I_r k_x^4 - \rho_r S_r \omega^2 + k_f + \mathrm{i}\omega c_f}. \tag{4.13}$$

Eqs. (4.10) and (4.12) are not defined in the moving frame of reference because the external loads are not usually moving with the train. Again, the Green's functions $\bar{\mathbf{H}}_s^{tr}$, $\bar{\mathbf{H}}_s^e$ and $\bar{\mathbf{H}}_{tr}^e$ can be computed using the 2.5D FEM-BEM approach presented in the previous section.

4.2.2 Model for the vibration propagation in the soil

The proposed 2.5D FEM-BEM approach used for modelling the tunnel/soil system cannot be used to obtain the tractions in the soil. For this reason, the semi-analytical solutions of a circular cavity in a full-space [75, 19] are used to relate displacements in the tunnel/soil interface with displacements and tractions at arbitrary points in the soil. In this model, the displacements in the soil at an arbitrary radial distance from the center of the tunnel r can be expressed as

$$\bar{\boldsymbol{U}}_s(k_x, \omega, r, \theta) = \sum_{n=0}^{\infty} [\mathbf{S}_n^s(\theta)\bar{\boldsymbol{U}}_n^s(k_x, \omega, r) + \mathbf{S}_n^a(\theta)\bar{\boldsymbol{U}}_n^a(k_x, \omega, r)], \tag{4.14}$$

where

$$\bar{\boldsymbol{U}}_s = \left\{ \bar{U}_{sr} \quad \bar{U}_{s\theta} \quad \bar{U}_{sx} \right\}^{\mathrm{T}}, \qquad \bar{\boldsymbol{U}}_n^i = \left\{ \bar{U}_{nr}^i \quad \bar{U}_{n\theta}^i \quad \bar{U}_{nx}^i \right\}^{\mathrm{T}}, \tag{4.15}$$

where $i = s$ for the symmetric case and $i = a$ for the anti-symmetric case (this definition holds all along the present subsection), and

$$\mathbf{S}_n^s = \begin{bmatrix} \cos n\theta & 0 & 0 \\ 0 & \sin n\theta & 0 \\ 0 & 0 & \cos n\theta \end{bmatrix}, \qquad \mathbf{S}_n^a = \begin{bmatrix} \sin n\theta & 0 & 0 \\ 0 & \cos n\theta & 0 \\ 0 & 0 & \sin n\theta \end{bmatrix}, \tag{4.16}$$

where $\bar{\boldsymbol{U}}_n^s$ and $\bar{\boldsymbol{U}}_n^a$ are the symmetric and anti-symmetric contributions to n-th ring mode of the displacements $\bar{\boldsymbol{U}}_s$. In Fig. 3.1, the Cartesian and cylindrical coordinate systems for both semi-analytical and 2.5D FEM-BEM models are defined.

At a generic radius r, the $n = 0$ component of the displacement $\bar{\boldsymbol{U}}_s(k_x, \omega, r, \theta)$ can be computed at the tunnel/soil interface as

$$\bar{U}_{0r}^s(k_x, \omega, r) = \frac{1}{2\pi} \int_0^{2\pi} \bar{U}_{sr}(k_x, \omega, r, \theta) \mathrm{d}\theta,$$
$$\bar{U}_{0\theta}^s(k_x, \omega, r) = 0, \tag{4.17}$$
$$\bar{U}_{0x}^s(k_x, \omega, r) = \frac{1}{2\pi} \int_0^{2\pi} \bar{U}_{sx}(k_x, \omega, r, \theta) \mathrm{d}\theta,$$

$$\bar{U}_{0r}^a(k_x, \omega, r) = 0,$$
$$\bar{U}_{0\theta}^a(k_x, \omega, r) = \frac{1}{2\pi} \int_0^{2\pi} \bar{U}_{s\theta}(k_x, \omega, r, \theta) \mathrm{d}\theta, \tag{4.18}$$
$$\bar{U}_{0x}^a(k_x, \omega, r) = 0.$$

For the case of a generic ring mode $n > 0$, these expressions become

$$\bar{U}_{nr}^s(k_x, \omega, r) = \frac{1}{\pi} \int_0^{2\pi} \bar{U}_{sr}(k_x, \omega, r, \theta) \cos(n\theta) \mathrm{d}\theta,$$
$$\bar{U}_{n\theta}^s(k_x, \omega, r) = \frac{1}{\pi} \int_0^{2\pi} \bar{U}_{s\theta}(k_x, \omega, r, \theta) \sin(n\theta) \mathrm{d}\theta, \tag{4.19}$$
$$\bar{U}_{nx}^s(k_x, \omega, r) = \frac{1}{\pi} \int_0^{2\pi} \bar{U}_{sx}(k_x, \omega, r, \theta) \cos(n\theta) \mathrm{d}\theta,$$

$$\bar{U}_{nr}^a(k_x, \omega, r) = \frac{1}{\pi} \int_0^{2\pi} \bar{U}_{sr}(k_x, \omega, r, \theta) \sin(n\theta) \mathrm{d}\theta,$$
$$\bar{U}_{n\theta}^a(k_x, \omega, r) = \frac{1}{\pi} \int_0^{2\pi} \bar{U}_{s\theta}(k_x, \omega, r, \theta) \cos(n\theta) \mathrm{d}\theta, \tag{4.20}$$
$$\bar{U}_{nx}^a(k_x, \omega, r) = \frac{1}{\pi} \int_0^{2\pi} \bar{U}_{sx}(k_x, \omega, r, \theta) \sin(n\theta) \mathrm{d}\theta,$$

Consider the soil/tunnel interface, which is located at a radius r_b from the centre of the tunnel. For this radius, one can write the expressions

$$\bar{\boldsymbol{U}}_n^i(k_x, \omega, r_b) = \bar{\mathbf{U}}_{cn}^i(k_x, \omega, r_b) \bar{\boldsymbol{C}}_n^i, \tag{4.21}$$

where $\bar{\mathbf{U}}_{cn}^s$ is the matrix $\mathbf{U}$ defined by [19], $\bar{\mathbf{U}}_{cn}^a$ can be obtained from $\bar{\mathbf{U}}_{cn}^s$ using the transformation proposed at the appendix of [21] and $\bar{\boldsymbol{C}}_n^s$ and $\bar{\boldsymbol{C}}_n^a$ are the unknown Fourier coefficients. Since the displacements at soil/tunnel interface are known, Eqs. (4.17) to (4.20) can be used to obtain $\bar{\boldsymbol{U}}_n^s(k_x, \omega, r_b)$ and $\bar{\boldsymbol{U}}_n^a(k_x, \omega, r_b)$. Then, the unknown Fourier coefficients can be found by inverting Eq. (4.21).

After obtaining the Fourier coefficients $\bar{\boldsymbol{C}}_n^s$ and $\bar{\boldsymbol{C}}_n^a$, the symmetric and anti-symmetric terms for displacements and tractions at any radial location in the soil r_f can be found

by

$$\bar{\boldsymbol{U}}_n^i(k_x, \omega, r_f) = \bar{\mathbf{U}}_{cn}^i(k_x, \omega, r_f)\bar{\boldsymbol{C}}_n^i, \tag{4.22}$$

and

$$\bar{\boldsymbol{T}}_n^i(k_x, \omega, r_f) = \bar{\mathbf{T}}_{cn}^i(k_x, \omega, r_f)\bar{\boldsymbol{C}}_n^i, \tag{4.23}$$

where $\bar{\mathbf{T}}_{cn}^s$ and $\bar{\mathbf{T}}_{cn}^a$ are the matrices $\mathbf{T}$ defined in [19, 21] and the contribution $\bar{\boldsymbol{T}}_n^s(k_x, \omega, r_f)$ and $\bar{\boldsymbol{T}}_n^a(k_x, \omega, r_f)$ can be found following an analogous process to the one performed for the displacements. Then, the displacements in the soil can be obtained by applying Eq. (4.14) for $r = r_f$. The equivalent expression can be used for the tractions, being

$$\bar{\boldsymbol{T}}_s(k_x, \omega, r_f, \theta) = \sum_{n=0}^{\infty}[\mathbf{S}_n^s(\theta)\bar{\boldsymbol{T}}_n^s(k_x, \omega, r_f) + \mathbf{S}_n^a(\theta)\bar{\boldsymbol{T}}_n^a(k_x, \omega, r_f)]. \tag{4.24}$$

4.2.3   Verification of the tunnel/soil model

In this section, the verification of the numerical methodology to obtain the tractions in the soil is presented. The verification is done on the basis of a system consisting of a cylindrical cavity in a homogeneous full-space. A cavity radius r_t of 1 m is considered and the mechanical parameters of the full-space are presented in Table 3.1. Two models of this system are compared in this verification: on one hand, the semi-analytical solutions of a cylindrical cavity in a full-space provided by [75] constitute the reference solution; on the other hand, an equivalent 2.5D FEM-BEM model of this cavity in a full-space system has been constructed meshing a region close to the cavity with finite elements and the rest with boundary elements. The region considered for 2.5D FEM mesh is a circular ring of 0.2 m thickness meshed with linear triangular elements. The outer boundary of the circular ring has been meshed by 80 linear boundary elements. Displacements at the nodes of the boundary elements are used as boundary conditions for the vibration propagation model presented in subsection 4.2.2.

For both the models, the traction Green's functions due to a vertical force applied at the inner boundary of the cavity and at $\theta = 0$ are computed for frequencies up to 100 Hz and for wavenumbers from -2π rad/m to 2π rad/m. Tractions are computed by both models for evaluators located at a radial distance of 2 m from the centre of the cavity and placed at angular locations θ of 0, $\pi/2$ rad, π rad and $3\pi/2$ rad. Figure 4.2 shows the results of the radial tractions obtained by both models at all evaluators previously defined. From this results, it can be concluded that there is a very good agreement between the results obtained with the proposed numerical methodology and the reference theoretical solution. This implies that the numerical methodology used in the framework of this thesis is properly verified. There is, however, a very slight mismatch in the

results between the two methods at certain frequencies. Apart from the intrinsic errors related to the nature of mesh, the slight mismatch comes from the number of ring modes considered [19] and the approximation done in the context of the 2.5D FEM model of the tunnel to approach a theoretical point load.

4.3 Train/track interaction and train pass-by response models

For modelling the train/track interaction, two components of load are considered. The quasi-static loads, that results from the movement of the static loads corresponding to the weight of the train and the dynamic loads due to the dynamic interaction between the train and the track. The train/track dynamic interaction used assumes that the wheel/rail contact can be modelled as a linearised Hertzian contact between two crossed cylinders of different radius, as models of the wheel and the rail in the point of view of the contact. The classical Hertzian contact expression for this problems is linearised around the static load, obtaining an expression that linearly relates the vertical displacement of the wheel z_w, the vertical displacement of the rail z_r, the rail unevenness ε_r and the wheel/rail contact dynamic load $f_{w/r}$

$$f_{w/r} = k_H \left(z_w - z_r + \varepsilon_r\right), \tag{4.25}$$

where k_H is the stiffness of the linearised Hertzian contact. Performing the train/track interaction in the framework of a moving frame of reference associated to a train motion, the frequency associated to this problem is $\tilde{\omega}$ [9], in accordance with the derivation in subsection 4.2.1. Thus, all the variables represented in the frequency domain in the present section are associated to the frequency $\tilde{\omega}$, except when it is specifically mentioned otherwise. Transforming Eq. (4.25) to the frequency domain, grouping all the wheel/rail contacts in one expression and operating, the train/track interaction problem can be solved in the frequency domain by

$$\begin{Bmatrix} \boldsymbol{F}_{r_1}^{w/r} \\ \boldsymbol{F}_{r_2}^{w/r} \end{Bmatrix} = \left(\begin{bmatrix} \mathbf{H}_v^{w/r} & \\ & \mathbf{H}_v^{w/r} \end{bmatrix} + \begin{bmatrix} \mathbf{H}_{r_1 r_1}^{w/r} & \mathbf{H}_{r_1 r_2}^{w/r} \\ \mathbf{H}_{r_2 r_1}^{w/r} & \mathbf{H}_{r_2 r_2}^{w/r} \end{bmatrix} + k_H^{-1}\mathbf{I} \right)^{-1} \begin{Bmatrix} \boldsymbol{E}_{r_1} \\ \boldsymbol{E}_{r_2} \end{Bmatrix}, \tag{4.26}$$

where $\boldsymbol{F}_{r_i}^{w/r}$ is the vector of the train/track dynamic interaction loads associated to the i-th rail, $\mathbf{H}_v^{w/r}$ is receptance matrix of a 2D vehicle model at the contact points with the track for one rail, $\mathbf{H}_{r_i r_j}^{w/r}$ is the receptance matrix of the i-th at the interaction points with the vehicle due to forces applied in the interaction points of the j-th rails, k_H is linearised
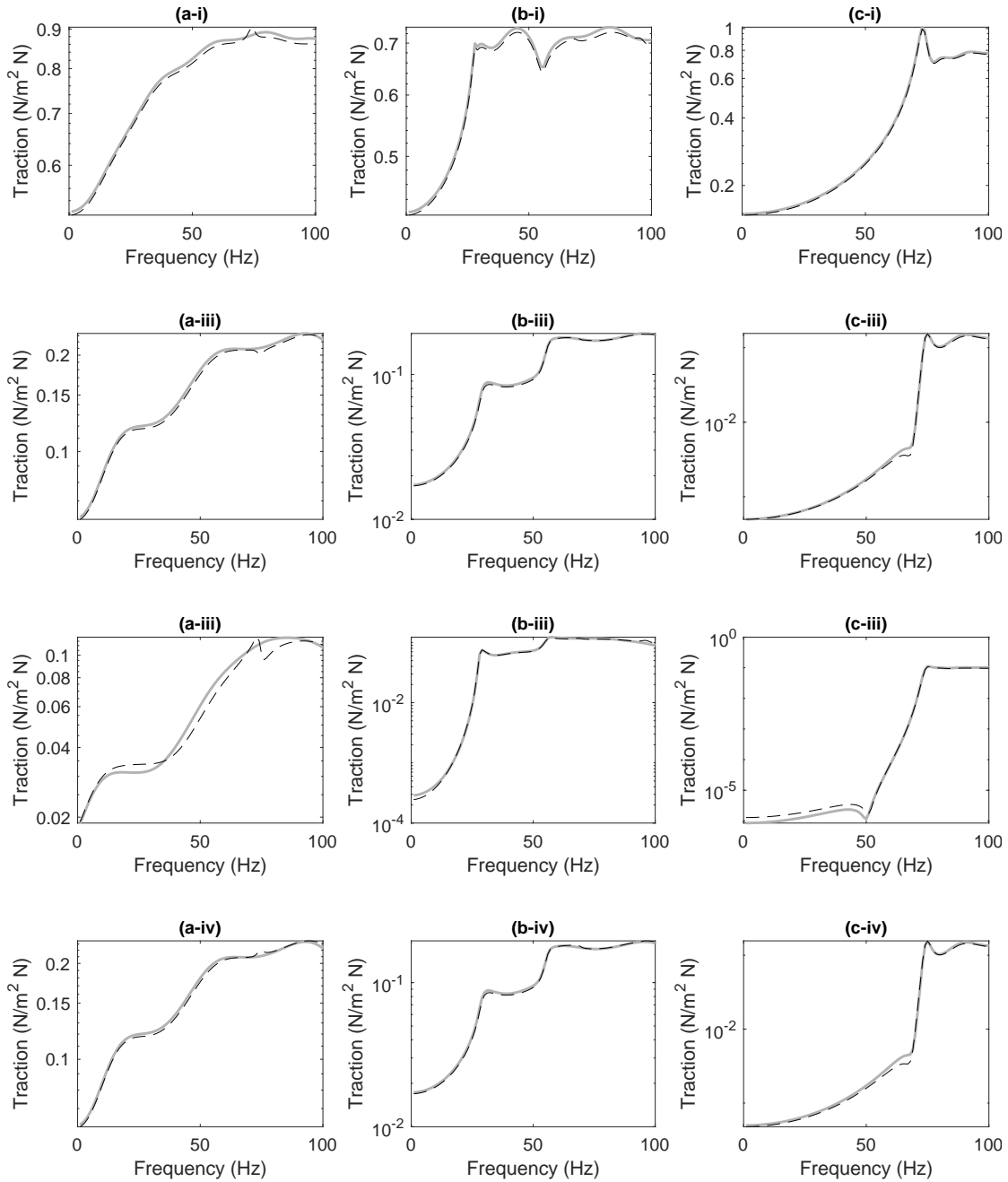
FIGURE 4.2: Green's functions of the radial tractions obtained by the numerical methodology presented in this thesis (dashed black line) and the semi-analytical model of a cavity in a full-space (grey solid line). The results are obtained at evaluators placed at a radius of 2 m and at angular positions of 0 rad (i) $\pi/2$ rad (ii) π degrees (iii) and $3\pi/2$ rad (iv). The results are associated to the wavenumbers of 0 (a), $\pi/2$ rad/m (b) and π rad/m (c).

Hertzian spring considered to be the same in all the contacts, $\mathbf{I}$ is identity matrix and $\boldsymbol{E}_{r_i}$ is the vector of frequency spectra of the track unevenness at all the wheel/rail interaction points associated to the i-th rail. Assuming completely symmetric problems, where the response of both rails is the same and the unevenness profiles of both rails are considered completely correlated, the wheel/rail interaction force vectors $\boldsymbol{F}_{r_1}^{w/r}$ and $\boldsymbol{F}_{r_2}^{w/r}$ are equal. Then, Eq. (4.26) can be written as

$$\boldsymbol{F}^{w/r} = \left(\mathbf{H}_v^{w/r} + \mathbf{H}_r^{w/r} + k_H^{-1}\mathbf{I}\right)^{-1} \boldsymbol{E}_r, \tag{4.27}$$

where the term $\mathbf{H}_r^{w/r}$ is equal to $\mathbf{H}_{r_1 r_1}^{w/r} + \mathbf{H}_{r_1 r_2}^{w/r}$ and can be obtained applying vertical unitary forces at both railheads on the a model of the track/tunnel/soil system based on the methodology presented in previous sections. Specifically, the elements of the receptance matrix $\mathbf{H}_r^{w/r}$ can be computed by

$$H_{r,nm}^{w/r} = \frac{1}{2\pi} \int_{-\infty}^{+\infty} \tilde{H}_r^r e^{-\mathrm{i}k_x(\tilde{x}_n - \tilde{x}_m)} \mathrm{d}k_x, \tag{4.28}$$

where $H_{r,nm}^{w/r}$ is the (n, m) element of the matrix $\mathbf{H}_r^{w/r}$, $\tilde{x}_n$ and $\tilde{x}_m$ are the longitudinal coordinates of the n-th and m-th axles, respectively, seen from the point of view of the moving frame of reference, and $\tilde{H}_r^r$ is the 2.5D Green's function of the vertical response of one of the rails (as the problem is completely symmetric, the response of both rails is the same) due to vertical forces applied at both rails. The 2D model of the vehicle that is used in this chapter is presented in B.1.

Once the wheel/rail interaction forces are computed, the displacement response in the time domain at any position of the railway infrastructure system due to the passage of the train can be found using the expression

$$u(\tilde{x}, t) = \frac{1}{4\pi^2} \int_{-\infty}^{+\infty} \sum_{n=1}^{N_a} \left[\int_{-\infty}^{+\infty} \tilde{H}_s^r F_n^{w/r} e^{-\mathrm{i}k_x(\tilde{x} - \tilde{x}_n)} \mathrm{d}k_x \right] e^{\mathrm{i}\tilde{\omega}t} \mathrm{d}\tilde{\omega}, \tag{4.29}$$

where $u(\tilde{x}, t)$ is the response in the time domain t in an arbitrary position of the railway infrastructure system, $\tilde{H}_s^r$ is the 2.5D Green's function in the wavenumber-frequency domain that relates the response of the system at that arbitrary position with a force applied at the rails, $\tilde{x}$ is the longitudinal coordinates associated to the moving frame of reference, $\tilde{x}_n$ is the longitudinal coordinatess of the n-th seen from the point of view of the moving frame of reference, v_t is the speed of the train, N_a is the number of train axles and $F_n^{w/r}$ is the wheel/rail interaction force associated to the n-th axle. An equivalent expression for the soil tractions can be obtained by simply replacing the displacement Green's functions with those for the tractions in Eq. (4.29). Similarly, the velocity and

acceleration responses can be obtained, respectively, using

$$v(\tilde{x}, t) = \frac{1}{4\pi^2} \int_{-\infty}^{+\infty} \sum_{n=1}^{N_a} \left[\int_{-\infty}^{+\infty} i(\tilde{\omega} + k_x v_t) \tilde{H}_s^r F_n^{w/r} e^{-ik_x(\tilde{x} - \tilde{x}_n)} dk_x \right] e^{i\tilde{\omega} t} d\tilde{\omega}, \qquad (4.30)$$

$$a(\tilde{x}, t) = \frac{1}{4\pi^2} \int_{-\infty}^{+\infty} \sum_{n=1}^{N_a} \left[\int_{-\infty}^{+\infty} -(\tilde{\omega} + k_x v_t)^2 \tilde{H}_s^r F_n^{w/r} e^{-ik_x(\tilde{x} - \tilde{x}_n)} dk_x \right] e^{i\tilde{\omega} t} d\tilde{\omega}. \qquad (4.31)$$

4.3.1 Wavenumber-frequency sampling strategy

The accuracy of the train pass-by response simulated in the basis of the present methodology is strongly dependent on how the Green's functions of the system are sampled in the wavenumber and frequency domain. In the present section, a sampling scheme is proposed in order to get a more accurate response of the system on account of the train pass-by. This sampling scheme proposes a linear sampling on moving frequencies and a non-uniform sampling scheme along the wavenumber that varies with the frequency. Note that, in this section, the frequency is seen from the fixed frame of reference ω is called static frequency and the frequency seen from the moving frame of reference $\tilde{\omega}$ is called moving frequency.

As a first step of the sampling strategy, the moving frequencies of the system are determined. This is accomplished in the following way:

- The required maximum static frequency $\omega_{\max}$ and the length of the sampling vector for frequency N_ω are defined.

- The maximum moving frequency $\tilde{\omega}_{\max}$ is computed using the relation $\tilde{\omega}_{\max} = \omega_{\max}(1 + v_t/c_{\min})$ [9], where v_t is the train speed and $c_{\min}$ is the minimum wave speed of the system. Theoretical wave speeds of ideal systems are used to obtain an approximation of $c_{\min}$ for the specific model studied.

- The sampling on moving frequency is then obtained by considering a linear distribution of N_w discrete values of the frequency from 0 to $\tilde{\omega}_{\max}$.

In the second step of the sampling strategy, the sampling on wavenumber k_x is determined. This is accomplished by the following steps:

- Initally, a pre-sampling process is perform, where the Green's functions of the system are obtained for two moving frequencies: $\pi/2$ rad/s and $\tilde{\omega}_{\max}$. Dense sampling vectors of $N_{k_x}^{ps}$ samples for the wavenumber are used for this two frequencies. These vectors are constructed by performing the following steps:

- Considering those two frequencies and the approximated wave speeds used in the $c_{\min}$ evaluation, a wavenumber limit for each of those two frequencies and for the i-th subsystem can be computed as $k_{xi}^{\lim} = \tilde{\omega}/c_i$, where c_i is the approximated wave speed of the i-th subsystem. The number of sub-systems existing in the model is N_{ss}.

- For each sub-system and each frequency, a wavenumber sampling vector of $N_{k_x}^{ps}/N_{ss}$ samples is constructed. Half of this samples are linearly distributed from $-2k_{xi}^{\lim}$ to $2k_{xi}^{\lim}$ (always considering the 0), and the rest are logarithmically distributed from $2k_{xi}^{\lim}$ to 10^5 rad/m and from $-2k_{xi}^{\lim}$ to -10^5 rad/m.

- Then, all sampling vectors associated to the same frequency are combined in only one pre-sampling vector of $N_{k_x}^{ps}$ samples.

- Finally, the two pre-sampling vectors obtained are used to compute the Green's functions of the system at both frequencies.

- The wavenumber limit until where most of the spectral content is confined is obtained for the each pre-sampling frequencies and each evaluator in the system. Then, for a specific evaluators, four wavenumber limits are computed: two with a tolerance of 10%, $k_{x_{\lin}}^{\lim_u}$ and $k_{x_{\lin}}^{\lim_d}$, and another one with a tolerance of 0.1% $k_{x_{\log}}^{\lim_u}$ and $k_{x_{\log}}^{\lim_d}$. Subscripts u and d are referred to the maximum and minimum frequencies used in the pre-sampling.

- The wavenumber limits $k_{x_{\lin}}^{\lim_u}$, $k_{x_{\lin}}^{\lim_d}$, $k_{x_{\log}}^{\lim_u}$ and $k_{x_{\log}}^{\lim_d}$ of only three evaluators are considered. These evaluators should be selected ensuring that they are representing high, medium and low wavenumber limits of all the evaluators of the system.

- It is assumed that the wavenumber limits $k_{x_{\lin}}^{\lim}$ and $k_{x_{\log}}^{\lim}$ vary linearly along the moving frequency and, therefore, they can be expressed as a function of $\tilde{\omega}$ as

$$k_{x_{\lin}}^{\lim}(\tilde{\omega}) = \left(\frac{\tilde{\omega} - \pi/2}{\tilde{\omega}_{\max} - \pi/2} \right) \left(k_{x_{\lin}}^{\lim_u} - k_{x_{\lin}}^{\lim_d} \right) + k_{x_{\lin}}^{\lim_u} \qquad (4.32)$$

and

$$k_{x_{\log}}^{\lim}(\tilde{\omega}) = \left(\frac{\tilde{\omega} - \pi/2}{\tilde{\omega}_{\max} - \pi/2} \right) \left(k_{x_{\log}}^{\lim_u} - k_{x_{\log}}^{\lim_d} \right) + k_{x_{\log}}^{\lim_u} \qquad (4.33)$$

- For each selected evaluator, a wavenumber sampling vector with a linear distribution of samples between $-k_{x_{\lin}}^{\lim}$ and $k_{x_{\lin}}^{\lim}$ (always considering the 0) and a logarithmic distribution from $k_{x_{\lin}}^{\lim}$ to $k_{x_{\log}}^{\lim}$ and from $-k_{x_{\lin}}^{\lim}$ to $-k_{x_{\log}}^{\lim}$ is constructed for each frequency. Half of the $N_{k_x}^s/3$ samples of this sampling vector (since N_{k_x} is the sampling vector length for the three evaluators combined) are used in the linear distribution and the other half in the logarithmic one.

- Finally, the non-uniform wavenumber sampling is obtained by combining the wavenumber samplings of the three selected evaluators.

4.4 Computation of vibration energy flow

The methodology described in previous sections define a method to simulate the response of the soil due to a train pass-by in the context of circular tunnels. Using this response, the vibration energy flow radiated upwards by the railway underground infrastructure under consideration can be computed. The vibration energy flow E can be computed from the power flow P as

$$E = \int_{-\infty}^{\infty} P(t) \mathrm{d}t, \tag{4.34}$$

where the power flow is defined as

$$P(t) = \int_S \boldsymbol{v}(\boldsymbol{x}, t) \cdot \boldsymbol{\tau}(\boldsymbol{x}, t) \mathrm{d}S, \tag{4.35}$$

being S the surface through where the energy flow wants to be evaluated and $\boldsymbol{v}(\boldsymbol{x}, t)$ and $\boldsymbol{\tau}(\boldsymbol{x}, t)$ are the vibration velocity and traction fields in the coordinate system $\boldsymbol{x}$.

Since the tunnel is assumed to be embedded in a full-space and, therefore, no wave reflections in the homogeneous full-space are expected, the only vibration energy that needs to be considered is the one radiated upwards. Thus, the vibration energy radiated upwards by a tunnel infrastructure is proposed to be computed by considering an integration surface that is a cylindrical strip of radius r_m, angular section defined by the angles θ_1 and θ_2 and width of one meter. Although the present modelling approach considers the system to be longitudinal invariant, the time domain response of the system due to a train pass-by is not. However, the response in the frequency domain is constant along the longitudinal direction. This allows considering only one sample of the vibration velocity and traction fields in the longitudinal direction in order to perform the integration along x. For the sake of simplicity, the response is evaluated at $x = 0$. Thus, the total energy per meter radiated across the surface is given by:

$$E = r_m \int_{\theta_1}^{\theta_2} \int_{-\infty}^{\infty} \boldsymbol{v}(0, \theta, t) \cdot \boldsymbol{\tau}(0, \theta, t) \mathrm{d}t \mathrm{d}\theta. \tag{4.36}$$

In order to use the previous expression, the velocity response in the soil is obtained using Eq. (4.30), while the traction response is obtained by using Eq. (4.29) by replacing the displacement Green's function in the soil with the traction Green's function.

4.5   Applications

In this section, the methodology described in the chapter is applied with the aim of comparing the vibration energy flow radiated by two different underground tunnel infrastructures. The underground railway infrastructures considered in this chapter are a simple tunnel with a single track where the rails are directly attached to the tunnel invert (direct fastening system) and a simple tunnel with a floating slab track. For the sake of simplicity, the first tunnel system is called DFF and the second FST. A schematic of the DFF and FST models developed in this case study are shown in Figs. 4.3 and 4.4, respectively. The mechanical properties of these system are summarised in Table 4.1, for the DFF, and in Table 4.2, for the FST. For both models, the rails and the fasteners are modelled as proposed in section 4.2.1 and the properties for these systems used in the present case study are shown in Table 4.3.
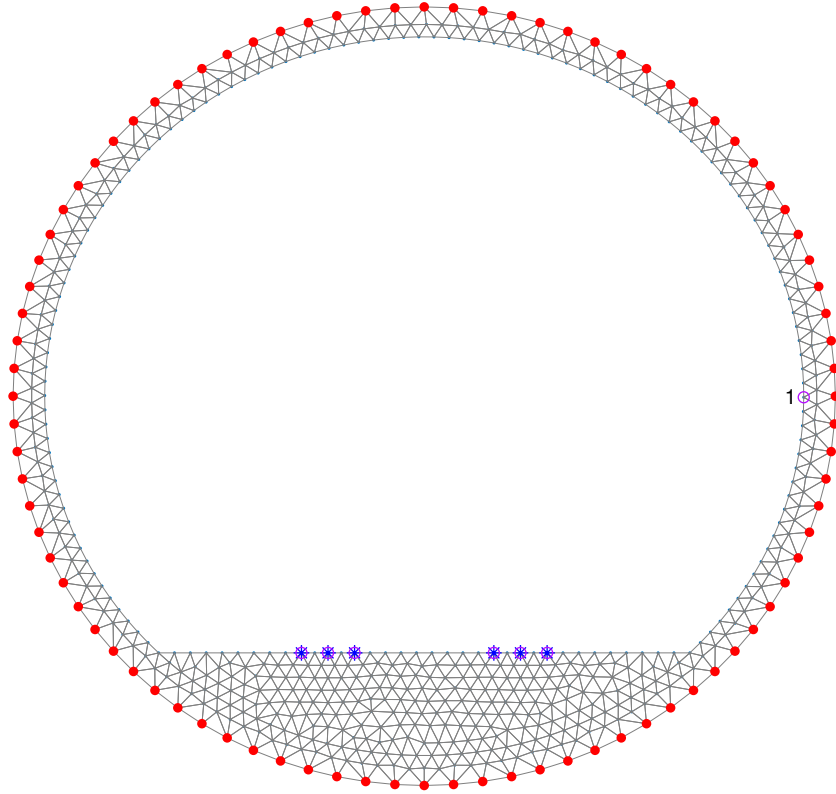
FIGURE 4.3: Schematic of the DFF system modelled by 2.5D FE (tunnel) and BE (soil). Red solid markers represent the BE nodes, blue star markers are the points where forces are applied and pink circular markers denote the evaluators, where the evaluator in the tunnel wall is denoted by 1.

The soil is modelled as a homogeneous full-space and tunnels are embedded in it. Both the tunnels have an inner radius of 3 m and a wall thickness of 0.25 m. The tunnels are excited by vertical points loads at the points shown in blue star markers. These points are the points where the rails are coupled to the tunnel/soil system. The Green's functions
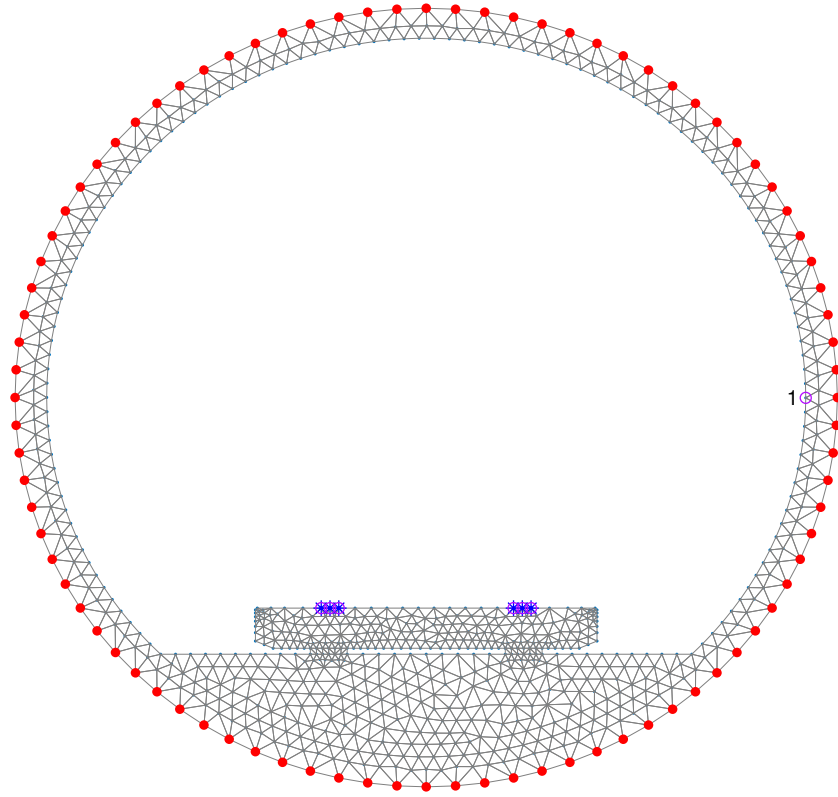
FIGURE 4.4: Schematic of the FST system modelled by 2.5D FE (floating slab track and tunnel) and BE (soil). Red solid markers represent the BE nodes, blue star markers are the points where forces are applied and pink circular markers denote the evaluators, where the evaluator in the tunnel wall is denoted by 1.

Subsystem	Parameters	Units	Value
Tunnel	Young's modulus	[GPa]	3.5
	Poisson ratio	[−]	0.15
	Density	[kg/m^3]	2500
	Damping	[−]	0.01

TABLE 4.1: Properties of DFF system.

of the track/tunnel/soil system for these point loads are obtained at the tunnel/soil interface (points shown in red) and evaluators locations (points shown in pink) using the track/tunnel/soil method previously presented. Then, the semi-analytical solutions of a cylindrical cavity in a full-space are used to relate the displacement Green's functions in the tunnel/soil interface with the displacement and traction Green's functions in a set of evaluators in the soil used later for energy flow computations. The properties of soil are summarised in the Table 4.4. The evaluators in the soil are located at radial distances of 5 m and 15 M from the outer wall of the tunnels (which represent radial distances of 8.25 m and 18.25 m from the centre of the tunnels, respectively) and placed at angular locations from $\theta = \pi/2$ rad to $\theta = \pi$ rad, and with 19 discrete points. Since the systems studied in this application study are symmetric, the vibration energy radiated upwards

Subsystem	Parameters	Units	Value
Tunnel	Young's modulus	[GPa]	3.5
	Poisson ratio	[−]	0.15
	Density	[kg/m^3]	2500
	Damping	[−]	0.01
Floating slab	Young's modulus	[GPa]	3.5
	Poisson ratio	[−]	0.15
	Density	[kg/m^3]	2500
	Damping	[−]	0.01
Elastomeric mat	Young's modulus	[MPa]	2.73
	Poisson ratio	[−]	0.35
	Density	[kg/m^3]	1328
	Damping	[−]	0.05

TABLE 4.2: Properties of FST.

Subsystem	Parameters	Units	Value
Rails	Density	[kg/m^3]	7850
	Young's modulus	[GPa]	207
	Cross-sectional area	[m^2]	$23.5 \cdot 10^{-6}$
	Second moment of inertia	[kg/m^2]	$6930 \cdot 10^{-6}$
Fasteners	Stiffness	[MN/m]	35
	Damping	[−]	$35 \cdot 10^3$

TABLE 4.3: Properties of the rails and fasteners used in DFF and FST.

can be computed multiplying by two the energy flow in the cylindrical strip defined $\theta_1 = \pi/2$ rad and $\theta_2 = \pi$ rad.

Parameters	Units	Value
Density	[kg/m^3]	2191
Young's modulus	[MPa]	180
Poisson ratio	[−]	0.3
Damping	[−]	0.025

TABLE 4.4: Properties of soil.

The sampling strategy mentioned in section 4.3.1 is followed to obtain the response of the system modelled with the numerical methodology. A total of 2^9 samples of $\tilde{\omega}$ and 2^{11} samples of k_x are considered for both infrastructures. Once the required Green's functions of the system are obtained, the train/track interaction and the train pass-by models described in section 4.3 are applied to obtain the response in the evaluator at the tunnel wall 1 and at the evaluators of the soil. The train is composed of 5 cars, while the properties of each car are summarised in Table D.1. The linearised Hertz contact stiffness is computed for the present case, obtaining a value of $1.23 \cdot 10^9$ N/m. It is assumed that rails have the same unevenness profile. The train speed in these

simulations is assumed to be 25 m/s, which is a common speed of operation of metro trains.

4.5.1   Vibration analysis

In this section, the analysis of the vibration response of both tunnel systems due to train passage is performed. The response of the rail and tunnel is obtained in the railhead (vertical response) and at evaluator 1 in the tunnel wall, respectively. Figure 4.5 shows the vibration acceleration response of the rails and evaluator 1 in the time domain for DFF and FST systems. Figure 4.6 shows the frequency content for the vertical component of the vibration acceleration of rail and evaluator on the tunnel wall in one-third octave bands for DFF and FST. The octave bands are normalised with respect to train pass time, which is computed as $(\tilde{x}_{N_a} - \tilde{x}_1)/v_t$.
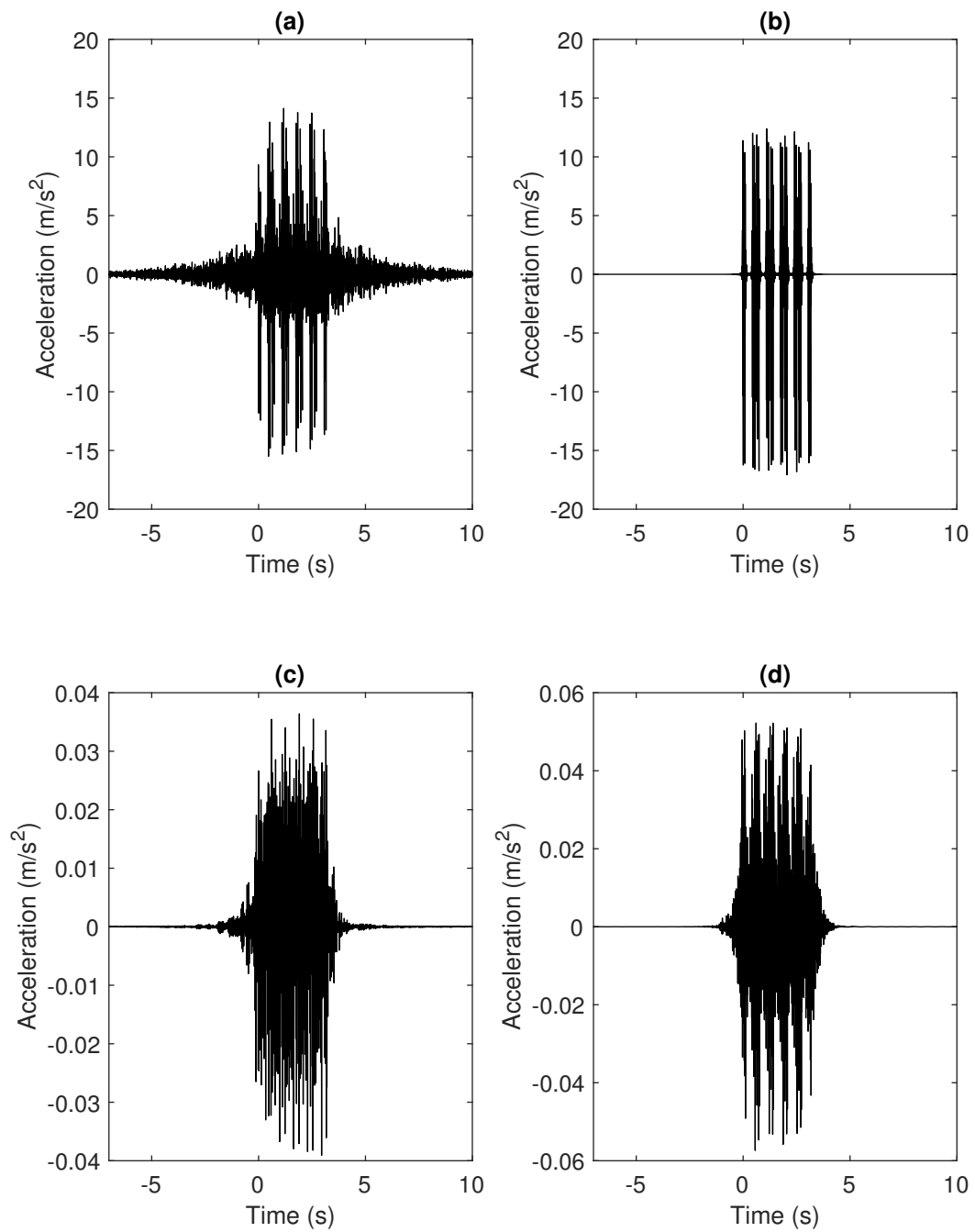
FIGURE 4.5: Acceleration response in the time domain of the rail for the FST (a) and
DFF (b) systems and on the evaluator 1 for the FST (c) and DFF (d) systems.
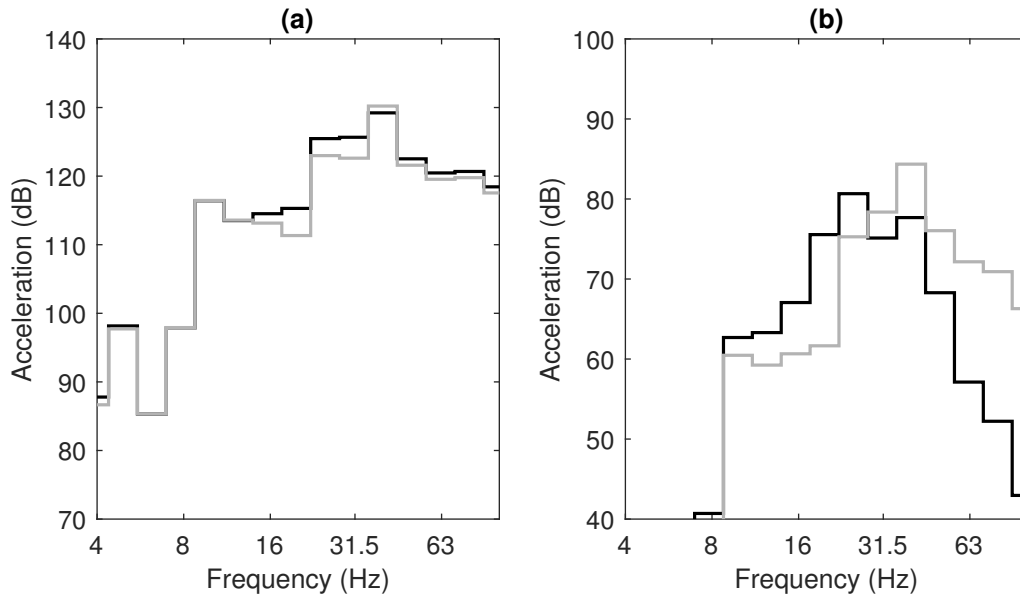
FIGURE 4.6: One-third octave bands of the vertical acceleration spectrum of the rail (a) and the evaluator 1 (b). The solid black line represents the response of the FST system and solid grey line represents the DFF system response. The reference for the dB is 10^{-6} m/s^2.

As shown in Fig. 4.6, it can be seen that, in general, the level of vibration of rail for the FST system is larger than the one for the DFF system, mostly for the bands of 20 Hz, 25 Hz and 31.5 Hz. In contrast, it is shown that the level of vibration on the evaluator 1 for the FST system is smaller and the frequency content is shifted to lower frequencies, inducing to large differences between the frequency responses of the FST and DFF systems at high frequencies, where the FST is reducing drastically the levels of vibration as compared with the DFF system.

4.5.2 Vibration energy flow analysis

In this section, a detailed analysis of the vibration energy flow radiated by both infrastructures considered in this application study is performed. For the vibration energy flow analysis, the total vibration energy flow, the mean power flow, the energy spectral density and the energy radiation pattern radiated by both infrastructures are obtained. The vibration energy flow analysis is performed on the evaluators in soil previous mentioned.

Using Eq. (4.36), the total energy flow per meter radiated by both DFF and FST tunnel systems at distances of 5 m and 15 m away from the outer tunnel wall is obtained. The results of this are shown in the Table 4.5. From the table it is observed that FST is radiating slightly more energy as compared to DFF at 15 m away from the outer wall

of the tunnel. As expected, the total vibration energy flow radiated upwards decreases with the radial distance of the soil evaluators due to the structural damping of the soil.

Track type	5 m	15 m
DFF	0.2547 J/m	0.1691 J/m
FST	0.2227 J/m	0.1711 J/m

TABLE 4.5: Total energy flow from DFF and FST

The mean power flow radiated through the defined cylindrical strip can be computed using the expression

$$P(t) = r_m \int_{\theta_1}^{\theta_2} \boldsymbol{v}(0, \theta, t) \cdot \boldsymbol{\tau}(0, \theta, t) \mathrm{d}\theta, \tag{4.37}$$

where this expression can be deduced from using Eq. (4.36).

In order to investigate which are the causes of the higher energy radiated by FST as compared with DFF system at 15 m away from the outer wall of the tunnel, the energy spectral density (ESD) per unit of longitudinal length is obtained. Equation (4.36) is used to obtain the ESD of all the evaluators located in the soil. Figure 4.7 shows the energy spectral density radiated by DFF and FST systems. In a similar way as the vibration analysis of the previous section pointed out, Figs. 4.7 and 4.8 show that the FST system is shifting the frequency content to lower frequencies. Moreover, in light of the total energy flow results previously obtained, one can deduced the this shift on frequency does not imply a change on the energy radiated, as the results at 5 meters, show. As the damping in the soil is affecting more the high frequency components of the vibration, the total energy loss between 5 m and 15 m for the DFF system is higher than the one for FST system at 15 m away from the outer wall of the tunnel.
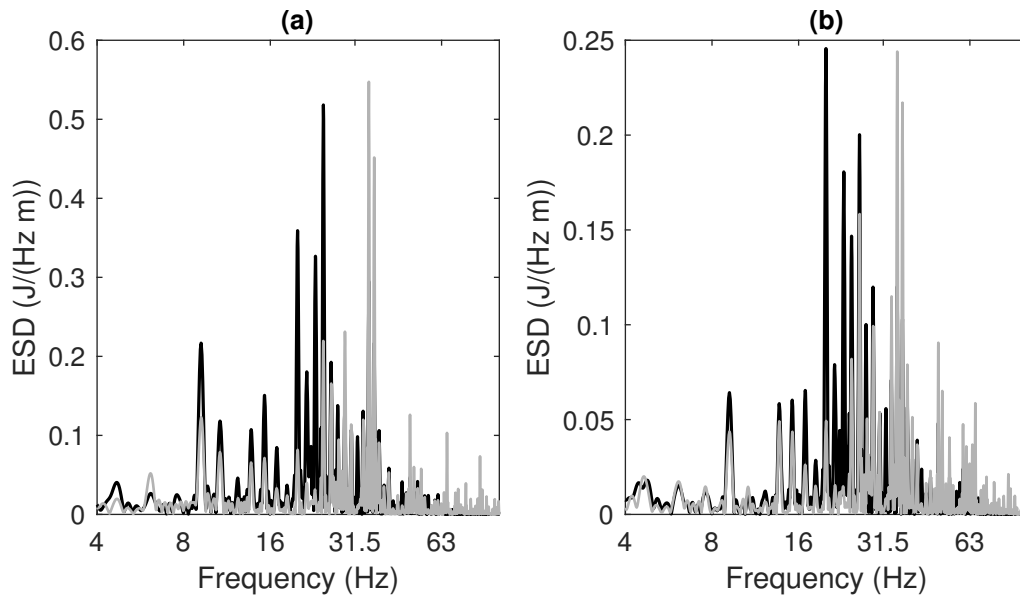
FIGURE 4.7: ESD of the vibration energy flow radiated upwards for the evaluators in soil located at a distance of 5 m (a) and at 15 m (b) from the outer tunnel wall for the cases of the DFF system (solid grey line) and FST system (solid black line).

FIGURE 4.8: Energy spectra (ES) in one-third octave bands bands of the vibration energy flow radiated upwards for the evaluators in soil located at a distance of 5 m (a) and at 15 m (b) from the outer tunnel wall for the cases of the DFF system (solid grey line) and FST system (solid black line). The dB are computed with a reference of 1 J/m.

Next, the radiation pattern of the vibration energy flow by both the infrastructures is studied. In order to study the radiation pattern of the vibration energy flow, the

radiated energy through the cylindrical strip has been computed as a function of θ

$$E(\theta) = r_m \int_{-\infty}^{\infty} \boldsymbol{v}(0, \theta, t) \cdot \boldsymbol{\tau}(0, \theta, t) \mathrm{d}t. \tag{4.38}$$

Figure 4.9 shows the radiation pattern of the vibration energy flow by both tunnel system. From Fig. 4.9 it can be observed that more vibration energy is radiated vertically upwards by DFF as compared to FST, especially closer to the tunnel.
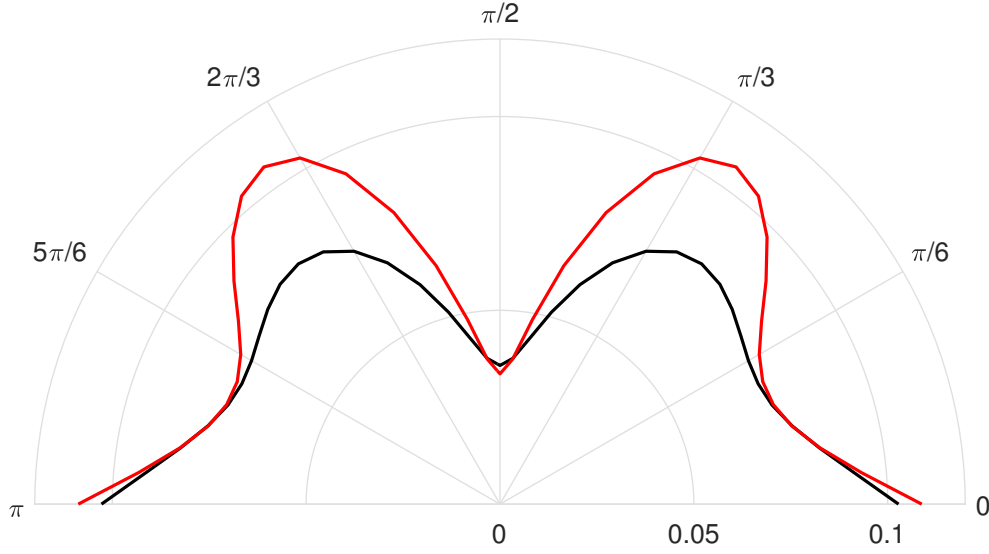
FIGURE 4.9: Radiation pattern of vibration energy flow radiated upwards (in (J/m)) at 5 meters as a function of θ (in (rad)) by DFF (solid red line) and FST (solid black line) systems.

Chapter 5

Validity of using only one accelerometer in the tunnel wall for railway-induced ground-borne vibration assessment of underground railway infrastructures

This chapter is intended to give insights into practical considerations in the use of one accelerometer for railway-induced ground-borne vibration assessment of underground railway infrastructures. The methodology developed in Chapter 4 is used in this regard. A preliminary assessment of the validity of using one accelerometer is presented. The chapter also contains an assessment and comparative study of the vibration generated and the energy flow radiated upwards by DFF and FST systems for two types of soils.

5.1   Study cases

In this section, the systems to be studied in this chapter are described. The underground railway infrastructures considered in this chapter are the same as presented in chapter 4: a simple tunnel with a single track where the rails are directly attached to the tunnel invert (direct fastening system) and a simple tunnel with a floating slab track. These systems are referred to as DFF and FST, respectively. In this chapter, the response is obtained at three evaluators in the tunnel wall. These evaluated are highlighted in pink and the identified as evaluators 1, 2 and 3, as shown in the figures. In this study,
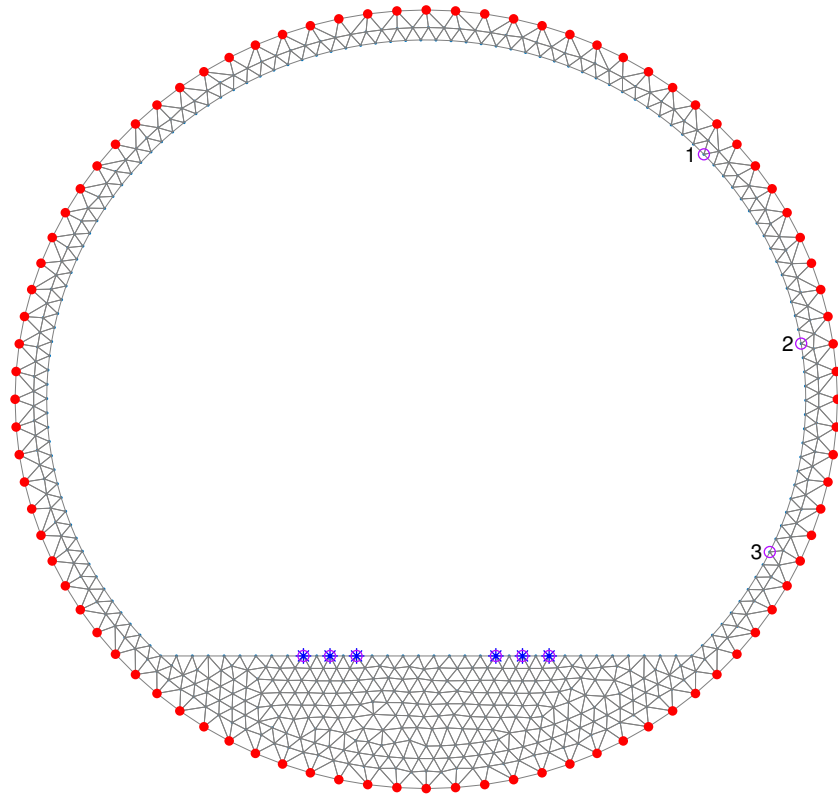
FIGURE 5.1: Schematic of the DFF system modelled by 2.5D FE (tunnel) and BE (soil). Red solid markers represent the BE nodes, blue star markers are the points where forces are applied and pink circular markers denote the evaluators, where the evaluator in the tunnel wall is denoted by 1, 2 and 3.
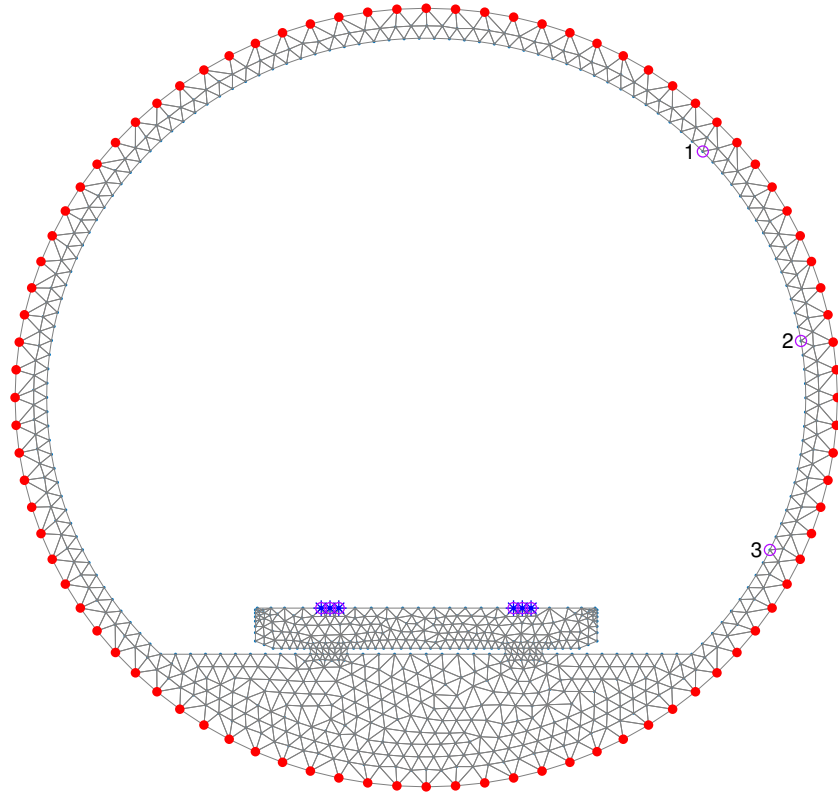
FIGURE 5.2: Schematic of the FST system modelled by 2.5D FE (floating slab track and tunnel) and BE (soil). Red solid markers represent the BE nodes, blue star markers are the points where forces are applied and pink circular markers denote the evaluators, where the evaluator in the tunnel wall is denoted by 1, 2 and 3.

two soil cases are considered: a soft soil and a hard soil. The properties of the soft soil used here are the same as considered in chapter 4 and are presented in Table 4.4, while the properties of the hard soil are presented in Table 5.1. The rest of the parameters used to perform the simulations in this chapter are the same than the ones presented in chapter 4.

Parameters	Units	Value
Density	[kg/m^3]	2191
Young's modulus	[MPa]	480
Damping	[−]	0.025
Poisson ratio	[−]	0.3

TABLE 5.1: Properties of hard soil.

5.2   Effect of soil stiffness on the tunnel wall response

In this section, the vibration response in the tunnel and the radiated energy flow in DFF and FST systems is performed for the two types of soil already defined: a soft soil and hard soil cases. The vibration response of the tunnel is obtained in terms of the radial acceleration of vibration in evaluator 2 for the two cases of soil stiffness. On one hand, Figure 5.3 shows the comparison of vibration acceleration spectra in one-third octave bands between DFF and FST systems, for soft soil (right) and hard soil (left) cases. In the other hand, Figure 5.4 shows the comparison of vibration acceleration spectra in one-third octave bands between soft and hard soil cases, for the DFF system (left) and the FST system (right). From Fig 5.3 and Fig. 5.4 it can be seen that the FST is able to reduce the high-frequency component of the vibration in the tunnel wall irrespective of soil stiffness. It is also shown that the soil stiffness has a significant effect on the level of vibration of the tunnel wall, being the vibration levels in the evaluator 2 in hard soil is less as compared to soft soil.
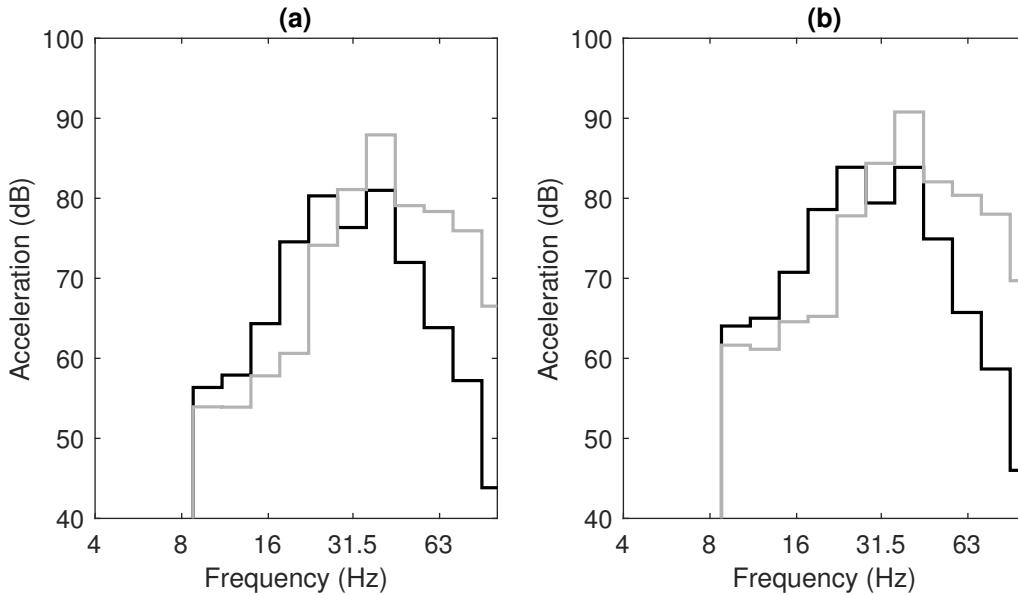
FIGURE 5.3: One-third octave bands of the radial acceleration spectrum of evaluator 2 hard soil (a) and soft soil (b) cases. Solid black lines represent the response in the case of the FST system and solid grey lines represent the DFF case. The reference for the dB is 10^{-6} m/s^2.
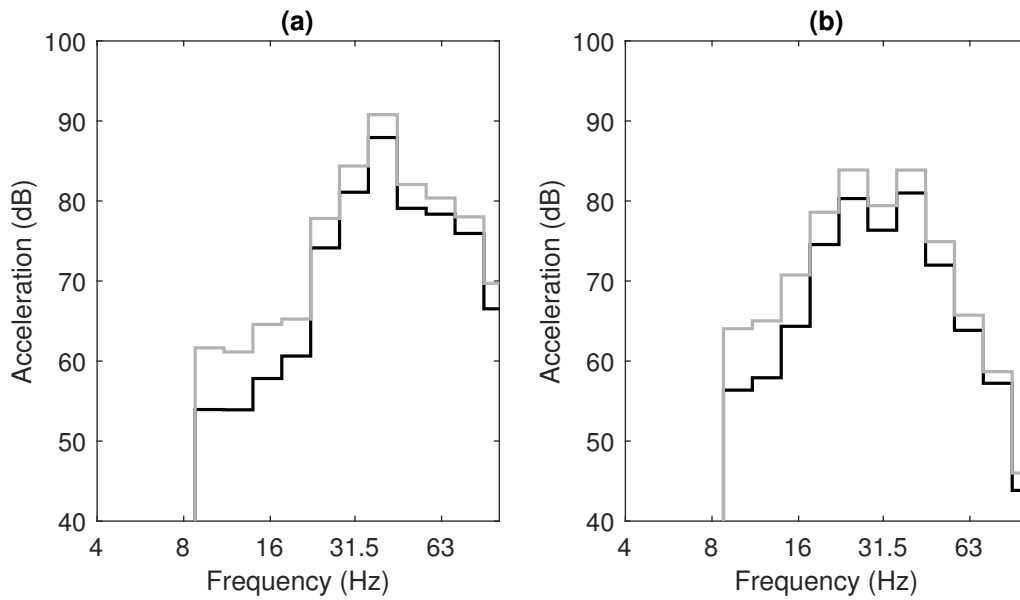
FIGURE 5.4: One-third octave bands of the radial acceleration spectrum of evaluator 2 for the case of the DFF system (a) and for the FST system (b). Solid black lines represent the hard soil case and solid grey lines represent the soft soil case. The reference for the dB is 10^{-6} m/s^2.

Moreover, and study of the vibration energy flow radiated upwards by both DFF and FST for the two types of soil studied is performed. All the computations are done considering the evaluators in the soil located at a distance of 5 m from the outer tunnel wall. Figures 5.5 and 5.6 shows the frequency response of the radiated vibration energy by DFF and FST systems for the soft soil and hard soil cases. In a similar way as the vibration analysis of the previous section pointed out, Figs. 5.5 and 5.6 show that the FST system is shifting the frequency content to lower frequencies. As expected, it can be said that the frequency content of the vibration energy flow changes significantly with the type of soil as seen in Fig. 5.6 (a) and Fig. 5.6 (b).
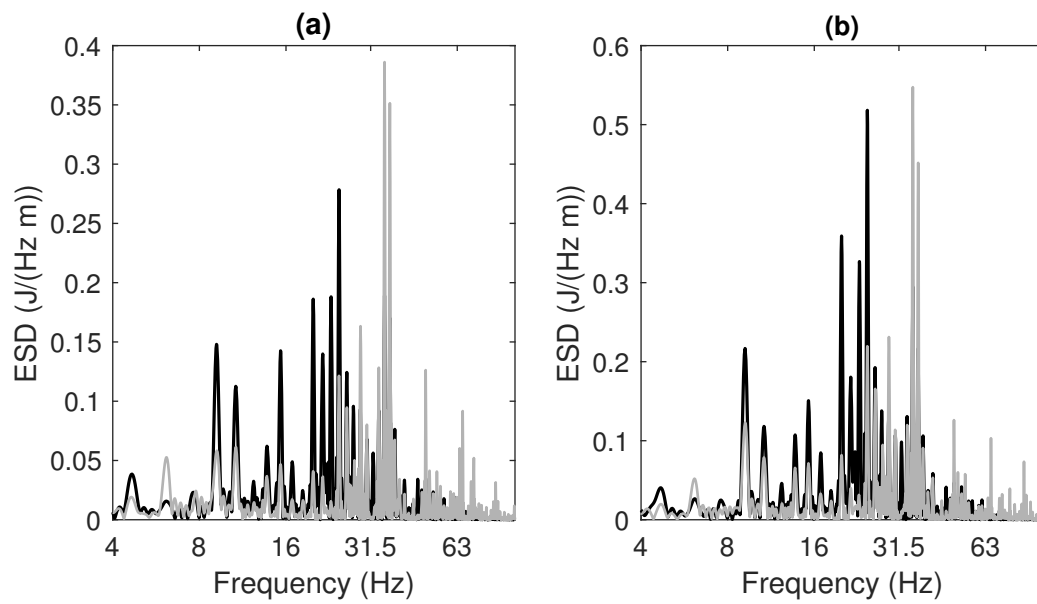
FIGURE 5.5: ESD of the vibration energy flow radiated upwards for hard soil (a) and in soft soil (b) cases and for the cases of the DFF system (solid grey line) and FST system (solid black line).
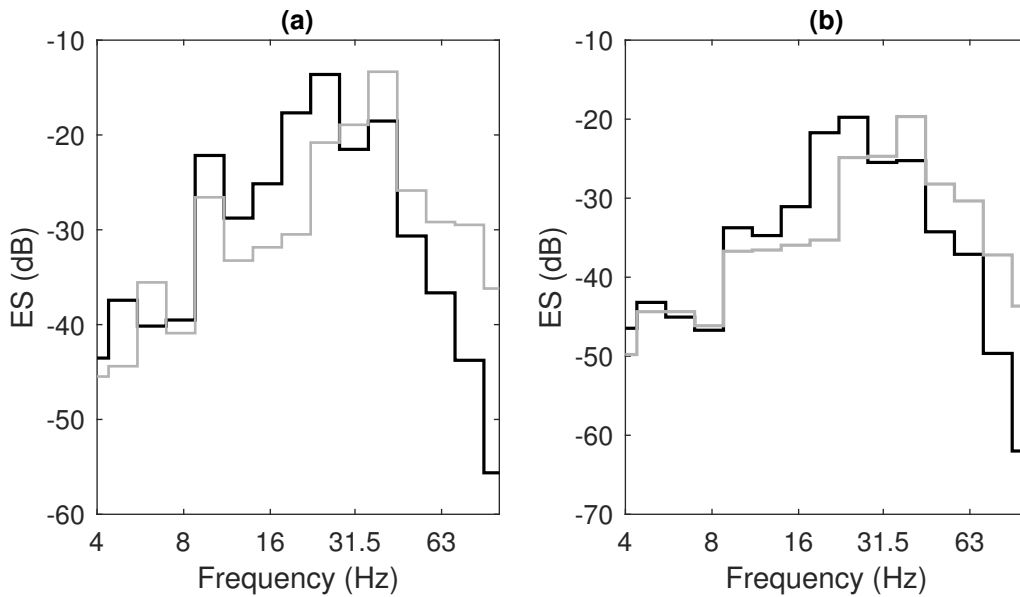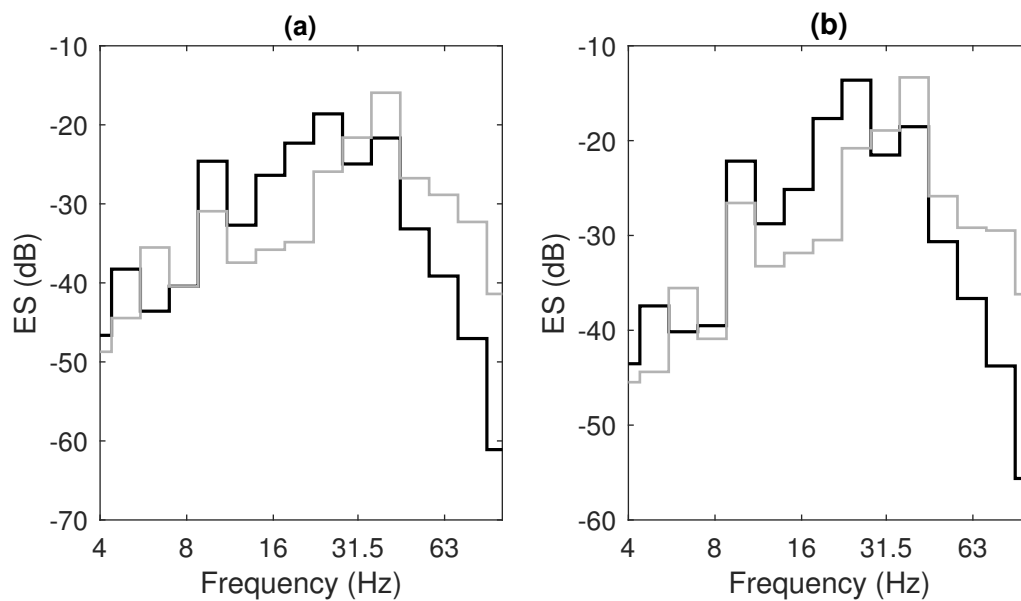

FIGURE 5.6: Energy spectra (ES) in one-third octave bands of the vibration energy flow radiated upwards for hard soil (a) and in soft soil (b) cases and for the cases of the DFF system (solid grey line) and FST system (solid black line). The reference for the dB is 1 J/m.

5.3 Validity of using one accelerometer in the tunnel wall for railway-induced ground-borne vibration assessment of underground railway infrastructures

In this section, the validity of using one accelerometer placed in the tunnel wall to assess the effectiveness of vibration mitigation countermeasures is studied. In order to study the validity of using one accelerometer, the insertion loss between the DFF and FST systems is taken as a reference. Two types of insertion loss are obtained: the one that comes from the comparison between the ESD associated with the vibration energy flow, which can be computed with the expression

$$\mathrm{IL}_{\mathrm{ESD}} = 10 \log_{10}\left(\frac{\mathrm{ESD}_{\mathrm{FST}}}{\mathrm{ESD}_{\mathrm{DFF}}}\right);\tag{5.1}$$

and the other associated to the acceleration in the y direction, which can be computed as

$$\mathrm{IL}_{\mathrm{a}} = 20 \log_{10}\left(\frac{a_{\mathrm{FST}}}{a_{\mathrm{DFF}}}\right).\tag{5.2}$$

In Eqs. (5.1) and (5.2), $\mathrm{ESD}_{\mathrm{FST}}$ represents the ESD associated to the FST system, $\mathrm{ESD}_{\mathrm{DFF}}$ represents the ESD related to the DFF system, a_{FST} represents the acceleration in y or z directions at the tunnel wall of the FST system while a_{DFF} represents the acceleration in y and z directions at the tunnel wall of the FST system. In the following, the insertion loss obtained by ESD $\mathrm{IL}_{\mathrm{ESD}}$ is compared with insertion loss obtained by the one obtained using the acceleration response IL_a at the three evaluators of the tunnel wall with the aim of obtaining insights in the use of one accelerometer for the assessment of the train pass-by overall induced vibration.

In Fig. 5.7 and 5.8, the insertion loss IL_{a} for y and z directions, respectively, and for all three evaluators on the tunnel wall is compared with the insertion loss $\mathrm{IL}_{\mathrm{ESD}}$ for the soft and hard soil cases. In these figures, it can be seen that IL_a approximately follows the $\mathrm{IL}_{\mathrm{ESD}}$ at frequencies between 10 and 50 Hz. For frequencies above 50 Hz, the IL_a associated to the three studied evaluators is overestimated with respect to $\mathrm{IL}_{\mathrm{ESD}}$. Moreover, a large difference between IL_a and $\mathrm{IL}_{\mathrm{ESD}}$ appears at 6.3 Hz for the case of hard soil. No feasible explanation of this phenomenon has been found yet.

In order to accurately determine the effectiveness of using one accelerometer for the assessment of underground railway-induced vibrations, the difference between $\mathrm{IL}_{\mathrm{ESD}}$ and IL_a is obtained and plotted in Fig. 5.9 for the case of the vibration of the evaluator in the y direction and in Fig. 5.10 for the case of the vibration of the evaluator in the a direction. As shown in the figures, the differences in insertion loss are very significant
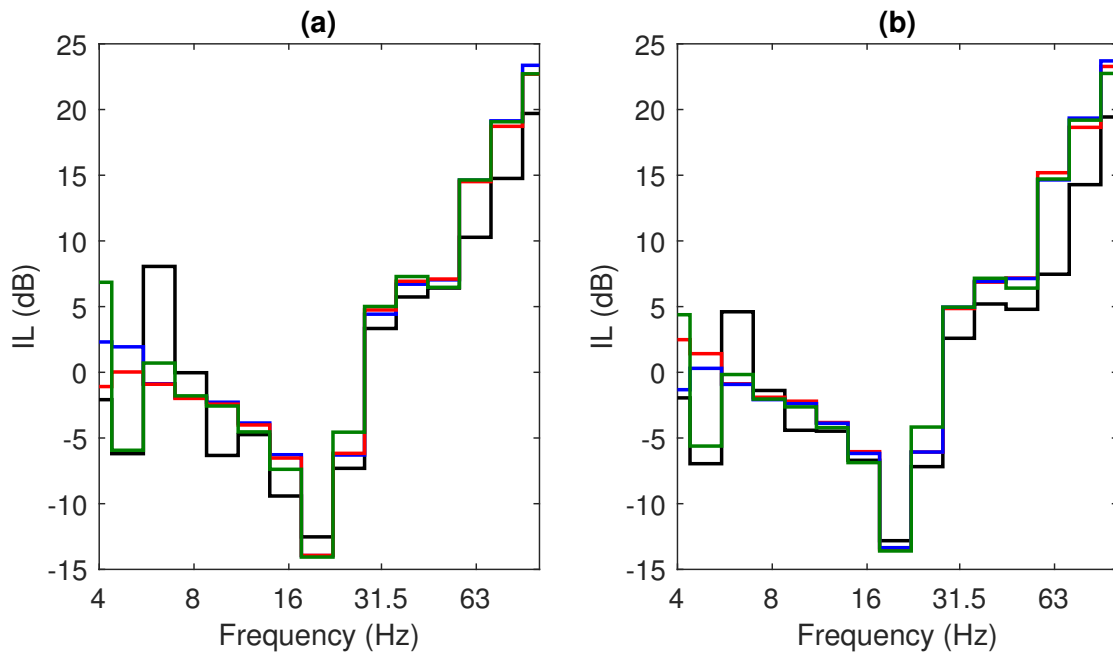
FIGURE 5.7: Insertion loss in dB for the evaluator 1 in y direction (solid blue line), the evaluator 2 in y direction (solid red line), the evaluator in y direction (solid green line) and for the vibration energy flow (solid black line) for hard soil (a) and soft soil (b) cases.
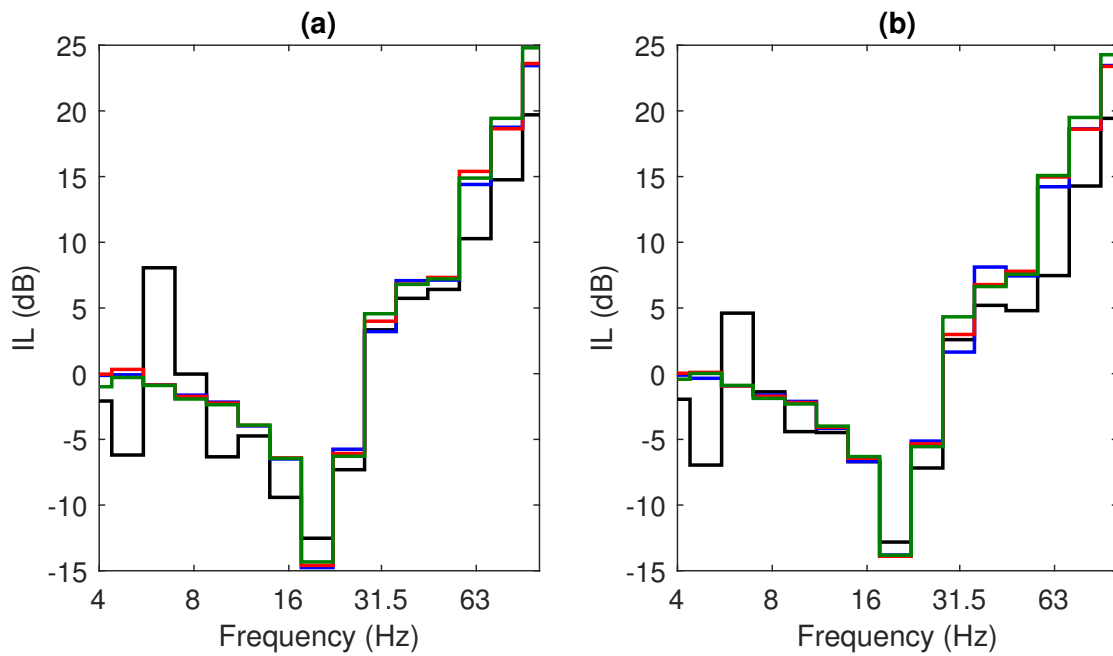
FIGURE 5.8: Insertion loss in dB for the evaluator 1 in z direction (solid blue line), the evaluator 2 in z direction (solid red line), the evaluator in z direction (solid green line) and for the vibration energy flow (solid black line) for hard soil (a) and soft soil (b) cases.

at 63 Hz for the case of the hard soil (arriving to values of 7 dB) and at 80 Hz and 100 Hz for the soft soil (also arriving to almost 8 dB).
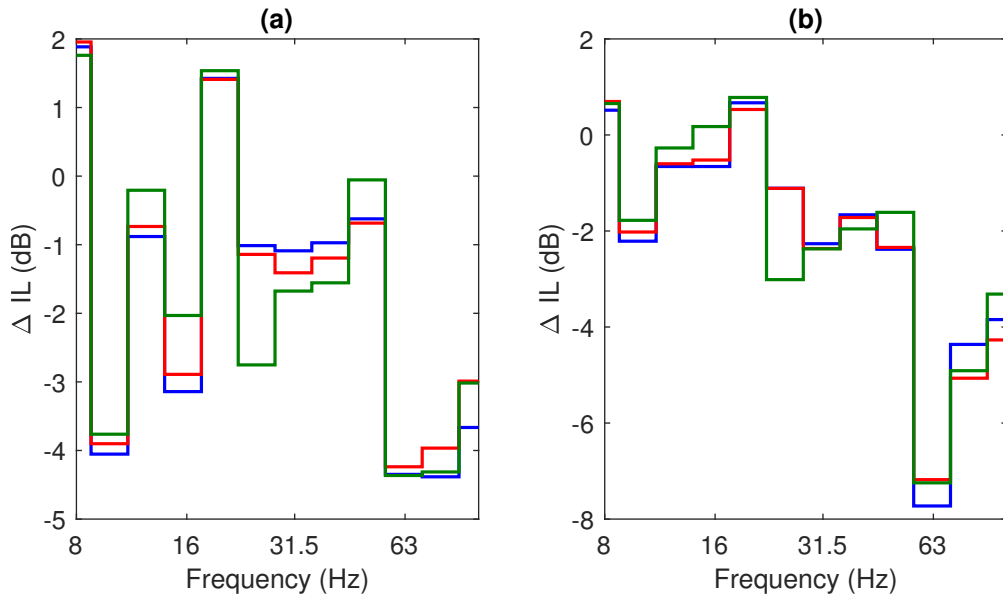
FIGURE 5.9: Difference between IL_{ESD} and IL_a for the evaluator 1 in y direction (solid blue line), for the evaluator 2 in y direction (solid red line) and the evaluator 3 in y direction (solid green line) and for hard soil (a) soft soil (b) cases.
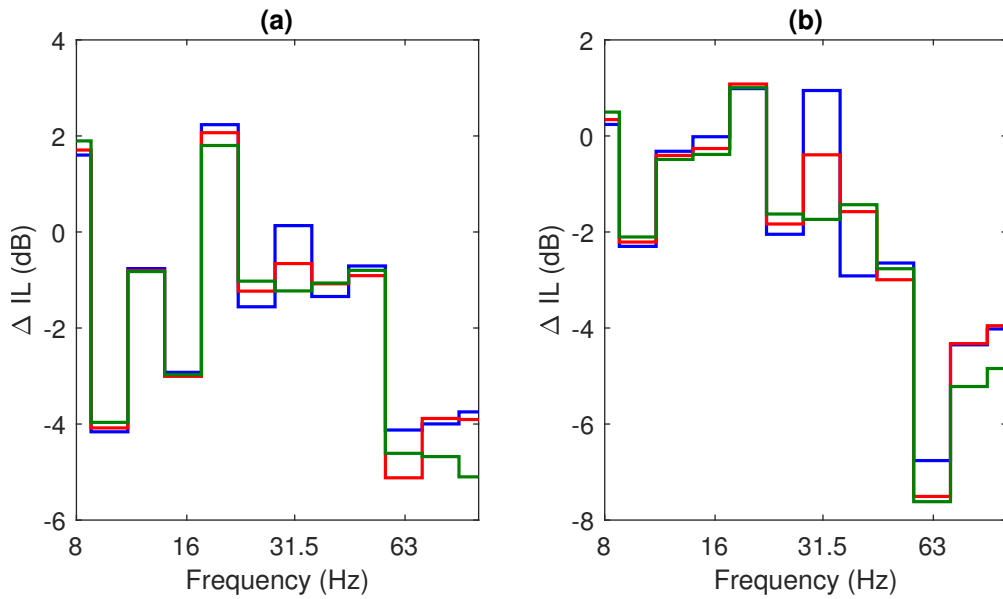
FIGURE 5.10: Difference between IL_{ESD} and IL_a for the evaluator 1 in z direction (solid blue line), for the evaluator 2 in z direction (solid red line) and the evaluator 3 in z direction (solid green line) and for hard soil (a) soft soil (b) cases.

The variability of the insertion loss at different points of the tunnel wall is studied by taking into account the three evaluators used in the calculation. To better understand this variability, the differences in IL_a between evaluator 2 and 3 with respect to evaluator 1 are plotted in Figs. 5.11 and 5.12, where Fig. 5.11 is related to the acceleration in the y direction and Fig. 5.12 to the z direction. These figures show that the differences between the selected evaluators are smaller than 2 dB. This implies that at least for the

evaluators selected, when an accelerometer is placed in the tunnel wall with the aim of assessing the vibration levels induced by a train passage in the particular tunnel studied, the decision of the point is not of great importance. This can be also clearly seen in Figs. 5.9 and 5.10, where it is shown that the differences between the $\mathrm{IL}_{\mathrm{ESD}}$ and IL_a are much larger than the differences between the insertion losses associated to the three evaluators. Figs. 5.11 and 5.12 also shown that the difference between the IL_a is slightly smaller in the hard soil case than in the soft soil case. Fig. 5.12 (a).
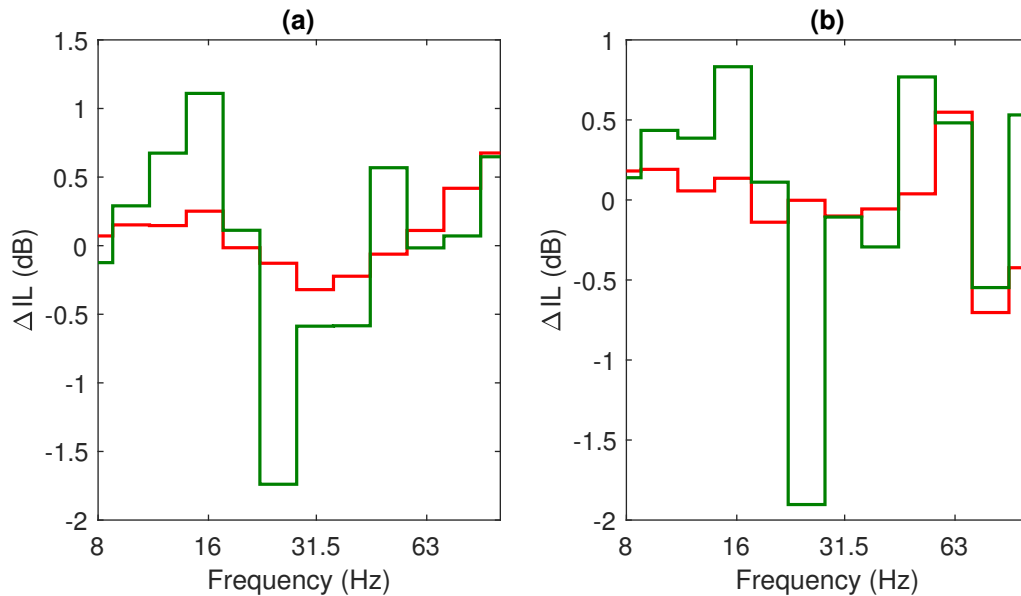
FIGURE 5.11: Difference between $\mathrm{IL}_{\mathrm{ESD}}$ and IL_a for the evaluator 2 (solid red line) and 3 (solid green line) with respect to evaluator 1 for hard soil (a) soft soil (b) cases. Results for the y direction.
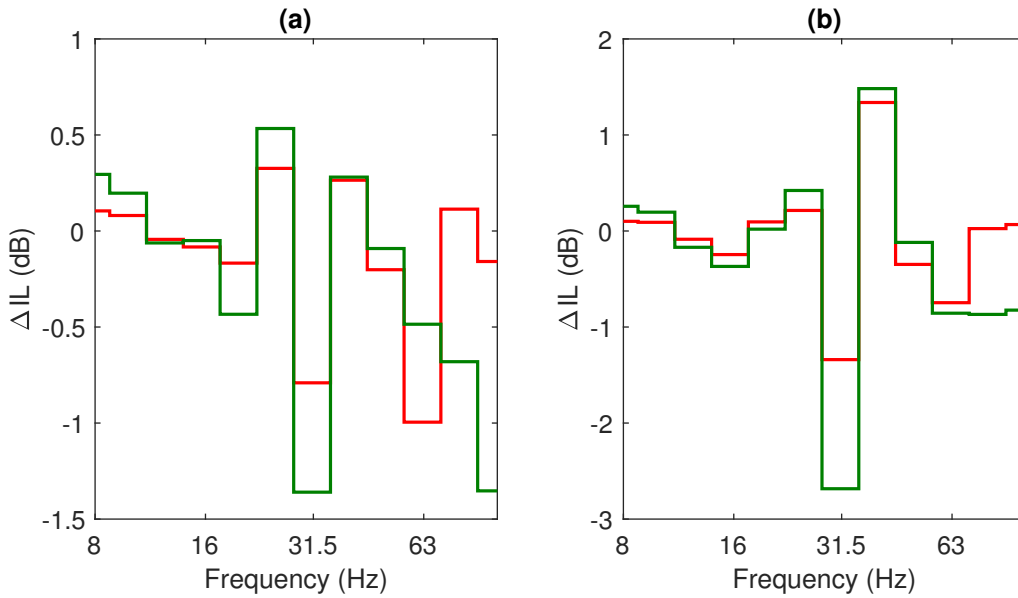
FIGURE 5.12: Difference between IL_{ESD} and IL_a for the evaluator 2 (solid red line) and 3 (solid green line) with respect to evaluator 1 for hard soil (a) soft soil (b) cases. Results for the z direction.

From the analysis of the insertion loss in Figs. 5.7 and 5.8, the difference in insertion loss between ESD and acceleration in Figs. 5.9 and 5.10 and relative difference of insertion loss Fig. 5.11 and 5.12, three important conclusions are found:

- It is found that the differences between the insertion loss that comes from the vibration energy flow with respect to the insertion loss coming from one accelerometer in the tunnel wall are up to 8 dB at frequencies of 63 Hz, 80 Hz and 100 Hz. Then, using one accelerometer in the tunnel wall in order to assess the efficiency of a vibration mitigation countermeasure applied in a railway tunnel overestimates its IL. On the other hand.

- The variations in the IL associated with the vibration acceleration are found to be small, implying that the location of the accelerometer is not of great importance.

- It is found that the IL of a mitigation measure could be significantly dependent on the local subsoil surrounding the tunnel infrastructure.

In this study, the variability of parameters such as train speed, soil stiffness, fasteners stiffness, track type and type of tunnel infrastructure is small. In order to achieve more rigorous conclusions about the validity of using one accelerometer in the tunnel for the assessment ground-borne railway-induced vibration in tunnels, more studies need to be carried out accounting for a much more representative set of parameters of the system.

Chapter 6

Methodology for the computation of the re-radiated noise inside tunnels

This chapter focuses on the analysis of noise and vibration generated in underground railway tunnels due to train traffic. Specifically, an analysis of noise and vibration generated by train passage in an underground simple tunnel in a homogeneous full-space is presented. In this chapter, a methodology based on decoupled 2.5D elastodynamic FEM-BEM along with 2.5D acoustic BEM is presented to model the re-radiated noise generated inside the tunnels due to train passage. The 2.5D FEM BEM used to model soil-structure interaction problems. The noise analysis inside the tunnel is performed using a 2.5D acoustic BEM considering a weak coupling. The method of fundamental solutions (MFS) is used to validate the acoustic BEM methodology. The influence of fastener stiffness on vibration and noise characteristic inside a simple tunnel is investigated.

6.1 Numerical methodology

A global computational scheme has been developed to study the re-radiated noise radiated on account of train-pass. A schematic of this computational scheme is shown in Fig. 6.1. It consists of three different models: the train/track interaction, the elastodynamic model that represents the track/tunnel/soil system and the model for the interior acoustics. As shown in the scheme, the coupled train/track/tunnel/soil system is solved in the two initial steps. In the first one, the track response, obtained from the 2.5D elastodynamic FEM-BEM model, and the vehicle response are used to obtain the wheel/rail interaction forces. In the second step, these forces are applied to the 2.5D elastodynamic FEM-BEM model of the track/tunnel/soil system to obtain the structural response. Then, the re-radiated noise generated by this structural response is computed by means a 2.5D acoustic BEM.
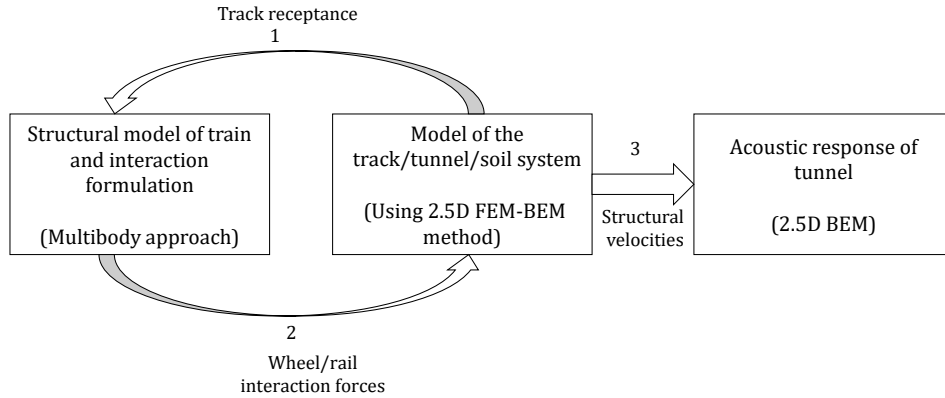
FIGURE 6.1: Schematic description of the methodology for computing re-radiated noise.

6.2 Acoustic analysis

The presented methodology utilising MFS and BEM for analysis of acoustics space in conjunction with 2.5D FEM-BEM method for analysis of elastodynamics is called decoupled approach, as it treats each domain separately and only the compatibility between both the domains is respected. This compatibility is guaranteed by prescribing the field of normal velocities obtained from the elastodynamic problem to the boundary of the acoustic domain. Since a decoupled approach is followed, the results computed in terms of structural velocity are used boundary conditions for computation of pressure levels in the acoustic domain. The acoustic pressure levels are computed by means of acoustics BEM and MFS. The collocation points for MFS are chosen to be the nodal points of FEM-BEM element mesh which bounds the acoustic domain and are also the nodes of BEM mesh used for obtaining the solution using BEM. The normal velocity $\bar{V}_n$ used as a boundary condition on the collocation points are computed from the normal displacement $\bar{U}_n$ obtained from the dynamic response of the structure as:

$$\bar{V}_n = \mathrm{i}\omega\bar{U}_n, \tag{6.1}$$

The procedure for obtaining the sound pressure levels using MFS and BEM is described in the succeeding sub-subsections. In both methodologies, the hysteretic damping model for the air is considered.

6.2.1 2.5D interior acoustics BEM approach

The pressure field in the acoustic space is obtained in a two-step procedure by BEM. In the first step unknown pressures on the boundary are obtained by using the known normal velocities on the boundary. From the pressure and velocities known on the boundary the pressure in the evaluation points are subsequently obtained. The velocity obtained from Eq. 6.1 is used as a boundary condition to obtain the pressure on the boundary of acoustic domain. The BEM used in acoustics also uses globally regularised integrals and there by avoids explicit computation of singular terms. The 2.5D regularised boundary integral equation for acoustics is obtained by following the standard regularisation procedure outlined in [79] on the integral representation equation Eq. (B5) of [66]. As a result, the regularised boundary integral equation in 2.5D is given by:

$$\int_S \left[\bar{p}(\mathbf{y})\bar{H}(\mathbf{x},\mathbf{y}) - \bar{p}(\mathbf{x})\bar{H}_0(\mathbf{x},\mathbf{y}) \right] \mathrm{d}S = \mathrm{i}\rho\omega \int_S \bar{v}(\mathbf{y})\bar{G}(\mathbf{x},\mathbf{y})\mathrm{d}S, \tag{6.2}$$

where the boundary integral equation is defined over an bounded domain defined by boundary S, $\mathbf{x}$ is the vector of coordinates of the source point, $\mathbf{y}$ is the vector of coordinates of the receiver locations, $\bar{H}$ is the Green's functions associated to the velocity in wavenumber frequency domain, $\bar{H}_0$ is the static Green's functions associated to the velocity ($\omega = 0, k_x = 0$) and $\bar{G}$ is the matrix of Green's functions associated to the pressure, $\bar{p}$ is the pressure and $\bar{v}$ is the velocity and ρ is the density of medium. Thus, the boundary integral equation used for obtaining the pressure on the boundary nodes, in matrix form is given by

$$\bar{\mathbf{H}}_b \bar{\boldsymbol{P}}_{n_b} = \mathrm{i}\rho\omega \bar{\mathbf{G}}_b \bar{\boldsymbol{V}}_{n_b}, \tag{6.3}$$

where, $\bar{\mathbf{H}}_b$, $\bar{\mathbf{G}}_b$ are matrices related to Green's velocity and pressure computed on boundary, $\bar{\boldsymbol{P}}_{n_b}$ and $\bar{\boldsymbol{V}}_{n_b}$ are nodal pressures and velocities on the boundary, respectively. After obtaining the boundary unknowns the pressure in the acoustic space is obtained as:

$$\bar{\boldsymbol{P}}_{n_f} = -(\bar{\mathbf{H}}_f \bar{\boldsymbol{P}}_{n_b} + \mathrm{i}\rho\omega \bar{\mathbf{G}}_f \bar{\boldsymbol{V}}_{n_b}), \tag{6.4}$$

where, $\bar{\boldsymbol{P}}_{n_f}$ is the vector of pressure in the acoustic space, $\bar{\mathbf{H}}_f$, $\bar{\mathbf{G}}_f$ are matrices related to Green's velocities and pressures computed in on evaluation points in acoustic space. The derivation of the above equation can be found in [79, 66]. The Green's functions of velocity and pressure are given in Appendix B.1 The speed of computation of BEM is improved by using the computation scheme similar to the one mentioned in Sec 3.2.1.

6.2.2   2.5D MFS approach applied to interior acoustics

The MFS approximates the pressure field within a given domain with a linear combination of fundamental solutions (Green's functions) of the governing differential i.e. the Helmholtz equation. The acoustic response at a generic point x is then reproduced considering the effects of N_S virtual sources located outside the analysis domain, as expressed by

$$\bar{P}(x) = \sum_{m=1}^{N_S} A_m \bar{G}_{mfs}(x, x_0^m), \qquad (6.5)$$

where, $\bar{G}_{mfs}(x, x_0^m)$ is the to the Green's function of the sound pressure, x_0^m represents the coordinates of the virtual source m and $(m = 1, 2, \cdots, NS)$, A_m is the unknown amplitudes of the virtual sources. In order to obtain the unknown amplitudes of the sources continuity of normal velocity at the collocation points is imposed i.e.

$$\sum_{m=1}^{N_S} A_m \bar{H}_{mfs}(x_p^i, x_0^m) = \bar{V}_n, \qquad (6.6)$$

where, $\bar{H}_{mfs}(x_p^i, x_0^m)$ is Green's functions for particle velocity and x_p^i are the coordinates of the collocation point i and $i = (1, 2, \cdots, n)$. The 2.5D Green's functions to be used in this 2.5D MFS approach are the same that the ones employed in the 2.5D acoustic BEM, which are shown in Appendix B.1 The validation of this MFS methodology together with more details regarding the method can be found in [65, 80].

6.2.3   Verification of the 2.5D acoustic BEM

At first, the proposed 2.5D acoustic BEM is verified by comparing with the analytical solution of the pressure response due to a 2.5D pulsating cylinder. This analytical solution is given in Appendix B.1 For the comparison, it is considered a cylinder of unit radius and an evaluation point located 10 m away from the centre of the cylinder. A 0.01 damping is considered for the air. BEM meshes of 60 and 180 elements are used for the comparison. Figure 6.2 shows the comparison of this response for a frequency range of $0 - 250$ Hz and for $k_x = (0, 0.5, 1)$ rad/m. As shown in the figure, a good agreement between the response of the 2.5D BEM and the analytical solution is found. Moreover, it is shown that the slight errors associated with the mesh of 60 elements can be avoided increasing the mesh density.

Next, the proposed 2.5D acoustic BEM method for interior acoustics is verified using the 2.5D MFS approach presented in Sec. 6.2.2. The verification is accomplished by comparing the pressure field inside a rectangular tube subjected to external excitation.
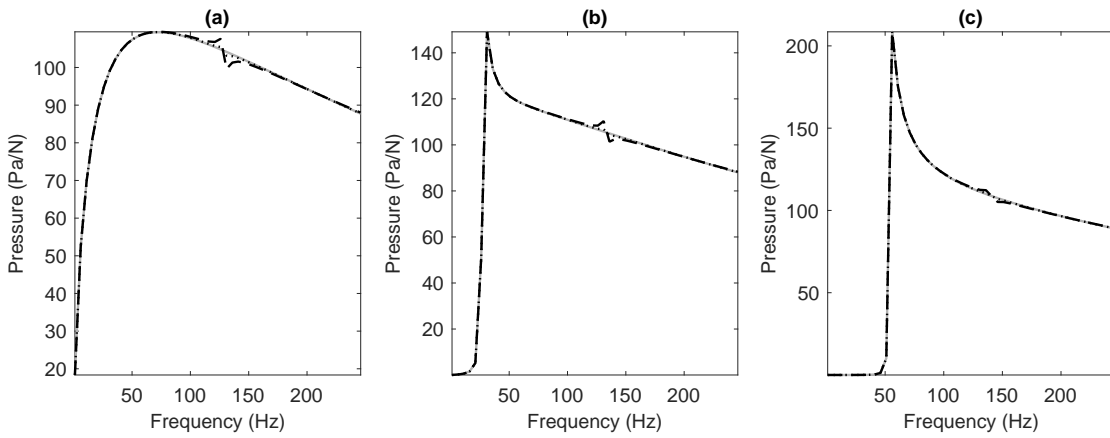
FIGURE 6.2: Pressure response obtained at a point located at a radial distance of 10 m for $k_x = 0$ rad/m (a), $k_x = 0.5$ rad/m (b) and $k_x = 1$ rad/m (c). The cases considered are: 2.5D acoustic BEM with 60 elements (dashed line), 2.5D acoustic BEM with 180 elements (dotted line) and analytical solution (solid grey line).
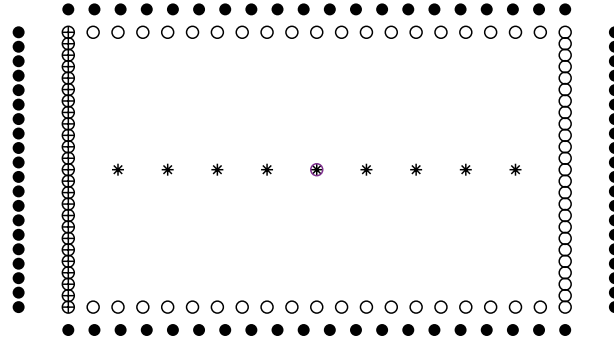
FIGURE 6.3: Rectangular tube used for the verification of the 2.5D acoustic BEM considering an 88-element mesh. The collocation points are represented by hollow markers, the source points by solid markers, the evaluators by star markers and the loaded collocation points by plus markers.

Figure 6.3 shows the schematic of the rectangular tube used for this verification. For $k_x = 0$, the pressure response inside the tube due to external excitation has an analytical solution. This analytical solution is also given in Appendix B.1. A velocity boundary condition is assumed at points shown by plus markers in Fig. 6.3 of the tube. A damping factor of 0.01 is considered for the air. BEM meshes of 88 elements and 220 elements are used for comparison. The pressure field is obtained at the points located at the star markers in Fig. 6.3. For this case, the collocation points in MFS are the nodes of the BEM mesh of 88 2-node elements.

Figure 6.4 shows the pressure obtained by MFS, BEM and analytical solution (in this case, only for $k_x = 0$) at the evaluator shown by circle star marker in Fig. 6.3. The results at the rest of the evaluators also present a good match between the methods. The figure shows good agreement between the methods. Also, it is shown that the slight errors associated with the mesh 88 elements can be avoided increasing the mesh density.
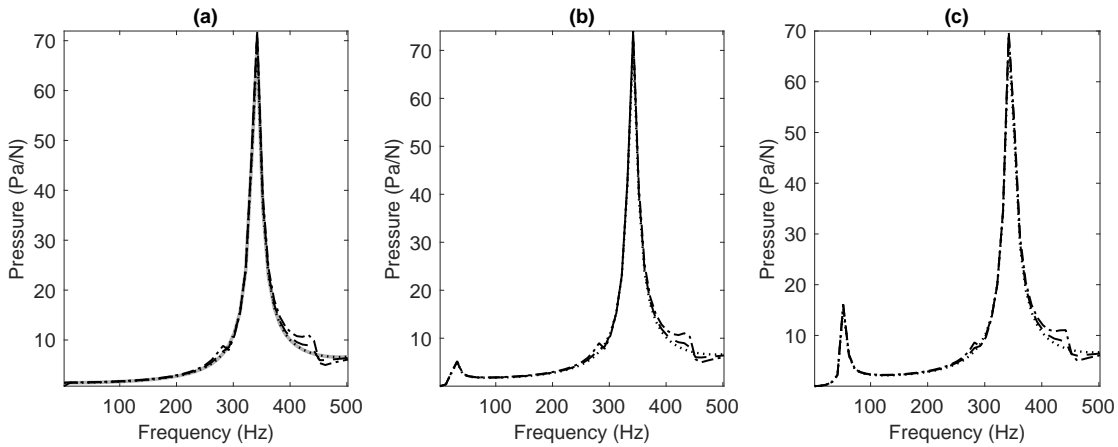
FIGURE 6.4: Pressure response computed in the wavenumber-frequency domain at the evaluator located at the centre of the tube. Sub-figure (a) shows the comparison of MFS (dotted line), BEM (dash-dotted line for the 88-element mesh and dashed line for the 220-element one) and analytical solution (solid grey line) for $k_x = 0$; Sub-figures (b) and (c) show a comparison of MFS and BEM for $k_x = 0.5$ rad/m and $k_x = 1$ rad/m, respectively.

6.3   Application

The present methodology is applied in the investigation of the re-radiated noise generated by train traffic inside underground tunnels. Although this methodology can be used for a wide range of studies related to noise and vibration analysis associated to railway infrastructures, this methodology is applied in the context of the present chapter to study the effects on the re-radiated noise in already constructed tunnels due to vibration abatement solutions. The coupled 2.5D elastodynamic FEM-BEM defined in Sec. 3.1 is used for computing the track and the tunnel structure response. The acoustic analysis inside the tunnel is performed using the 2.5D acoustic BEM defined in Sec. 6.2.1. Accounting for that substituting the rail pads of the fasteners by softer ones is one of the most common vibration abatement solutions applied to the existing railway track, a study of the effect that the fasteners stiffness has on noise radiation deserve consideration and it is also presented in this chapter. For this study, two cases of fasteners with different stiffness properties and a case where rails are directly fastened to the tunnel floor are analysed.

The model of the underground tunnel is shown in Fig. 6.5. The structure, consisting of the tunnel, the fasteners and the rails, is modelled with linear triangular finite elements, while the soil is modelled using the 2.5D elastodynamic BEM, being its associated nodes shown in red. The boundary element is a linear element having two nodes per element.

A nodal collocation scheme is followed to obtain the BEM matrices. Assuming a weak coupling between elastodynamic and acoustics systems, the structural response obtained at the purple points is used as the input to the acoustic model in terms of structural velocities. The tunnel has an inner radius of 3 m and a thickness of 0.25 m. The mechanical parameters of the rails, tunnel and soil as isotropic elastic media are presented in Table 6.1. The rail fasteners that attach the rails to the tunnel invert consist of a top elastomer just below the rails and a bottom elastomer sandwiched between two metallic plates under the top elastomer. Thus, the fasteners are modelled as a sandwiched system consisting of four layers meshed with 2.5D finite elements. The equivalent properties to be used in the 2.5D FEM model of the fasteners for the two cases previously mentioned are presented in Tables 6.2 and 6.3. These equivalent properties are obtained by considering that the vertical stiffness of the rails fastening system should not be modified when a continuously distributed fasteners are assumed instead of the typical periodic distribution of them. The thicknesses of the top and bottom elastomers are considered to be 0.007 m and 0.012 m, respectively, and those of the metallic plates are 0.016 m and 0.012 m, respectively for the top and the bottom. On Fig. 6.5, evaluators A, B and C are considered to show the vibration response of the structure, while evaluators a, b and c are used to present the noise response in following sections.

	E [MPa]	ρ [kg/m^3]	ν	D_p	D_s
Rails	207	7850	0.15	0.01	0.01
Tunnel	35	2500	0.15	0.01	0.01
Soil	0.18	2191	0.3	0.025	0.015

TABLE 6.1: Parameters of superstructure

	E [MPa]	ρ [kg/m^3]	ν	$D_p = D_s$
Top elastomer	1.15	1329	0.45	0.05
Top plate	$207 \cdot 10^3$	7850	0.30	0.01
Bot. elastomer	2.7	1329	0.35	0.05
Bottom plate	$207 \cdot 10^3$	7850	0.30	0.01

TABLE 6.2: Fasteners properties for case 1.
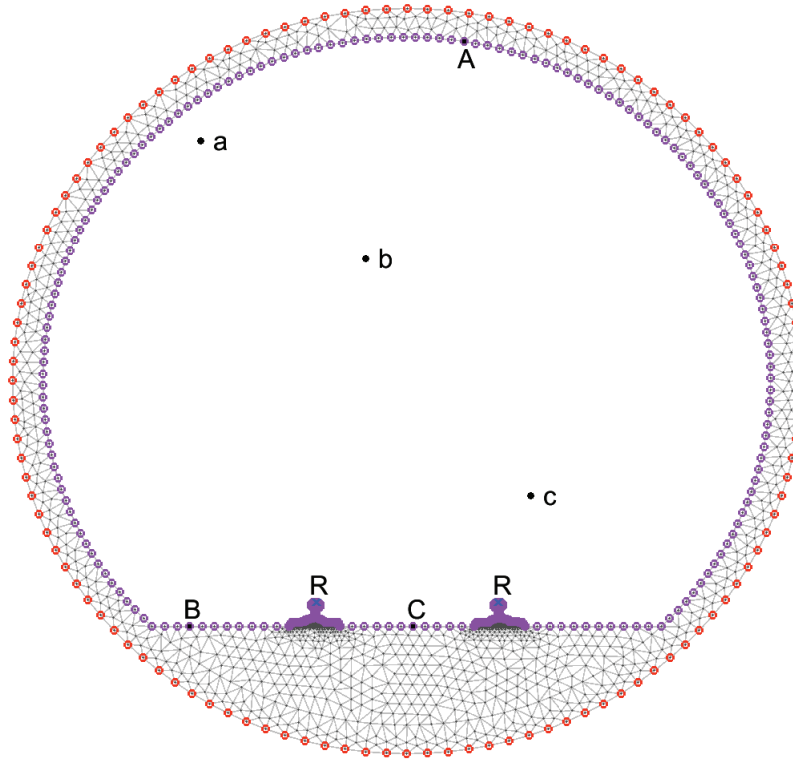
FIGURE 6.5: Geometry of the simple tunnel studied in this article. Considering the centre of the tunnel inner circumference at $(y = 0, z = 0)$, vibration response evaluators A, B and C are located at $(y = 0.5, z = -2.96)$ m, $(y = -1.79, z = 2.14)$ m and $(y = 0.05, z = 2.14)$ m, respectively; the rail response is obtained at the evaluators R, placed on top of each of the rails; acoustic response evaluators a, b and c are located at $(y = -1.7, z = -2.14)$ m, $(y = -0.34, z = -1.07)$ m and $(y = 1.02, z = 1)$ m, respectively.

	E [MPa]	ρ [kg/m^3]	ν	$D_p = D_s$
Top elastomer	0.3	1200	0.45	0.05
Top plate	$207 \cdot 10^3$	7850	0.30	0.01
Bot. elastomer	0.7	1200	0.35	0.05
Bottom plate	$207 \cdot 10^3$	7850	0.30	0.01

TABLE 6.3: Fasteners properties for case 2.

In order to couple this 2.5D elastodynamic FEM-BEM model with a train pass-by model, it is excited by a 2.5D vertical load applied on the top of the rails (point R on Fig. 6.5) in order to obtain the track receptances required for the train/track interaction, as explained in Sec. 4.3. A synthetic unevenness profile based on a track class 3 of the Federal Railroad Administration (FRA) classification is considered in the present calculations [81]. The train speed is assumed to be 25 m/s. The adopted rail unevenness profile

excites the train in the frequency range between 0 Hz and 250 Hz which is also the range of frequencies considered to be important for the study of ground-borne vibration and re-radiated noise induced by railway traffic. Uniformly distributed samples of 2^{12} points in the range of -10 rad/m to 10 rad/m have been used as a sampling vector of the wavenumber, as most of the spectral information of the system is contained in this range. The properties and model of the train as well as the stiffness of wheel/rail contact k_H used for this simulation can be found in Costa et al. [51].

6.3.1 Vibration analysis

Figure 6.6 shows the time histories of the vertical rail velocities for the three cases of fastener stiffness. Sub-figure (a) is the time history for the stiffest fastener in this study (case 1: Table 6.2) followed by the one which is a softer fastener (case 2: Table 6.3) in subfigure (b) and subfigure (c) represents the case which the rails are directly attached to the tunnel floor (case 3). Figure 6.7 shows the frequency content for the vertical component of the vibration velocity of rail and tunnel evaluators in one-third octave bands for the three cases of the fasteners stiffness. The octave bands are normalised with the length of the time signal, which is 13 seconds all along the present chapter. From the figures, it can be seen that the application of rail pads in the rails fastening system (cases 1 and 2) implies a reduction of the vibration in the tunnel invert as well as an increasing of the rails vibration. This behaviour cannot be clearly seen in the tunnel evaluator A, because of the specific combination of tunnel ring modes. Focusing on the cases with rail pads, it is shown that the track with softer fasteners (case 2) is a more efficient solution than the track with stiffer ones (case 1) in order to reduce the vibration in the tunnel. In general, the track in case 2 is shifting the vibration spectra in the tunnel and the rails to lower frequencies. For the case where the rail is directly fixed with the tunnel invert (case 3), the rail and tunnel behave as one solid. As a result, most of the vibration is transferred to the tunnel. Also, the vibration response of the rail and tunnel is similar for this case.

6.3.2 Noise analysis

In this section, an analysis of the noise-induced inside the tunnel due to train traffic is presented. The effect of fasteners in noise radiation fields is also discussed. A comparison is provided for the sound pressure levels in the tunnel for two cases: the noise is radiated only from the tunnel structure and the noise is radiated by the tunnel structure and the rails. A comparison of the sound pressure level obtained by the 2.5D MFS approach and
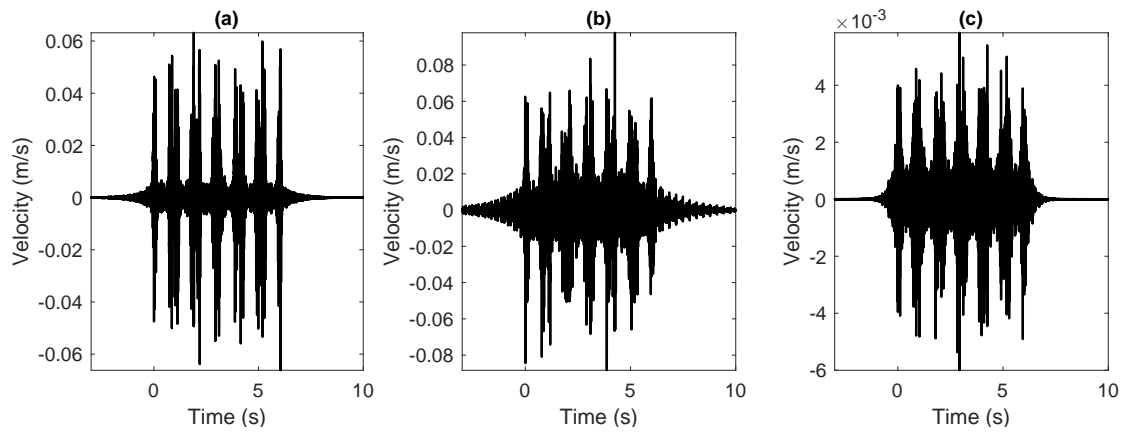
FIGURE 6.6: Time histories of the rail velocity for case 1 (a), case 2 (b) and case 3 (c).
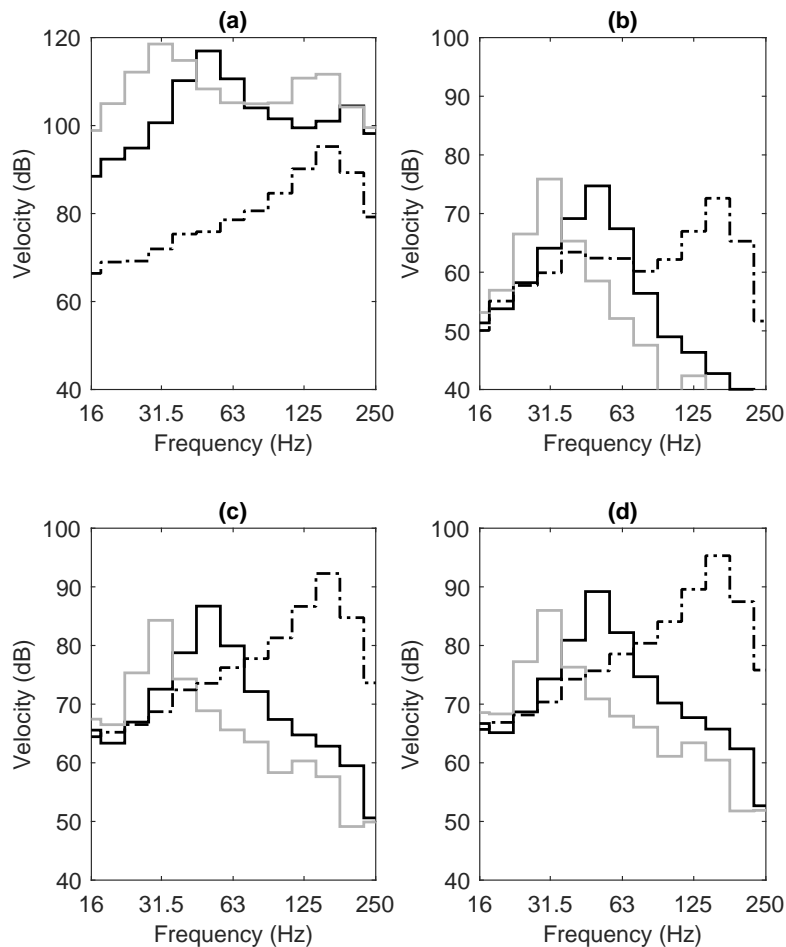
FIGURE 6.7: Vertical component of the velocity levels in dB (dB reference 10^{-8} m/s) in one-third octave bands for the rail (a), the tunnel evaluator A (b), the tunnel evaluator B (c) and the tunnel evaluator C (d). Black lines represent case 1, grey lines represent case 2 and the dash-dotted line represents case 3.

the 2.5D acoustic BEM, neglecting in both cases the contribution of the rails, is made in order to further validate the presented 2.5D acoustic BEM methodology.

Therefore, the acoustic space considered in this analysis is the interior of the tunnel. As said before, the evaluator locations in the acoustics space, where the pressure field is computed, are a, b and c in Fig. 6.5. The BEM nodes for the 2.5D acoustic BEM are denoted in purple in Fig. 6.5 and the normal velocities on all these nodes obtained from the structural response computed in previously are used as a boundary condition for this 2.5D acoustic BEM. For the case when rails are not considered, the nodes in the tunnel invert just below the rails are used as nodes in 2.5D acoustic BEM. Zero velocity is ascribed to these nodes. The collocation points required in the 2.5D MFS modelling are the same points as the nodes used by the 2.5D acoustic BEM. The boundary condition at these collocation points are the same normal velocities that are used for the 2.5D acoustic BEM. The MFS sources are placed outside the domain. The distance between source collocation points is optimised to get a proper solution from the 2.5D MFS approach. A small damping ratio of 0.025 is considered for both modelling strategies.

Noise pressure field in the wavenumber-frequency domain at all the acoustic evaluator locations for case 1 is obtained by the 2.5D acoustic BEM and the 2.5D MFS approach. The noise pressure field is computed without considering the contribution of rails. Figure 6.8 shows that both methods are showing a good agreement capturing the nature of the noise pressure field inside the tunnel.

The rail contribution to the noise levels inside the tunnel is studied by comparing noise pressure levels obtained with and without considering the rails for all the cases of rail fastening systems considered. In order to better understand the effect of fastener stiffness in the noise field, mean pressure levels of both cases are compared. These mean pressure levels are obtained by averaging the noise pressure levels over a grid of evaluators inside the acoustic space. Figure 6.9 the spectra in one-third octave bands of the mean pressure levels of noise radiation in each case obtained by neglecting rail and considering rails. From this figure, it is observed that the noise field in the tunnel radiated only because of the tunnel structure (Fig.6.9a) is affected by the fasteners stiffness in a similar way than the vibration response is affected. In contrast, the noise field is affected in a completely different way than the vibration response when the rail contribution is considered (Fig.6.9b). Thus, one can generally conclude from this results that the noise level inside the tunnel when the rail contribution is considered increases as the fasteners stiffness decreases.

Figure 6.10 shows the pressure levels obtained inside the tunnel for the acoustics evaluator a, b and c for each of the three cases of rail fastening systems. The most important
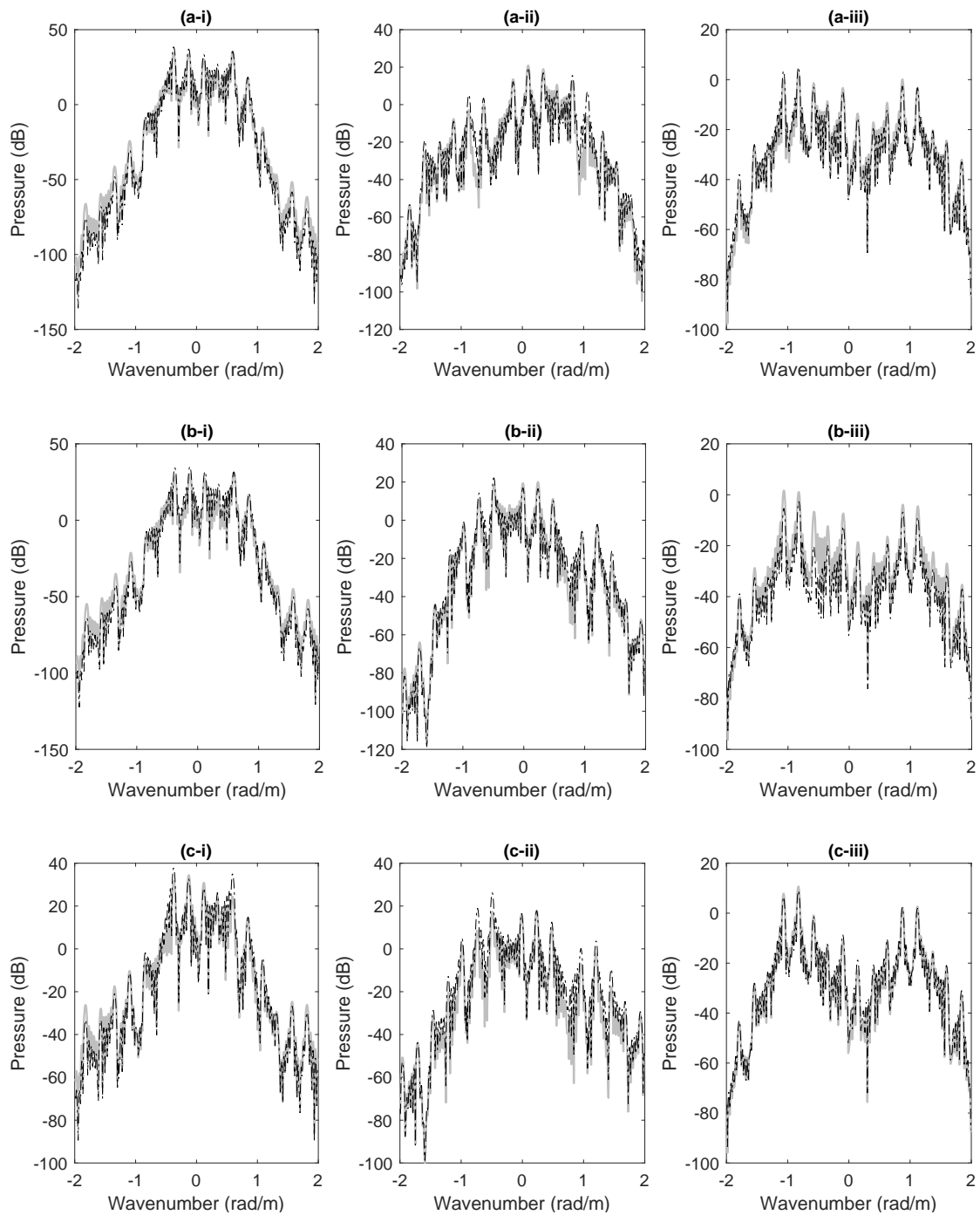
FIGURE 6.8: Noise pressure in the wavenumber-frequency domain obtained from the 2.5D MFS approach (grey line) and the 2.5D acoustic BEM (dashed black line) at acoustic evaluator a (a), acoustic evaluator b (b) and acoustic evaluator c (c), at frequencies of 44 Hz (i), 70 Hz (ii), 157 Hz (iii).
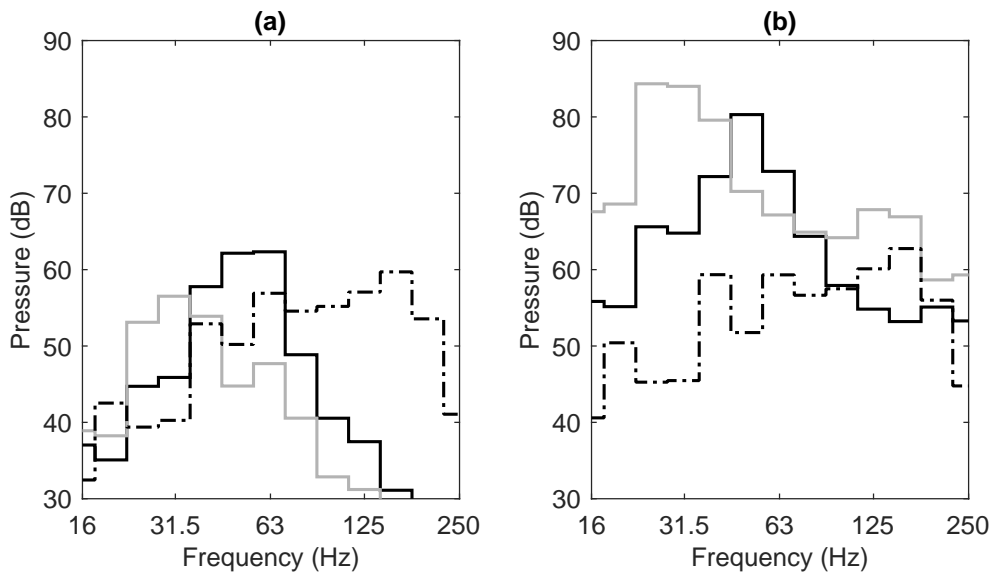
FIGURE 6.9: Mean pressure levels in dB (dB ref 20 μPa) obtained by neglecting the rail contribution (a) and considering rail contribution (b), for the case 1 (black line), 2 (grey line), and 3 (dash-dotted line) of rail fastening systems.

conclusion that one can take from this figure is that when the rail fastening system considers rail pads, the noise field inside the tunnel is completely controlled at all frequencies by the rail noise radiation, as shown at sub-figures 6.10a and 6.10b. In the case where the rail is directly attached to the tunnel, the rail contribution is similar to the one coming from the tunnel structure. From the point of view of the different rail fastening systems studied, the frequency content of the noise behaves in similar way than the vibration response previously described.
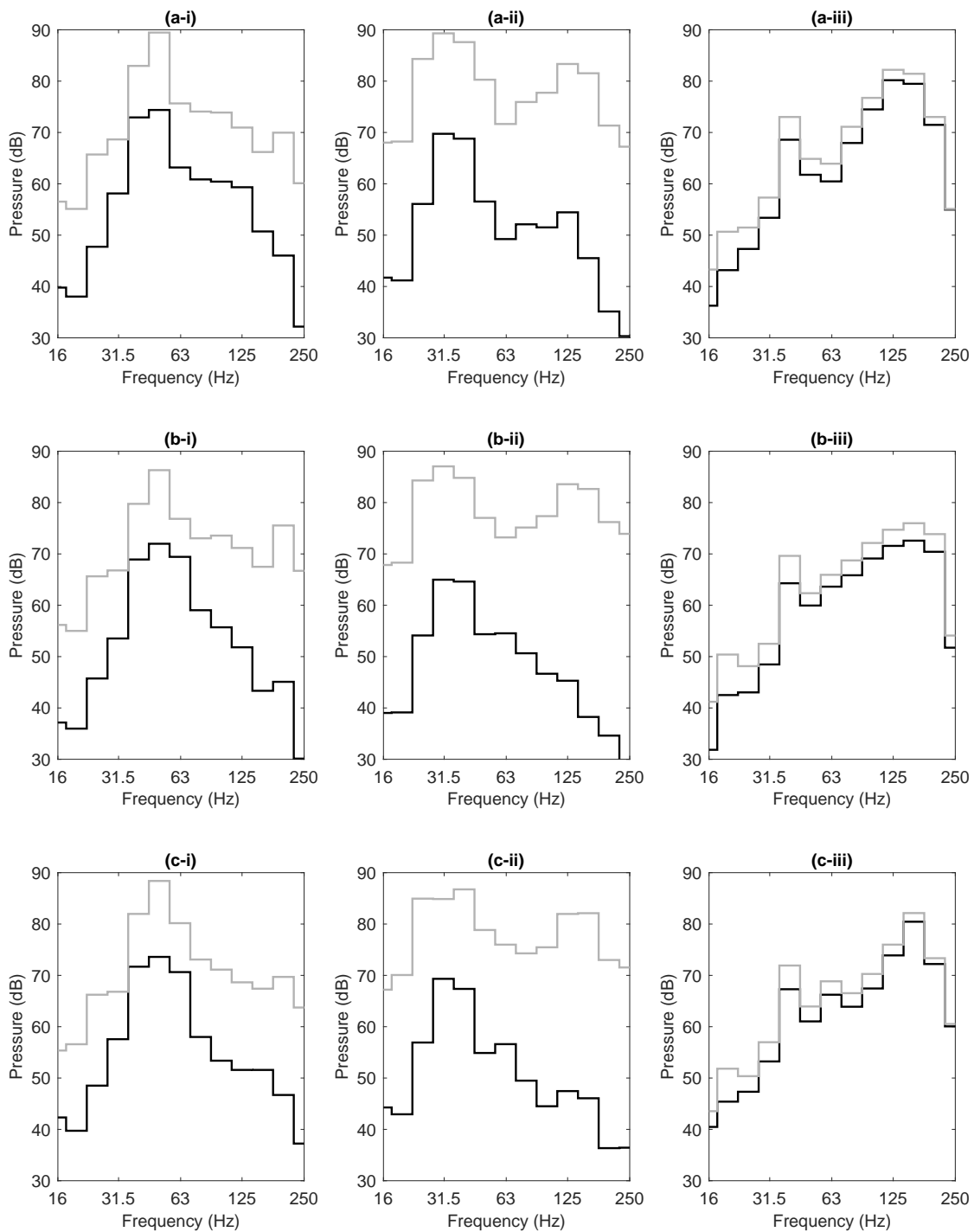
FIGURE 6.10: Pressure levels considering the rail contribution (grey line) and without the rail contribution (black line) for the acoustic evaluators a (a), b (b) and c (c) and for the cases 1 (i), 2 (ii) and 3 (iii).

Chapter 7

Conclusions and further work

7.1   Conclusions

In this thesis, a methodology for assessing railway-induced ground-borne vibration due
to underground railway infrastructures in the context of urban environments has been
presented. The methodology is based on a comprehensive numerical approach for mod-
elling track/tunnel/soil systems considering a full-space model of the ground. This
approach is formulated in the wavenumber-frequency domain (2.5D) and it is based on
coupled FEM-BEM approach combined with the semi-analytical solutions of a cavity in
a full-space and a semi-analytical model of the track. Regarding the 2.5D FEM-BEM
approach developed in this thesis, two strategies have been proposed in order to increase
the computational efficiency of the methodology. The first strategy proposes a method
for computing the Green's functions of a full-space that avoids interpolation and reduces
the number of operations of the process. The second strategy is based on an axisym-
metric formulation to deal with circular underground railway tunnels. This formulation
can also be used for other types of railway tunnels if a circular boundary of the bound-
ary element mesh is considered. A semi-analytical model of the track, coupled with
the 2.5D FEM-BEM model of the tunnel/soil system, has been established. It is based
on Euler-Bernoulli beams as a model of the rails and continuously distributed viscous
springs as a model of the fasteners is coupled to the tunnel/soil system. A methodology
which uses the semi-analytical solutions of a cavity in a full-space in conjunction with
the previously described approach has been developed with the aim of computing the
energy flow radiated upwards by underground railway tunnels. A non-uniform sampling
scheme for the wavenumber-frequency sampling to accurately capture the behaviour of
the track/tunnel/soil system on account of train pass-by has been proposed.

Since this comprehensive methodology for modelling the track/tunnel/soil system uses
finite elements to model the tunnel structure, its modelling detail is higher than the
previously developed methodologies based on semi-analytical modelling of the tunnel
structure, as the PiP method. The present methodology has been specifically designed to
be used in general assessment studies about ground-borne underground railway-induced
vibrations where decisions on the type of track and/or the application of mitigation
measures at the sources, as soft rail-pads, under-ballast or under-slab mats have to be
made. Moreover, this methodology can be used for the study of the vibration radiation
patterns of railway tunnels.

The developed methodology has been used to perform a comparison of the energy flow
radiated upwards by DFF and FST systems for two kinds of soil: a soft soil (180 MPa of
Young's modulus) and a hard soil (480 MPa of Young's modulus). From this comparison,

the following conclusions have been obtained in the context of the vibration response in the tunnel structure:

- In general, the level of vibration of the rail is larger in FST as compared to DFF for almost all frequencies below 100 Hz.

- The level of vibration on the evaluator placed in the tunnel wall for the FST system is smaller than the one associated with the DFF system.

- It is found that for the FST case, the frequency content is shifted to lower frequencies, inducing to large differences between the frequency responses of the FST and DFF systems at high frequencies, where the FST is reducing drastically the levels of vibration as compared with the DFF system.

- FST is able to reduce the level of vibrations in the tunnel wall at frequencies above 31.5Hz for both kinds of soil studied.

From the analysis of the vibration energy flow radiated by both these infrastructures, it can be concluded that:

- The total vibration energy flow radiated by FST and DFF systems is practically the same.

- The vibration energy flow radiated by infrastructures decreases with distance away from the tunnel due to the damping of the soil. The reduction observed for the DFF system is larger than the one for the FST system because the frequency content of the vibration energy in the FST is shifted to lower frequencies with respect to the DFF, in the same way, that it has been observed for the vibration in the tunnel wall.

- Taking into account that the total vibration energy flow is almost the same in both cases, one can deduce that the shift on frequency is done by the FST does not imply a change on the energy radiated.

- As expected, the vibration energy flow is affected by the soil stiffness. It is found that stiffer soil results in a reduction of the vibration energy radiated upwards and a very significant modification of the vibration energy flow radiation pattern.

The developed approach has been also used for a preliminary study on the validity of using one accelerometer for assessing the efficiency of vibration mitigation countermeasures in the framework of railway tunnels. In order to check the validity of using one

accelerometer, three evaluators placed at the tunnel wall are considered. The acceleration on the evaluators on the tunnel wall and the vibration energy spectral density were then used to compute the insertion loss between DFF and FST systems in order to get insights of the validity of using one accelerometer for assessing the effectiveness of this track systems. The main conclusions that are obtained from the vibration energy radiated upwards and the computed insertion loss are summarised as:

- It is found that the differences between the insertion loss that comes from the vibration energy flow with respect to the insertion loss coming from one accelerometer in the tunnel wall are up to 8 dB at frequencies of 63 Hz, 80 Hz and 100 Hz. Then, using one accelerometer in the tunnel wall in order to assess the efficiency of a vibration mitigation countermeasure applied in a railway tunnel overestimates its IL. On the other hand.

- The variations in the IL associated with the vibration acceleration are found to be small, implying that the location of the accelerometer is not of great importance.

- It is found that the IL of a mitigation measure could be significantly dependent on the local subsoil surrounding the tunnel infrastructure.

A modelling approach for the re-radiated noise induced by a train passage inside railway tunnels was also presented. This approach has been based on the weak coupling between the comprehensive numerical approach for modelling track/tunnel/soil previously described and a 2.5D BEM model for interior acoustics. Using this modelling approach, the influence of the fastener stiffness on the noise and vibration levels inside a simple tunnel as well as the relation between the noise emitted by the rails or the tunnel structure is investigated and discussed. The results of the application of this method in a simple tunnel case are obtained for three cases of rail fastening systems. Moreover, the results of the noise field inside the tunnel cavity are obtained with and without the contribution of the rails.

From these results, the main conclusions of the study were:

- Rail fastening system consisting of rail pads imply a reduction of the vibration levels in the tunnel structure as well as an increasing of the rails vibration.

- Softer rail pads are, in general, a more efficient solution than stiffer ones in terms of vibration reduction in the tunnel.

- The noise field inside the tunnel induced only by the tunnel structure (without the rails contribution) is affected by the stiffness of the fastener in a similar way that

the vibration response is affected. In contrast, when the rail contribution is considered, the noise level in the tunnel increases as the fasteners stiffness decreases, which is completely inverse general behaviour than the tunnel vibration level with respect to the fastener stiffness.

- If train vehicle and wheels are not considered, it is observed that the noise field inside the tunnel is completely controlled at all frequencies by the rail noise radiation.

7.2   Further work

The methodology presented in this thesis can be improved in various aspects. Improvements on the computational efficiency of the methodology are being investigated these days in LEAM-UPC. More research in order to extend the application field of the methodology is also expected to be carried out in the near future. Studies related to the efficiency of vibration mitigation countermeasures applied in the tunnel will be performed. A summary of the detailed ideas for future works is presented below.

Generalised energy flow computations

In the thesis, a methodology to compute the energy flow radiated by underground railway infrastructures has been proposed. The computation of energy flow requires the computation of tractions and displacements in the soil. Although the 2.5D FEM-BEM approach is capable of computing displacements in the soil, it cannot compute the tractions field. In this thesis, the tractions and displacements are proposed to be computed by using semi-analytical solutions of the cavity in a full-space, results that can be used for the computation of the vibration energy flow. Although this semi-analytical model is a relatively robust solution, its accuracy depends on the number of ring modes considered, which makes this solution more computationally demanding that other semi-analytical models of the ground response. Moreover, it can be used only for circular geometries in a homogeneous full-space. It is therefore proposed as a future work of the thesis to develop a faster, accurate and more general method to compute energy flow. The combination of the 2.5D FEM-BEM approach with the method of fundamental solutions or the singular boundary method is research lines in progress in the LEAM-UPC research centre.

Validity of using one accelerometer

In this thesis, a preliminary study on the validity of using one accelerometer to assess the efficiency of a FST system as a vibration mitigation countermeasure against a DFF system has been presented. Two cases of soil were considered for this preliminary study. In order to obtain a better understanding of this issue, a much more representative study that takes into account the variability of parameters such as the train speed, the stiffness of the soil, the track type, the tunnel infrastructure, the vehicle, etc... should be performed.

2.5D FEM-BEM with half-space

In this thesis, the developed 2.5D FEM-BEM can be used in the analysis of railway-induced ground-borne vibration considering full-space and half-space models of the soil. However, the thesis focused only on the general assessment studies about ground-borne underground railway-induced vibrations considering a full-space model of the ground. It is therefore proposed, as a further continuation of the 2.5D FEM-BEM developed in this thesis, to study railway-induced ground-borne vibration of the complete system consisting of train/track/tunnel/soil/building, where the soil will be modelled as a half-space. Regarding the use of the 2.5D FEM-BEM approach for the case of the half-space model of the soil it is further proposed the following:

- Use the method to obtain the half-space Green's functions given by [56] instead of using the ones of EDT toolbox [82], since the solution proposed in [56] is more computationally efficient and can be adapted easily to the sampling strategies required by the methodology presented in this thesis.

- Speed optimisation to 2.5D FEM-BEM methodology specific to the use of half-space solutions in 2.5D BEM.

- Detailed investigation on the nature of coupling load between the track and the subgrade. A preliminary study is presented on this issue in [83].

Experimental validation

The experimental validation of the present methodology for the vibration energy flow radiated by an underground railway infrastructure is a challenging task. A scale model that the LEAM-UPC have will be used in order to construct a small tunnel for the validation of this behaviour.

Hybrid methodology

In cases where the railway track is already constructed and new vibration mitigation measures are desired to be installed, it is proposed to develop a hybrid methodology model of the global system, which models the tunnel-building response using experimental measurements [84] and the other subsystems (track/track/tunnel/soil) with the methodology proposed in the thesis.

Appendix A

2.5D static Green's functions for displacements and tractions for a homogeneous full-space

The full-space elastodynamic Green's functions for tractions and displacements for nonzero frequency can be found in [25]. In this section, analytical solutions of Green's displacements and stress are given for two cases: $(\omega = 0, \ k_x \neq 0)$ and $(\omega = 0, \ k_x = 0)$. The tractions Green's functions can be found from the stress Green's functions σ, which can be obtained from strains Green's functions using the relation $\sigma_{i,j}^k = \lambda \varepsilon_{vol}^k \delta_{i,j} + 2\mu \varepsilon_{i,j}^k$, where $i, j, k = \{x, y, z\}$. In this section, $H_n^{(2)}$ are n-th order Hankel's functions of the second kind, λ is the first Lamé constant, μ is the second Lamé constant, β is the S-wave speed, α is the P-wave speed, ρ is the density of the medium, $r = \sqrt{y^2 + z^2}$ and ν is the Poisson ratio of the medium.

A.1   Expressions of the displacements Green's functions for $k_x \neq 0$ and $\omega = 0$

$$G_{xx} = \frac{H_0^{(2)}(\mathrm{i}k_x r)}{4\mathrm{i}\rho\beta^2} - \frac{k_x r H_1^{(2)}(\mathrm{i}k_x r)}{8\rho}\left(\frac{1}{\beta^2} - \frac{1}{\alpha^2}\right),$$

$$G_{yy} = \frac{H_0^{(2)}(\mathrm{i}k_x r)}{4\mathrm{i}\rho\beta^2} - \frac{1}{4\mathrm{i}\rho}\left(\frac{1}{\beta^2} - \frac{1}{\alpha^2}\right)\left[\frac{H_0^{(2)}(\mathrm{i}k_x r)}{2}\right.$$
$$\left. - \frac{\mathrm{i}k_x r \gamma_y^2}{4}\left(H_1^{(2)}(\mathrm{i}k_x r) - H_3^{(2)}(\mathrm{i}k_x r)\right) - \gamma_y^2 H_2^{(2)}(\mathrm{i}k_x r)\right],$$

$$G_{zz} = \frac{H_0^{(2)}(\mathrm{i}k_x r)}{4\mathrm{i}\rho\beta^2} - \frac{1}{4\mathrm{i}\rho}\left(\frac{1}{\beta^2} - \frac{1}{\alpha^2}\right)\left[\frac{H_0^{(2)}(\mathrm{i}k_x r)}{2}\right.$$
$$\left. - \frac{\mathrm{i}k_x r \gamma_z^2}{4}\left(H_1^{(2)}(\mathrm{i}k_x r) - H_3^{(2)}(\mathrm{i}k_x r)\right) - \gamma_z^2 H_2^{(2)}(\mathrm{i}k_x r)\right],$$

$$G_{xy} = \frac{\gamma_y k_x r}{8\rho}\left(\frac{1}{\beta^2} - \frac{1}{\alpha^2}\right)H_0^{(2)}(\mathrm{i}k_x r),$$

$$G_{xz} = \frac{\gamma_z k_x r}{8\rho}\left(\frac{1}{\beta^2} - \frac{1}{\alpha^2}\right)H_0^{(2)}(\mathrm{i}k_x r),$$

$$G_{yz} = \frac{\gamma_z \gamma_y k_x r}{8\rho}\left(\frac{1}{\beta^2} - \frac{1}{\alpha^2}\right)H_1^{(2)}(\mathrm{i}k_x r). \tag{A.1}$$

A.2   Expressions of the displacements Green's functions for $k_x = 0$ and $\omega = 0$

$$G_{xx} = \frac{1}{8\pi(1-\nu)\mu}(3-4\nu)\ln\frac{1}{r},$$

$$G_{yy} = \frac{1}{8\pi(1-\nu)\mu}\left[(3-4\nu)\ln\frac{1}{r} - \gamma_y^2\right],$$

$$G_{zz} = \frac{1}{8\pi(1-\nu)\mu}\left[(3-4\nu)\ln\frac{1}{r} - \gamma_z^2\right],$$

$$G_{xy} = 0,$$

$$G_{yz} = \frac{\gamma_y \gamma_z}{8\pi(1-\nu)\mu},$$

$$G_{xz} = 0. \tag{A.2}$$

A.3 Expressions of the strains Green's functions for $k_x \neq 0$ and $\omega = 0$

In order to get obtain the strains for the case of $k_x \neq 0$ and $\omega = 0$, the terms presented in Eq. A.3 are derived for that case. Substituting this terms in the original equations presented by [25], it is possible to find the strains for the case of $k_x \neq 0$ and $\omega = 0$.

$$
\begin{aligned}
A \cdot B_0 &= \frac{r}{16\mu(1-\nu)} \frac{H_1^{(2)}(\mathrm{i}k_x r)}{k_x}, \\
A \cdot B_1 &= \frac{-\mathrm{i}r}{16\mu(1-\nu)} H_0^{(2)}(\mathrm{i}k_x r), \\
A \cdot B_2 &= \frac{k_x r}{16\mu(1-\nu)} H_1^{(2)}(\mathrm{i}k_x r), \\
A \cdot B_3 &= \frac{\mathrm{i}k_x^2 r}{16\mu(1-\nu)} H_2^{(2)}(\mathrm{i}k_x r),
\end{aligned}
\tag{A.3}
$$

A.4 Expressions of the strains Green's functions for $k_x = 0$ and $\omega = 0$

$$\varepsilon_{\text{vol}}^x = \varepsilon_{yy}^x = \varepsilon_{zz}^x = 0,$$

$$\varepsilon_{xy}^x = -\frac{\gamma_y}{4\pi\rho\beta^2 r},$$

$$\varepsilon_{xz}^x = -\frac{\gamma_z}{4\pi\rho\beta^2 r},$$

$$\varepsilon_{yz}^x = 0,$$

$$\varepsilon_{\text{vol}}^y = -\frac{\gamma_y}{2\pi\rho\alpha^2 r},$$

$$\varepsilon_{yy}^y = \frac{\gamma_y}{4\pi\rho r}\left(\frac{1 - 2\gamma_y^2}{\beta^2} - \frac{3 - 2\gamma_y^2}{\alpha^2}\right),$$

$$\varepsilon_{zz}^y = \frac{\gamma_y}{4\pi\rho r}(1 - 2\gamma_z^2)\left(\frac{1}{\beta^2} - \frac{1}{\alpha^2}\right),$$

$$\varepsilon_{xy}^y = \varepsilon_{yy}^x = 0,$$

$$\varepsilon_{yz}^y = -\frac{\gamma_z}{4\pi\rho r}\left(\frac{2\gamma_y^2}{\beta^2} + \frac{1 - 2\gamma_y^2}{\alpha^2}\right),$$

$$\varepsilon_{\text{vol}}^z = \varepsilon_{\text{vol}}^y,$$

$$\varepsilon_{yy}^z = \frac{\gamma_z}{4\pi\rho r}(1 - 2\gamma_y^2)\left(\frac{1}{\beta^2} - \frac{1}{\alpha^2}\right),$$

$$\varepsilon_{zz}^z = \frac{\gamma_z}{4\pi\rho r}\left(\frac{1 - 2\gamma_z^2}{\beta^2} - \frac{3 - 2\gamma_z^2}{\alpha^2}\right),$$

$$\varepsilon_{xy}^z = \varepsilon_{xz}^z = 0,$$

$$\varepsilon_{yz}^z = -\frac{\gamma_y}{4\pi\rho r}\left(\frac{2\gamma_z^2}{\beta^2} + \frac{1 - 2\gamma_z^2}{\alpha^2}\right). \tag{A.4}$$

Appendix B

Boundary Integral Equation

B.1 Boundary integral equation for acoustics

The boundary integral equation for acoustics in 2.5D is derived similarly following the procedure followed by François et. al. for deriving the integral equation for elastodynamics. The boundary integral representation equation for acoustic is in 2.5D is derived from the 3D boundary integral representation equation for acoustics

$$P(x_0, y_0, z_0) = -\int_{\Gamma} [P(x, y, z)\frac{\partial G(r)}{\partial n} + \mathrm{i}\rho\omega G(r)V_n(x, y, z)]\mathrm{d}\Gamma, \qquad \text{(B.1)}$$

where $P(x_0, y_0, z_0)$ denotes sound pressure in acoustic domain, $V_n(x_0, y_0, z_0)$ denotes air particle velocity amplitude in normal direction of boundary domain, (x_0, y_0, z_0) is the location of source point and (x, y, z) is the location of the receiver point. $G(r) = \frac{e^{\mathrm{i}k_0 r}}{4\pi r}$ is the Green's function for sound pressure in 3D. $\frac{\partial G(r)}{\partial n} = \bar{H}(r)$ is the normal derivative of Green's function for pressure. $r = \sqrt{(x - x_0)^2 + (y - y_0)^2 + (z - z_0)^2}$, $k_0 = \frac{\omega}{c_0}$ and c_0 the speed of sound in air.

For 2.5D it is assumed that the domain is invariant in x-direction, thus the normal vector n is independent of x coordinate. So the integral equation on a cross-section denoted by Γ of the boundary can be written as

$$P(x_0, y_0, z_0) = -\int_{-\infty}^{-\infty} \left[\int_{\Gamma} P(x, y, z)\frac{\partial G(r)}{\partial n} + \mathrm{i}\rho\omega G(r)V_n(x, y, z)\mathrm{d}\Gamma\right]\mathrm{d}x. \qquad \text{(B.2)}$$

It is also assumed that the sound field is spatially harmonic in the x-direction with wavenumber k_x

$$P(x, y, z) = P(k_x, y, z)e^{-ik_x x}, \qquad V_n(x, y, z) = V_n(k_x, y, z)e^{-ik_x x}, \qquad \text{(B.3)}$$

Equation (B.2) is then written as

$$
\begin{aligned}
P(k_x, y_0, z_0) &= -\int_{-\infty}^{-\infty} \left[\iint_{\Gamma} P(k_x, y, z)e^{-ik_x x}\frac{\partial G(r)}{\partial n} + i\rho\omega G(r)V_n(k_x, y, z)e^{-ik_x x}\mathrm{d}\Gamma \right]\mathrm{d}x \\
&= -e^{-ik_x x}\int_{\Gamma}\left[\int_{-\infty}^{-\infty} P(k_x, y, z)\frac{\partial G(r)}{\partial n}e^{-ik_x(x-x_0)}\mathrm{d}(x - x_0) \right. \\
&\qquad \left. + i\rho\omega G(r)e^{-ik_x(x-x_0)}\int_{-\infty}^{-\infty} V_n(k_x, y, z)\mathrm{d}(x - x_0) \right]\mathrm{d}\Gamma,
\end{aligned}
$$
$$\text{(B.4)}$$

after rearranging and operating Eq. (B.4) becomes

$$\bar{\boldsymbol{P}}(\mathbf{x}) = -\int_{\Gamma}\left[\bar{\boldsymbol{P}}(\mathbf{y})\bar{\boldsymbol{H}}(\mathbf{r}) + i\rho\omega\bar{\boldsymbol{V}}_n(\mathbf{y})\bar{\boldsymbol{G}}(\mathbf{r}) \right]\mathrm{d}\Gamma, \qquad \text{(B.5)}$$

where $\mathbf{x} = (y_0, z_0)$ is the vector of source location and $\mathbf{y} = (y, z)$ is the vector of receiver location in this case the boundary. Thus the equation relates the pressure and normal velocity on the boundary to the pressure in the domain. This equation is not valid on the boundary. In order to obtain the equation valid on the boundary, the source point is moved on the boundary and a limiting process is followed which results in the regularisation of the integral equation. Details of this procedure are established in the Marc Bonnet. Here the final form of the boundary integral equation for the bounded and unbounded domain is given.

The regularised boundary integral equation for bounded domains is

$$\int_{\Gamma}\left[\bar{\boldsymbol{P}}(\mathbf{y})\bar{\boldsymbol{H}}(\mathbf{x}, \mathbf{y}) - \bar{\boldsymbol{P}}(\mathbf{x})\bar{\boldsymbol{H}}_0(\mathbf{x}, \mathbf{y}) \right]\mathrm{d}\Gamma = i\rho\omega\int_{\Gamma}\bar{\boldsymbol{V}}_n(\mathbf{y})\bar{\boldsymbol{G}}(\mathbf{x}, \mathbf{y})\mathrm{d}\Gamma, \qquad \text{(B.6)}$$

and for unbounded domains

$$\bar{\boldsymbol{P}}(\mathbf{x}) = \int_{\Gamma}\left[\bar{\boldsymbol{P}}(\mathbf{y})\bar{\boldsymbol{H}}(\mathbf{x}, \mathbf{y}) - \bar{\boldsymbol{P}}(\mathbf{x})\bar{\boldsymbol{H}}_0(\mathbf{x}, \mathbf{y}) \right]\mathrm{d}\Gamma - i\rho\omega\int_{\Gamma}\bar{\boldsymbol{V}}_n(\mathbf{y})\bar{\boldsymbol{G}}(\mathbf{x}, \mathbf{y})\mathrm{d}\Gamma, \qquad \text{(B.7)}$$

B.2 2.5D Green's functions for the 2.5D acoustic BEM approach

The Green's function for the pressure is given by

$$G(k_x, r) = \frac{1}{2\pi} K_0(k_a r), \tag{B.8}$$

while velocity Green's function is given by

$$H(k_x, r) = -\frac{k_a}{2\pi} K_1(k_a r) \left(\frac{y - y_0}{r} n_y + \frac{z - z_0}{r} n_z \right), \tag{B.9}$$

where, $k_a = \sqrt{k_x^2 - k_0^2}$, $k_0 = \omega/c_0$ and $r = \sqrt{(y - y_0)^2 + (z - z_0)^2}$, (y, z) is the location of the receiver point and (y_0, z_0) is the location of source point, K_0 and K_1 are modified Bessel functions of the second kind of order zero and one, respectively, n_y and n_z are the $y-$, $z-$ component of unit normal, respectively, and c_0 is the speed of sound.

B.3 Analytical solutions related to the acoustic field radiated by a 2.5D pulsating cylinder and inside a rectangular tube

The analytical solution for pressure field generated by a 2.5D pulsating cylinder [66] is given by

$$\bar{P}(r) = \frac{i\rho\omega v_n K_0(k_a r)}{k_a K_1(k_a r)}, \tag{B.10}$$

where v_n is the velocity amplitude in radial direction.

The analytical solution for pressure field inside the rectangular tube [85] is given by

$$P(x) = \rho c_0 \omega u_n \left(\sin \frac{\omega x}{c_0} + \frac{\cos \frac{\omega x}{c_0}}{\tan \frac{\omega L_x}{c_0}} \right), \tag{B.11}$$

where u_n is the displacement amplitude normal to the surface, x is the horizontal coordinate of the evaluation points which are located on the center line of the tube and L_x is the width of the tube.

Appendix C

Finite element method

The differential equation of the elastic domain is given by

$$\nabla \cdot \boldsymbol{\sigma} + \mathbf{b} = \rho \frac{\mathrm{d}^2 \mathbf{u}}{\mathrm{d}t^2},$$ (C.1)

where $\boldsymbol{\sigma}$ is the stress tensor that acts on the infinitesimal volume, $\mathbf{b}$ is the matrix of forces, ρ is the density of the elastic volume and u is the vector of displacement. The weak form of the problem is derived by applying to the previous expression a field of virtual displacements v and integrating on a generic volume Ω with boundary Γ.

$$\int_\Omega \mathbf{v}^T \nabla \cdot \boldsymbol{\sigma} \, \mathrm{d}\Omega - \int_\Omega \mathbf{v}^T \rho \frac{\mathrm{d}^2 \mathbf{u}}{\mathrm{d}t^2} \, \mathrm{d}\Omega + \int_\Omega \mathbf{v}^T \rho \mathbf{b} \, \mathrm{d}\Omega = 0,$$ (C.2)

The application of the divergence theorem to the first integral on the left side of Eq. (C.2) allows establish

$$\int_\Omega \mathbf{v}^T \nabla \cdot \boldsymbol{\sigma} \, \mathrm{d}\Omega = \int_\Gamma \left(\mathbf{v}^T \boldsymbol{\sigma} \right) \mathbf{n} \, \mathrm{d}\Gamma - \int_\Omega (\nabla \mathbf{v})^T : \boldsymbol{\sigma} \, \mathrm{d}\Omega.$$ (C.3)

where n is the outward normal to boundary Γ. This allows to write Eq. (C.2) as:

$$\int_\Omega (\nabla \mathbf{v})^T : \boldsymbol{\sigma} \, \mathrm{d}\Omega + \int_\Omega \mathbf{v}^T \rho \frac{\mathrm{d}^2 \mathbf{u}}{\mathrm{d}t^2} \, \mathrm{d}\Omega = \int_\Omega \mathbf{v}^T \rho \mathbf{b} \, \mathrm{d}\Omega + \int_\Gamma \mathbf{v}^T \mathbf{g} \, \mathrm{d}\Gamma,$$ (C.4)

where $\mathbf{g}$ is defined as the vector of tensions, applied at the volume boundary, in the direction of normal vector.

The equilibrium condition imposed implies that the stress tensor $\boldsymbol{\sigma}$ is symmetric and thus,

$$\left(\nabla \mathbf{v}^T \right) : \boldsymbol{\sigma} = (\nabla \mathbf{v}) : \boldsymbol{\sigma} = \frac{1}{2} \left(\nabla \mathbf{v}^T + \nabla \mathbf{v} \right) : \boldsymbol{\sigma}.$$ (C.5)

The displacements are related to strain ε by

$$\varepsilon(\mathbf{u}) = \frac{1}{2} \left(\nabla \mathbf{u}^T + \nabla \mathbf{u} \right). \tag{C.6}$$

The stress tensor is related to the strain tensor as:

$$\boldsymbol{\sigma} = \mathbf{C}\varepsilon, \tag{C.7}$$

where the tensor $\mathbf{C}$, which relates the tensors $\boldsymbol{\sigma}$ and ε under linear a linear transformation. The response of the system is assumed to be harmonic with frequency ω in time and so the displacements can be written as:

$$\mathbf{u}(\mathbf{x}, t) = \mathbf{u}(\mathbf{x})e^{\mathrm{i}\omega t}, \tag{C.8}$$

where $\mathbf{x}$ is the cordinate system, which leads to transformation of Eq. (C.4) as

$$\int_\Omega \boldsymbol{\varepsilon}(\mathbf{v}) : \sigma(\mathbf{u}) \, \mathrm{d}\Omega - \omega^2 \int_\Omega \mathbf{v}^T \rho \mathbf{u} \, \mathrm{d}\Omega = \int_\Omega \mathbf{v}^T \rho \mathbf{b} \, \mathrm{d}\Omega + \int_\Gamma \mathbf{v}^T \mathbf{g} \, \mathrm{d}\Gamma. \tag{C.9}$$

An alternative vector notation for the symmetrical stress tensor is used where the components are collected in the vector $\boldsymbol{\sigma}$ and analogously, the vector $\boldsymbol{\varepsilon}$ collects the components of the symmetrical strain tensor where, $\boldsymbol{\sigma} = (\sigma_{xx}, \sigma_{yy}, \sigma_{zz}, \sigma_{xy}, \sigma_{yx}, \sigma_{zx})^T$ and $\boldsymbol{\varepsilon} = (\varepsilon_{xx}, \varepsilon_{yy}, \varepsilon_{zz}, \gamma_{xy}, \gamma_{yz}, \gamma_{zx},)^T$ and $\gamma_{ij} = 2\varepsilon_{ij}$, $i \neq j$. As the domain is assumed to be invariant in the x direction, the displacements are then a function of cordinates y and z. Introducing the finite element discretisation, the displacement can be written as:

$$\mathbf{u}(\mathbf{x}, \omega) = \mathbf{N}(y, z)\tilde{\mathbf{u}}(x, \omega) \tag{C.10}$$

where, $\tilde{\mathbf{u}}(x, \omega)$ is the nodal displacement which is a function of ω and the cordinate x. $\mathbf{N}$ is the matrix of the finite element shape functions. The strain vector can then be derived from the discretised displacements as

$$\varepsilon = \mathbf{D}\mathbf{u} = \mathbf{D}\mathbf{N}\tilde{\mathbf{u}} = \mathbf{D}_1\mathbf{N}\tilde{\mathbf{u}} + \mathbf{D}_2\mathbf{N}\frac{\partial \tilde{\mathbf{u}}}{\partial x} \tag{C.11}$$

where $\mathbf{D}_1$ and $\mathbf{D}_2$ are given as:

$$
\mathbf{D}_1 = \begin{bmatrix} \frac{\partial}{\partial x} & 0 & 0 \\ 0 & 0 & 0 \\ 0 & 0 & \frac{\partial}{\partial z} \\ 0 & \frac{\partial}{\partial x} & 0 \\ 0 & \frac{\partial}{\partial z} & 0 \\ \frac{\partial}{\partial z} & 0 & \frac{\partial}{\partial x} \end{bmatrix}, \quad
\mathbf{D}_2 = \begin{bmatrix} 0 & 0 & 0 \\ 0 & 1 & 0 \\ 0 & 0 & 0 \\ 1 & 0 & 0 \\ 0 & 0 & 1 \\ 0 & 0 & 0 \end{bmatrix}, \tag{C.12}
$$

for simplicity, $\mathbf{L}_1 = \mathbf{D}_1 \mathbf{N}$ and $\mathbf{L}_2 = \mathbf{D}_2 \mathbf{N}$. Inserting the finite element discretisation and using the constitutive relationship mentioned in Eq. (C.7), allows to write Eq. (C.9) as:

$$
\int_\Omega \left(\mathbf{L}_1 \tilde{\mathbf{v}} + \mathbf{L}_2 \frac{\partial \tilde{\mathbf{v}}}{\partial x} \right)^T \mathbf{C} \left(\mathbf{L}_1 \tilde{\mathbf{u}} + \mathbf{L}_2 \frac{\partial \tilde{\mathbf{u}}}{\partial x} \right) \, \mathrm{d}\Omega
$$
$$
-\omega^2 \int_\Omega (\mathbf{N}\tilde{\mathbf{v}})^T \rho (\mathbf{N}\tilde{\mathbf{u}}) \, \mathrm{d}\Omega = \int_\Omega (\mathbf{N}\tilde{\mathbf{v}})^T \rho \mathbf{b} \, \mathrm{d}\Omega + \int_\Gamma (\mathbf{N}\tilde{\mathbf{v}})^T \mathbf{g} \, \mathrm{d}\Gamma. \tag{C.13}
$$

Simplifying the equation by rewriting the volume integrals as an integral over the longitudinal coordinate x and the cross section A

$$
\int_{-\infty}^{+\infty} \frac{\partial \tilde{\mathbf{v}}^T}{\partial x} \mathbf{K}_{21} \tilde{\mathbf{u}} \, \mathrm{d}x + \int_{-\infty}^{+\infty} \frac{\partial \tilde{\mathbf{v}}^T}{\partial x} \mathbf{K}_2 \frac{\partial \tilde{\mathbf{u}}}{\partial x} \, \mathrm{d}x + \int_{-\infty}^{+\infty} \tilde{\mathbf{v}}^T \mathbf{K}_0 \tilde{\mathbf{u}} \, \mathrm{d}x
$$
$$
+ \int_{-\infty}^{+\infty} \tilde{\mathbf{v}}^T \mathbf{K}_{12} \frac{\partial \tilde{\mathbf{u}}}{\partial x} \, \mathrm{d}x - \omega^2 \int_{-\infty}^{+\infty} \tilde{\mathbf{v}}^T \mathbf{M} \tilde{\mathbf{u}} \, \mathrm{d}x = \tag{C.14}
$$
$$
= \int_{-\infty}^{+\infty} \tilde{\mathbf{v}}^T \left(\int_A \mathbf{N}^T \rho \mathbf{b} \, \mathrm{d}A \right) \, \mathrm{d}x + \int_{-\infty}^{+\infty} \tilde{\mathbf{v}}^T \left(\int_l \mathbf{N}^T \mathbf{g} \, \mathrm{d}l \right) \, \mathrm{d}x,
$$

where

$$
\mathbf{K}_0 = \int_A \mathbf{L}_1^T \mathbf{C} \mathbf{L}_1 \, \mathrm{d}A, \quad \mathbf{K}_{12} = \int_A \mathbf{L}_1^T \mathbf{C} \mathbf{L}_2 \, \mathrm{d}A,
$$
$$
\mathbf{K}_{21} = \int_A \mathbf{L}_2^T \mathbf{C} \mathbf{L}_1 \, \mathrm{d}A, \quad \mathbf{K}_2 = \int_A \mathbf{L}_2^T \mathbf{C} \mathbf{L}_2 \, \mathrm{d}A, \tag{C.15}
$$
$$
\mathbf{M} = \int_A \mathbf{N}^T \rho \mathbf{N} \, \mathrm{d}A.
$$

From integration of parts in the above equation one can find that

$$
\int_{-\infty}^{+\infty} \frac{\partial \tilde{\mathbf{v}}^T}{\partial x} \mathbf{K}_{21} \tilde{\mathbf{u}} \, \mathrm{d}x = \mathbf{v}^T \mathbf{K}_{21} \mathbf{u} \Big|_{-\infty}^{\infty} - \int_{-\infty}^{+\infty} \tilde{\mathbf{v}}^T \mathbf{K}_{21} \frac{\partial \tilde{\mathbf{u}}}{\partial x} \, \mathrm{d}x,
$$
$$
\int_{-\infty}^{+\infty} \frac{\partial \tilde{\mathbf{v}}^T}{\partial x} \mathbf{K}_2 \frac{\partial \tilde{\mathbf{u}}}{\partial x} \, \mathrm{d}x = \mathbf{v}^T \mathbf{K}_2 \frac{\partial \tilde{\mathbf{u}}}{\partial x} \Big|_{-\infty}^{\infty} - \int_{-\infty}^{+\infty} \tilde{\mathbf{v}}^T \mathbf{K}_2 \frac{\partial^2 \tilde{\mathbf{u}}}{\partial x^2} \, \mathrm{d}x. \tag{C.16}
$$

Equation C.14 can then be simplified as

$$-\int_{-\infty}^{+\infty} \tilde{\mathbf{v}}^T \mathbf{K}_2 \frac{\partial^2 \tilde{\mathbf{u}}}{\partial x^2} \, \mathrm{d}x + \int_{-\infty}^{+\infty} \tilde{\mathbf{v}}^T \mathbf{K}_0 \tilde{\mathbf{u}} \, \mathrm{d}x$$
$$+ \int_{-\infty}^{+\infty} \tilde{\mathbf{v}}^T \mathbf{K}_1 \frac{\partial \tilde{\mathbf{u}}}{\partial x} \, \mathrm{d}x - \omega^2 \int_{-\infty}^{+\infty} \tilde{\mathbf{v}}^T \mathbf{M} \tilde{\mathbf{u}} \, \mathrm{d}x = \quad \text{(C.17)}$$
$$= \int_{-\infty}^{+\infty} \tilde{\mathbf{v}}^T \left(\int_A \mathbf{N}^T \rho \mathbf{b} \, \mathrm{d}A \right) \mathrm{d}x + \int_{-\infty}^{+\infty} \tilde{\mathbf{v}}^T \left(\int_l \mathbf{N}^T \mathbf{g} \, \mathrm{d}l \right) \mathrm{d}x,$$

where $\mathbf{K}_1 = \mathbf{K}_{12} - \mathbf{K}_{21}$. Since the initial formulation has been proposed for any virtual displacement field all integrals over the longitudinal coordinate x vanish and the equation is equivalent to

$$\mathbf{K}_0 \tilde{\mathbf{u}}(y,\omega) + \mathbf{K}_1 \frac{\partial \tilde{\mathbf{u}}(y,\omega)}{\partial x} - \mathbf{K}_2 \frac{\partial^2 \tilde{\mathbf{u}}(y,\omega)}{\partial x^2} - \omega^2 \mathbf{M} \tilde{\mathbf{u}}(y,\omega) = \boldsymbol{f}(y,\omega), \quad \text{(C.18)}$$

and the external load vector is

$$\boldsymbol{f}(y,\omega) = \int_l \mathbf{N}^T \mathbf{g} \, \mathrm{d}l + \int_A \mathbf{N}^T \rho \mathbf{b} \, \mathrm{d}A. \quad \text{(C.19)}$$

The Fourier transform property that allows to convert differential equations to linear one is given as

$$\mathcal{F} \left[\frac{\partial h(y)}{\partial x}, k_y \right] = -\mathrm{i}k_x h(x). \quad \text{(C.20)}$$

Taking into account the above property of the Fourier transform Eq. (C.18) is rewritten as,

$$\left(\mathbf{K}_0 - \omega^2 \mathbf{M} - ik_x \mathbf{K}_1 + k_x^2 \mathbf{K}_2 \right) \boldsymbol{U} = \boldsymbol{F}, \quad \text{(C.21)}$$

which represent the 2.5D finite element equation and where $\mathbf{K}_0$, $\mathbf{K}_1$, $\mathbf{K}_2$ are the stiffness matrices and $\mathbf{M}$ is the mass matrix of the finite element domain which are independent of wavenumber k_y and the frequency ω.

Appendix D

Vehicle Model

Fig. D.1 shows a visual description of the vehicle model, which is a system of 10 DOF. These are the car body vertical displacement z_c, the car body pitch, the vertical displacements of both bogies, the pitch of both bogies and the vertical displacements of the four wheels, which are all represented by the variables z_c, φ_c, $z_{\text{bog}}^{(1)}$, $z_{\text{bog}}^{(2)}$, $\varphi_{\text{bog}}^{(1)}$, $\varphi_{\text{bog}}^{(2)}$, $z_w^{(1)}$, $z_w^{(2)}$, $z_w^{(3)}$ and $z_w^{(4)}$, respectively. Regarding to the other variables illustrated in Fig. D.1, m_c is the car body mass, J_c is the car body mass inertia, $m_{\text{bog}}^{s(i)}$ is the sprung mass of the ith bogie, $k_{ss}^{(i)}$ is the stiffness of the ith bogie secondary suspension, $\eta_{ss}^{(i)}$ is the structural damping coefficient of the ith bogie secondary suspension, $c_{ss}^{(i)}$ is the viscous damping of the ith bogie secondary suspension, $m_{\text{bog}}^{(i)}$ is the unsprung mass of the ith bogie, $J_{\text{bog}}^{(i)}$ is the unsprung mass inertia of the ith bogie, $k_{ps}^{(j)}$ is the stiffness of the jth wheelset primary suspension, $\eta_{ps}^{(j)}$ is the structural damping coefficient of the jth wheelset primary suspension, $c_{ps}^{(j)}$ is the viscous damping of the jth wheelset primary suspension, $m_{ps}^{(j)}$ is the mass of the jth wheelset primary suspension, $m_w^{(j)}$ is the mass of the jth wheelset, d_{sc} is the distance between bogies of the same car, d_{dc} is the distance between bogies of the different cars and d_w is the distance between wheelsets of the same bogie.
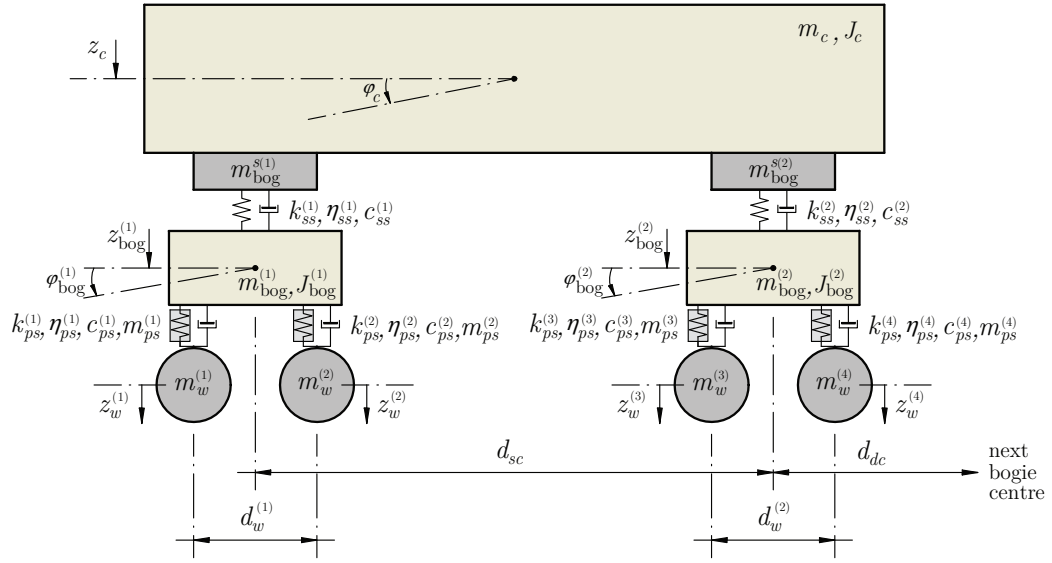
FIGURE D.1: Vehicle model.

Considering a vector of DOF organized as

$$\left\{ z_c \quad \varphi_c \quad z_{\text{bog}}^{(1)} \quad \varphi_{\text{bog}}^{(1)} \quad z_{\text{bog}}^{(2)} \quad \varphi_{\text{bog}}^{(2)} \quad z_w^{(1)} \quad z_w^{(2)} \quad z_w^{(3)} \quad z_w^{(4)} \right\}^{\text{T}}, \tag{D.1}$$

the nonzero terms of the upper triangular part of the stiffness matrix of this vehicle model are

$$K_{1,1} = k_{ss}^{*(1)} + k_{ss}^{*(2)} + \mathrm{i}\omega\left(c_{ss}^{(1)} + c_{ss}^{(2)}\right) - \omega^2\left(m_c + m_{\mathrm{bog}}^{s(1)} + m_{\mathrm{bog}}^{s(2)}\right),$$

$$K_{1,2} = \left[k_{ss}^{*(1)} - k_{ss}^{*(2)} + \mathrm{i}\omega\left(c_{ss}^{(1)} - c_{ss}^{(2)}\right)\right]\frac{d_{sc}}{2},$$

$$K_{2,2} = \left[k_{ss}^{*(1)} + k_{ss}^{*(2)} + \mathrm{i}\omega\left(c_{ss}^{(1)} + c_{ss}^{(2)}\right)\right]\frac{d_{sc}^2}{4} - \omega^2 J_{c+\mathrm{bog}}^s,$$

$$K_{1,1+2i} = -\left(k_{ss}^{*(i)} + \mathrm{i}\omega c_{ss}^{(i)}\right),$$

$$K_{2,3} = -\left(k_{ss}^{*(1)} + \mathrm{i}\omega c_{ss}^{(1)}\right)\frac{d_{sc}}{2},$$

$$K_{2,5} = \left(k_{ss}^{*(2)} + \mathrm{i}\omega c_{ss}^{(2)}\right)\frac{d_{sc}}{2},$$

$$K_{1+2i,1+2i} = k_{ss}^{*(i)} + k_{ps}^{**(2i-1)}\mathfrak{c}_{2i-1} + k_{ps}^{**(2i)}\mathfrak{c}_{2i} + \mathrm{i}\omega c_{ss}^{(i)} - \omega^2 m_{\mathrm{bog}}^{(i)},$$

$$K_{1+2i,2+2i} = \left[k_{ps}^{**(2i-1)}\mathfrak{c}_{2i-1} - k_{ps}^{**(2i)}\mathfrak{c}_{2i}\right]\frac{d_w^{(i)}}{2},$$

$$K_{2+2i,2+2i} = \left[k_{ps}^{**(2i-1)}\mathfrak{s}_{2i-1} + k_{ps}^{**(2i)}\mathfrak{s}_{2i}\right]\frac{d_w^{2(i)}}{4} - \omega^2 J_{\mathrm{bog}}^{(i)},$$

$$K_{1+2i,6+j} = -k_{ps}^{**(j)}\mathfrak{c}_j,$$

$$K_{2+2i,5+2i} = -\left(k_{ps}^{**(2i-1)}\mathfrak{c}_{2i-1}\right)\frac{d_w^{(i)}}{2},$$

$$K_{2+2i,6+2i} = \left(k_{ps}^{**(2i-1)}\mathfrak{c}_{2i-1}\right)\frac{d_w^{(i)}}{2},$$

$$K_{6+j,6+j} = k_{ps}^{**(j)}\mathfrak{c}_j - \omega^2 m_w^{(j)} \tag{D.2}$$

where $J_{c+\mathrm{bog}}^s = J_c + (d_{sc}^2/4)(m_{\mathrm{bog}}^{s(1)} + m_{\mathrm{bog}}^{s(2)})$ and where $i = 1, 2$ and $j = 1, 2, 3, 4$, taking into account that the expressions containing both i and j are restricted to the following conditions: $j = 1, 2$ when $i = 1$ and $j = 3, 4$ when $i = 2$. The single asterisk notation denotes a complex stiffness defined with the general expression $k^* = k(1 + \mathrm{i}\,\mathrm{sign}(\omega)\eta)$ and the double asterisk also denotes a complex stiffness with the general expression $k^* = k(1 + \mathrm{i}\,\mathrm{sign}(\omega)\eta) + \mathrm{i}\omega c)$. Finally, the $\mathfrak{s}_j$ and $\mathfrak{c}_j$ associated to the j-th primary suspension are defined as

$$\mathfrak{s}_j = \frac{1}{\mathrm{sinc}\left(\pi\dfrac{\omega}{\omega_0^{(j)}}\right)}, \quad \mathfrak{c}_j = \frac{\cos\left(\pi\dfrac{\omega}{\omega_0^{(j)}}\right)}{\mathrm{sinc}\left(\pi\dfrac{\omega}{\omega_0^{(j)}}\right)}, \tag{D.3}$$

where

$$\omega_0^{(j)} = \sqrt{\frac{k_{ps}^{(j)**}}{m_{ps}^{(j)}}}. \tag{D.4}$$

A summary of the parameters of this vehicle model, the values taken in the present paper and the units of each parameter are shown in Table D.1. As shown, the massive parameters are divided by two since the values required of the half-vehicle. The stiffness of the secondary and primary suspension are already given for of vehicle system.

Vehicle parameters	Notation	Units	Value
Car body mass	m_c	[kg]	41923/2
Car body mass inertia	J_c	[kg m^{-2}]	$(9.17/2) \cdot 10^5$
Sprung mass of the ith bogie	$m_{\text{bog}}^{s(i)}$	[kg]	720/2
Stiffness of the ith bogie's secondary suspension	$k_{ss}^{(i)}$	[N m^{-1}]	$8.14 \cdot 10^5$
Structural damping coefficient of the ith bogie's secondary suspension	$\eta_{ss}^{(i)}$	[$-$]	0
Viscous damping of the ith bogie's secondary suspension	$c_{ss}^{(i)}$	[N s m^{-1}]	$15 \cdot 10^3$
Unsprung mass of the ith bogie	$m_{\text{bog}}^{(i)}$	[kg]	1730/2
Unsprung mass inertia of the ith bogie	$J_{\text{bog}}^{(i)}$	[kg m^{-2}]	824/2
Stiffness of the jth wheelset's primary suspension	$k_{ps}^{(j)}$	[N m^{-1}]	$1.24 \cdot 10^6$
Structural damping coefficient of the jth wheelset's primary suspension	$\eta_{ps}^{(j)}$	[$-$]	0
Viscous damping of the jth wheelset's primary suspension	$c_{ps}^{(j)}$	[N s m^{-1}]	$\cdot 10^4$
Mass of the jth wheelset's primary suspension	$m_{ps}^{(j)}$	[kg]	0
Mass of the jth wheelset	$m_w^{(j)}$	[kg]	1410/2
Distance between bogies of the same car	d_{sc}	[m]	11.368
Distance between bogies of different cars	d_{dc}	[m]	4.97
Distance between wheelsets of the ith bogie	$d_w^{(i)}$	[m]	2

TABLE D.1: Vehicle model parameters and data.

Bibliography

[1] International Organization for Standardization. ISO 2631-1. Mechanical vibration and shock. Evaluation of human exposure to whole-body vibration. Part 1: General requirements, 1997.

[2] Buhm Park, Jin-Yong Jeon, Sunghoon Choi, and Junhong Park. Short-term noise annoyance assessment in passenger compartments of high-speed trains under sudden variation. *Applied Acoustics*, 97:46 – 53, 2015.

[3] Christian H. Kasess, Anton Noll, Piotr Majdak, and Holger Waubke. Effect of train type on annoyance and acoustic features of the rolling noise. *The Journal of the Acoustical Society of America*, 134(2):1071–1081, 2013.

[4] Jin Yong Jeon, Joo Young Hong, Hyung Suk Jang, and Jae Hyeon Kim. Speech privacy and annoyance considerations in the acoustic environment of passenger cars of high-speed trains. *The Journal of the Acoustical Society of America*, 138(6):3976–3984, 2015.

[5] International Organization for Standardization. ISO 14837-1. Mechanical vibration. Ground-borne noise and vibration arising from rail systems. Part 1: General Guidance, 2005.

[6] D.P. Connolly, G. Kouroussis, O. Laghrouche, C.L. Ho, and M.C. Forde. Benchmarking railway vibrations – Track, vehicle, ground and building effects. *Construction and Building Materials*, aug 2014.

[7] D. P. Connolly, P. Alves Costa, G. Kouroussis, P. Galvin, P. K. Woodward, and O. Laghrouche. Large scale international testing of railway ground vibrations across Europe. *Soil Dynamics and Earthquake Engineering*, 71:1–12, 2015.

[8] Y. B. Yang and L. C. Hsu. A review of researches on ground-borne vibrations due to moving trains via underground tunnels. *Advances in Structural Engineering*, 9(3):377–392, jun 2006.

[9] G. Lombaert and G. Degrande. Ground-borne vibration due to static and dynamic axle loads of InterCity and high-speed trains. *Journal of Sound and Vibration*, 319(3-5):1036–1066, jan 2009.

[10] S. Gupta and G. Degrande. Modelling of continuous and discontinuous floating slab tracks in a tunnel using a periodic approach. *Journal of Sound and Vibration*, 329(8):1101–1125, apr 2010.

[11] X. Sheng, C. J. C. Jones, and D. J. Thompson. A comparison of a theoretical model for quasi-statically and dynamically induced environmental vibration from trains with measurements. *Journal of Sound and Vibration*, 267(3):621–635, oct 2003.

[12] H. E. M. Hunt. Prediction of vibration transmission from railways into buildings using models of infinite length. *Vehicle System Dynamics*, 24(S):234–247, 1995.

[13] H. E. M. Hunt. Modelling of rail vehicles and track for calculation of ground-vibration transmission into buildings. *Journal of Sound and Vibration*, 193(1):185–194, 1996.

[14] H. E. M. Hunt. Stochastic modelling of traffic-induced ground vibration. *Journal of Sound and Vibration*, 144(1):53–70, 1991.

[15] Lan Ding, Hong Ping Zhu, Hui Luo, and Tao Yin. Flexural wave propagation and localization in periodic jointed tunnels subjected to moving loads. *JVC/Journal of Vibration and Control*, 22(11):2788–2804, 2016.

[16] C. He, S. Zhou, P. Guo, H. Di, and X. Zhang. Analytical model for vibration prediction of two parallel tunnels in a full-space. *Journal of Sound and Vibration*, 423:306–321, 2018.

[17] Z. Yuan, A. Boström, and Y. Cai. Benchmark solution for vibrations from a moving point source in a tunnel embedded in a half-space. *Journal of Sound and Vibration*, 387:177–193, 2017.

[18] C. He, S. Zhou, H. Di, P. Guo, and J. Xiao. Analytical method for calculation of ground vibration from a tunnel embedded in a multi-layered half-space. *Computers and Geotechnics*, 99(February):149–164, 2018.

[19] J. A. Forrest and H. E. M. Hunt. A three-dimensional tunnel model for calculation of train-induced ground vibration. *Journal of Sound and Vibration*, 294(4-5):678–705, jul 2006.

[20] J. A. Forrest and H. E. M. Hunt. Ground vibration generated by trains in underground tunnels. *Journal of Sound and Vibration*, 294(4-5):706–736, jul 2006.

[21] M. F. M. Hussein and H. E. M. Hunt. A numerical model for calculating vibration from a railway tunnel embedded in a full-space. *Journal of Sound and Vibration*, 305(3):401–431, aug 2007.

[22] S. Gupta, M. F. M. Hussein, G. Degrande, H. E. M. Hunt, and D. Clouteau. A comparison of two numerical models for the prediction of vibrations from underground railway traffic. *Soil Dynamics and Earthquake Engineering*, 27(7):608–624, jul 2007.

[23] M. F. M. Hussein, S. Gupta, H. E. M. Hunt, G. Degrande, and J. P. Talbot. An efficient model for calculating vibration from a railway tunnel buried in a half-space. In *Proceedings of the Thriteenth International Congress on Sound and Vibration, Vienna*, 2006.

[24] E. Kausel and J. M. Roësset. Stiffness matrices for layered soils. *Bulletin of the Seismological Society of America*, 71(6):1743–1761, 1981.

[25] A. J. B. Tadeu and E. Kausel. Green's functions for two-and-a-half-dimensional elastodynamic problems. *Journal of Engineering Mechanics - ASCE*, 126(10):1093–1097, 2000.

[26] M.F.M. Hussein, S. François, M. Schevenels, H.E.M. Hunt, J.P. Talbot, and G. Degrande. The fictitious force method for efficient calculation of vibration from a tunnel embedded in a multi-layered half-space. *Journal of Sound and Vibration*, 333(25):6996–7018, dec 2014.

[27] T. Balendra, K. H. Chua, K. W. Lo, and S. L. Lee. Steady-state vibration of subway-soil-building system. *Journal of Engineering Mechanics*, 115(1):145–162, jan 1989.

[28] K. H. Chua, T. Balendra, and K. W. Lo. Groundborne vibrations due to trains in tunnels. *Earthquake Engineering & Structural Dynamics*, 21(5):445–460, 1992.

[29] T. Balendra, C. G. Koh, and Y. C. Ho. Dynamic response of buildings due to trains in underground tunnels. *Earthquake Engineering & Structural Dynamics*, 20(3):275–291, 1991.

[30] X. Sheng, C. J. C. Jones, and D. J. Thompson. Prediction of ground vibration from trains using the wavenumber finite and boundary element methods. *Journal of Sound and Vibration*, 293(3-5):575–586, jun 2006.

[31] A. A. Stamos and D. E. Beskos. Dynamic analysis of large 3-D underground structures by the bem. *Earthquake Engineering & Structural Dynamics*, 24(6):917–934, 1995.

[32] L. Godinho, P. Amado-Mendes, and A. Tadeu. Meshless analysis of soil-structure interaction using an MFS-MLPG coupled approach. *Engineering Analysis with Boundary Elements*, 55:80–92, 2015.

[33] Luís Godinho, Julieta António, and António Tadeu. Sound propagation around rigid barriers laterally confined by tall buildings. *Applied Acoustics*, 63(6):595–609, 2002.

[34] António Tadeu, Julieta António, Luís Godinho, and Paulo A. Mendes. Simulation of sound absorption in 2D thin elements using a coupled BEM/TBEM formulation in the presence of 3D sources. *International Journal for Housing Science and Its Applications*, 36(4):189–198, may 2012.

[35] J.D.R. Bordón, J.J. Aznárez, and O. Maeso. A 2D BEM–FEM approach for time harmonic fluid–structure interaction analysis of thin elastic bodies. *Eng. Anal. Bound. Elem.*, 43:19–29, June 2014.

[36] L. A. Padrón, J. J. Aznárez, and O. Maeso. BEM-FEM coupling model for the dynamic analysis of piles and pile groups. *Engineering Analysis with Boundary Elements*, 31(6):473–484, jun 2007.

[37] L. Andersen and C.J.C. Jones. Coupled boundary and finite element analysis of vibration from railway tunnels—a comparison of two- and three-dimensional models. *Journal of Sound and Vibration*, 293(3-5):611–625, jun 2006.

[38] Gordon C. Everstine and Francis M. Henderson. Coupled finite element/boundary element approach for fluid-structure interaction. *The Journal of the Acoustical Society of America*, 87(5):1938–1947, 1990.

[39] Z. C. He, G. R. Liu, Z. H. Zhong, G. Y. Zhang, and A. G. Cheng. A coupled ES-FEM/BEM method for fluid-structure interaction problems. *Engineering Analysis with Boundary Elements*, 35(1):140–147, 2011.

[40] Z. C. He, G. Y. Li, Z. H. Zhong, A. G. Cheng, G. Y. Zhang, Eric Li, and G. R. Liu. An ES-FEM for accurate analysis of 3D mid-frequency acoustics using tetrahedron mesh. *Computers and Structures*, 106-107:125–134, 2012.

[41] P. Fiala, G. Degrande, and F. Augusztinovicz. Numerical modelling of ground-borne noise and vibration in buildings due to surface rail traffic. *Journal of Sound and Vibration*, 301(3-5):718–738, apr 2007.

[42] D. Clouteau, M. Arnst, T. M. Al-Hussaini, and G. Degrande. Freefield vibrations due to dynamic loading on a tunnel embedded in a stratified medium. *Journal of Sound and Vibration*, 283(1-2):173–199, may 2005.

[43] D. Clouteau, M. L. Elhabre, and D. Aubry. Periodic BEM and FEM-BEM coupling - Application to seismic behaviour of very long structures. *Computational Mechanics*, 25(6):567–577, jun 2000.

[44] S. Gupta, W. F. Liu, G. Degrande, G. Lombaert, and W. N. Liu. Prediction of vibrations induced by underground railway traffic in Beijing. *Journal of Sound and Vibration*, 310(3):608–630, feb 2008.

[45] A. Yaseri, M. H. Bazyar, and S. Javady. 2.5D coupled FEM-SBFEM analysis of ground vibrations induced by train movement. *Soil Dynamics and Earthquake Engineering*, 104(October 2017):307–318, 2018.

[46] Patrícia Lopes, P. Alves Costa, M. Ferraz, R. Calçada, and A. Silva Cardoso. Numerical modeling of vibrations induced by railway traffic in tunnels: From the source to the nearby buildings. *Soil Dynamics and Earthquake Engineering*, 61-62:269–285, jun 2014.

[47] P. Fiala, S. Gupta, G. Degrande, and F. Augusztinovicz. A numerical model for re-radiated noise in buildings. In *Noise and Vibration Mitigation for Rail Transportation Systems. In: Proceedings of 9th International Workshop on Railway Noise, Munich, Germany, 2007*, volume 99, pages 115–121, 2008.

[48] X. Sheng, C. J. C. Jones, and D. J. Thompson. A theoretical model for ground vibration from trains generated by vertical track irregularities. *Journal of Sound and Vibration*, 272(3-5):937–965, may 2004.

[49] P. Alves Costa, R. Calçada, and A. Silva Cardoso. Influence of train dynamic modelling strategy on the prediction of track-ground vibrations induced by railway traffic. *Proceedings of the Institution of Mechanical Engineers, Part F: Journal of Rail and Rapid Transit*, 226(4):434–450, jan 2012.

[50] S. François, M. Schevenels, P. Galvín, G. Lombaert, and G. Degrande. A 2.5D coupled FE-BE methodology for the dynamic interaction between longitudinally invariant structures and a layered halfspace. *Computer Methods in Applied Mechanics and Engineering*, 199(23-24):1536–1548, apr 2010.

[51] P. Alves Costa, R. Calçada, and A. Silva Cardoso. Track-ground vibrations induced by railway traffic: In-situ measurements and validation of a 2.5D FEM-BEM model. *Soil Dynamics and Earthquake Engineering*, 32(1):111–128, jan 2012.

[52] XueCheng Bian, YunMin Chen, and Ting Hu. Numerical simulation of high-speed train induced ground vibrations using 2.5D finite element approach. *Science in China, Series G: Physics, Mechanics and Astronomy*, 51(6):632–650, 2008.

[53] X. Sheng, C. J. C. Jones, and D. J. Thompson. Modelling ground vibration from railways using wavenumber finite- and boundary-element methods. *Proceedings of the Royal Society A: Mathematical, Physical and Engineering Sciences*, 461(2059):2043–2070, jul 2005.

[54] Qiyun Jin, David J. Thompson, Daniel E. J. Lurcock, Martin G. R. Toward, and Evangelos Ntotsios. A 2.5D finite element and boundary element model for the ground vibration from trains in tunnels and validation using measurement data. *Journal of Sound and Vibration*, 422(February):373–389, 2018.

[55] P. Galvín, S. François, M. Schevenels, E. Bongini, G. Degrande, and G. Lombaert. A 2.5D coupled FE-BE model for the prediction of railway induced vibrations. *Soil Dynamics and Earthquake Engineering*, 30(12):1500–1512, dec 2010.

[56] Behshad Noori, Robert Arcos, Arnau Clot, and Jordi Romeu. A method based on 3D stiffness matrices in Cartesian coordinates for computation of 2.5D elastodynamic Green's functions of layered half-spaces. *Soil Dynamics and Earthquake Engineering*, 114(July):154–158, 2018.

[57] Patrícia Lopes, Pedro Alves Costa, M. Ferraz, R. Calçada, and A. Silva Cardoso. Numerical modeling of vibrations induced by railway traffic in tunnels: From the source to the nearby buildings. *Soil Dynamics and Earthquake Engineering*, 61-62:269 – 285, 2014.

[58] Paulo Amado-Mendes, Pedro Alves Costa, Luís M.C. Godinho, and Patrícia Lopes. 2.5D MFS-FEM model for the prediction of vibrations due to underground railway traffic. *Engineering Structures*, 104:141–154, 2015.

[59] L. Godinho, P. Amado-Mendes, J. Carbajo, and J. Ramis-Soriano. 3D numerical modelling of acoustic horns using the method of fundamental solutions. *Engineering Analysis with Boundary Elements*, 51:64–73, 2015.

[60] A. Tadeu, J. António, and L. Godinho. Defining an accurate MFS solution for 2.5D acoustic and elastic wave propagation. *Engineering Analysis with Boundary Elements*, 33(12):1383–1395, 2009.

[61] D. Brookes, W. I. Hamad, H. E. M. Hunt, M. F. M. Hussein, and J. P. Talbot. The dynamic interaction effects of railway tunnels: Crossrail and the Grand Central Recording Studios. *Proceedings of the Institution of Mechanical Engineers, Part F: Journal of Rail and Rapid Transit*, 232(2):542–559, 2017.

[62] M. Germonpré, J. C.O. Nielsen, G. Degrande, and G. Lombaert. Contributions of longitudinal track unevenness and track stiffness variation to railway induced vibration. *Journal of Sound and Vibration*, 437:292–307, 2018.

[63] A. Romero, A. Tadeu, P. Galvín, and J. António. 2.5D coupled BEM-FEM used to model fluid and solid scattering wave. *International Journal for Numerical Methods in Engineering*, 101(2):148–164, 2014.

[64] A. Romero, P. Galvín, J. António, J. Domínguez, and A. Tadeu. Modelling of acoustic and elastic wave propagation from underground structures using a 2.5D BEM-FEM approach. *Engineering Analysis with Boundary Elements*, 76(July 2016):26–39, 2017.

[65] Aires Colaço, Pedro Alves Costa, Paulo Amado-Mendes, and Luís Godinho. Prediction of Vibrations and Reradiated Noise Due to Railway Traffic: A Comprehensive Hybrid Model Based on a Finite Element Method and Method of Fundamental Solutions Approach. *Journal of Vibration and Acoustics*, 139(6):061009, 2017.

[66] X. Sheng, T. Zhong, and Y. Li. Vibration and sound radiation of slab high-speed railway tracks subject to a moving harmonic load. *Journal of Sound and Vibration*, 395:160 – 186, 2017.

[67] G Lombaert, G Degrande, S François, and D J Thompson. Ground-Borne Vibration due to Railway Traffic: A Review of Excitation Mechanisms, Prediction Methods and Mitigation Measures. In *Noise and Vibration Mitigation for Rail Transportation Systems SE - 33*, volume 126, pages 253–287. Springer Berlin Heidelberg, 2015.

[68] A. Dijckmans, P. Coulier, J. Jiang, M. G.R. Toward, D. J. Thompson, G. Degrande, and G. Lombaert. Mitigation of railway induced ground vibration by heavy masses next to the track. *Soil Dynamics and Earthquake Engineering*, 75:158–170, 2015.

[69] A. Dijckmans, A. Ekblad, A. Smekal, G. Degrande, and G. Lombaert. Efficacy of a sheet pile wall as a wave barrier for railway induced ground vibration. *Soil Dynamics and Earthquake Engineering*, 84:55–69, 2016.

[70] P. Alves Costa, R. Calçada, and A. Silva Cardoso. Ballast mats for the reduction of railway traffic vibrations. Numerical study. *Soil Dynamics and Earthquake Engineering*, 42:137–150, 2012.

[71] D. J. Thompson, J. Jiang, M. G.R. Toward, M. F.M. Hussein, A. Dijckmans, P. Coulier, G. Degrande, and G. Lombaert. Mitigation of railway-induced vibration by using subgrade stiffening. *Soil Dynamics and Earthquake Engineering*, 79:89–103, 2015.

[72] M. F. M. Hussein. *Vibration from underground railways*. PhD thesis, University of Cambridge, 2004.

[73] A. Castanheira-Pinto, P. Alves-Costa, L. Godinho, and P. Amado-Mendes. On the application of continuous buried periodic inclusions on the filtering of traffic vibrations: A numerical study. *Soil Dynamics and Earthquake Engineering*, 113(June):391–405, 2018.

[74] R. Arcos, J. Romeu, A. Balastegui, and T. Pàmies. Determination of the near field distance for point and line sources acting on the surface of an homogeneous and viscoelastic half-space. *Soil Dynamics and Earthquake Engineering*, 31(7):1072–1074, jul 2011.

[75] D. C. Gazis. Three-dimensional investigation of the propagation of waves in hollow circular cylinders. I. Analytical foundation. *The Journal of the Acoustical Society of America*, 31(5):568–573, 1959.

[76] M. F. M. Hussein and H. E. M. Hunt. Modelling of floating-slab tracks with continuous slabs under oscillating moving loads. *Journal of Sound and Vibration*, 297(1-2):37–54, oct 2006.

[77] A. Clot, J. Romeu, R. Arcos, and S. R. Martín. A power flow analysis of a double-deck circular tunnel embedded in a full-space. *Soil Dynamics and Earthquake Engineering*, 57:1–9, feb 2014.

[78] A. Clot, J. Romeu, and R. Arcos. An energy flow study of a double-deck tunnel under quasi-static and harmonic excitations. *Soil Dynamics and Earthquake Engineering*, 89:1–4, 2016.

[79] M. Bonnet. *Boundary integral equation methods for solids and fluids*. Wiley, 1999.

[80] Aires Colaço, Pedro Alves Costa, Paulo Amado-Mendes, Filipe Magalhães, and Luís Godinho. Experimental validation of a FEM-MFS hybrid numerical approach for vibro-acoustic prediction. *Applied Acoustics*, 141(January):79–92, 2018.

[81] C. E. Hanson, P. E. Jason, C. Ross, and D. A. Towers. High-speed ground transportation noise and vibration impact assessment. Technical report, U.S. Department of Transportation. Federal Railroad Administration Office, Washington, 2012.

[82] M. Schevenels, S. François, and G. Degrande. EDT: An ElastoDynamics Toolbox for MATLAB. *Computers and Geosciences*, 35(8):1752–1754, 2009.

[83] D. Ghangale, J. Romeu, R. Arcos, B. Noori, A. Clot, and J. Cayero. Study of the validity of a rectangular strip track/soil coupling in railway semi-analytical

prediction models. In *Numerical Methods in Geotechnical Engineering IX*, volume 1, pages 407–414, 2018.

[84] R. Arcos, D. Ghangale, A. Clot, B. Noori, and J. Romeu. Hybrid model for rail fasteners stiffness optimization in railway-induced ground-borne vibration problems. In *Proceedings of the 6th conference on Noise and Vibration Emerging Methods (NOVEM)*, pages 1–11, 2018.

[85] W. Desmet and D. Vandepitte. Finite Element Modeling for Acoustics. In *ISAAC13-International Seminar on Applied Acoustics, Leuven*, pages 37–85, 2005.